UNIVERSITY OF CALIFORNIA
Los Angeles

X-ray synchrotron radiation in a plasma wiggler

A dissertation submitted in partial satisfaction
of the requirements for the degree
Doctor of Philosophy in Electrical Engineering

by

Shuoqin Wang

2002

The dissertation of Shuoqin Wang is approved.

Eli Yablonovitch

Claudio Pellegrini

Warren B. Mori

Chandrashekhar Joshi, Committee Chair

University of California, Los Angeles

2002

To Esther Xuege Wang...

TABLE OF CONTENTS

LIST OF FIGURES

LIST OF TABLES

ACKNOWLEDGMENTS

First, I wish to express my great appreciation for my advisor professor Chan Joshi. His guidance, encouragement and research leadership is crucial for my research accomplishment. I also thank him for having me join one of the most advanced experiments in beam-plasma physics and work with many great scientists in prestigious national labs (SLAC, LBNL) . I am very grateful for this unique experience. Thanks to him, he often teaches me — do my best, and do not worry the rest. I hope that I can fully grasp this virtue in my later scientific career.

I owe many other people gratitude as I got training in experiment, theory and computer simulations over my graduate years at UCLA.

On the experimental side, first I thank Chris Clayton for his versatility and his great patience in training me. He helped me in every experiment I have done. I would never have finished my thesis without his shoulder. Ken Marsh was indispensable especially in my beginning years as a graduate student researcher at UCLA. He taught me a lot of basic but very practical skills in the lab. It is a very fun experience to work with him. I am very grateful to have a chance work with Professor Robert Siemann of Stanford University. I admire him for his amazed experience in every aspect of experimental field. I appreciate his guidance, his generous hospitality, and especially for putting up with a graduate student in his group. I wish to thank Patrick Muggli of USC, since many solutions to my experiment problems originated from his stimulated comments. Our long conversations (especially during the long carpool hours on highways connecting San Jose and LA) let me understand that as a plasma physicist, not only should physics be rich, but also life. I thank Mark Hogan and Dieter Walz for their constant support as I worked at SLAC. They are great scientists as well as great race-runners. I thank my colleague and roommate Brent Blue for his help as we worked at SLAC. We endured long-hours of experiments in the FFTB tunnel, and also enjoyed many restaurants around SLAC in our spare time, not to mention frisbee play outside the E-157 trailer in the midnights.

On the theoretical side, I am grateful for the guidance of Professor Warren Mori of the plasma simulations group. I enjoy very much of the chemistry of this group. I appreciate training not only in computer simualations but also in swimming skills. Another key figure is Professor Tom Katsouleas of USC. I have benefited from his clear physical pictures and his outstanding ability in making back-of-the envelope estimates. I thank Chuang Ren for his valuable suggestions to my simulation problems. I also thank Frank Tsung for teaching me from scratch about running codes. Viktor Decyk can always be relied upon whenever I was stuck with compiling Fortran 90 codes. I thank my colleagues Chengkun Huang and Lu Wei for their constant help with their computer skills.

To Professor John M. Dawson I owe my gratitude for his serious thinking of my naive physics questions. Unfortunately for my generation, we are too late to benefit from his deep insight in science.

There are many others who have helped me over the years, and I thank them for their helpful advice. Among them are Dan Gordon and Dave Blackwell, former graduate students, Even Dodd, Recardo Fonseca and Luis Silva of the simulations group and Seung Lee of USC. Especially thanks to Pantaneo Raimondi and Rick Iverson of SLAC for helping me understanding the SLAC beam transportation.

I appreciate Maria Guerrero for her administrative help during these years.

In relation to the specifics of this thesis, I appreciate Hal Tompkins of SSRL for his support with the X-ray diagnostics. E. Esarey and D. Whittum of LBNL provided me valuable comments on my experimental work. I am indebted to Sergei Tochitsky for his patience in editing part of my thesis and fixing my English problems.

My family gives me huge support which is fundamental to any of my work.

Vita

1967	Born, Anqin, Anhui Province, P.R.China.
1989	B.S. (Electronic Engineering), Zhejiang University, Hangzhou, Zhejiang, P.R. China.
1992	M.S.E.E. (Electronic Engineering), Zhejiang University, P.R. China.
1997	M.S. (Physics), The University of Alabama, Tuscaloosa, Alabama, USA.
1997–	Graduate Student Researcher, Department of Electrical Engineering, University of California, Los Angeles, California, USA.

Publications

Shuoqin Wang, C.E. Clayton, B.E. Blue, E. S. Dodd, K. A. Marsh, W. B. Mori, C. Joshi, S. Lee, P. Muggli, T. Katsouleas, R. Assmann, F. J. Decker, M. J. Hogan, R. H. Iverson, P. Riamondi, D. Walz, R. Siemann, "X-ray emission from betatron motion in a plasma wiggler", Phys. Rev. Lett., 88, 135004 (2002).

E. S. Dodd, R. G. Hemker, C.-K. Huang, S. Wang, C. Ren, W. B. Mori, S. Lee, and T. Katsouleas, "Hosing and sloshing of short-pulse GeV-class wakefield drivers", Phys. Rev. Lett., 88, 125001 (2002).

C. E. Clayton, B. E. Blue, E. S. Dodd, C. Joshi, K. A. Marsh, W. B. Mori, S. Wang, P. Catravas, S. Chattopadhyay, E. Esarey, W. P. Leemans, R. Assmann, F. J. Decker, M. J. Hogan, R. Iverson, P. Raimondi, R. H. Siemann, D. Walz, T. Katsouleas, S. Lee, and P. Muggli., "Transverse envelope dynamics of a 28.5-GeV electron beam in a long plasma", Phys. Rev. Lett., 88, 154801 (2002).

S. Lee, T. Katsouleas, P. Muggli, W. B. Mori, C. Joshi, R. Hemker, E. S. Dodd, C. E. Clayton, K. A. Marsh, B. Blue, S. Wang, R. Assmann, F. J. Decker, M. Hogan, R. Iverson, and D. Walz, "Energy doubler for a linear collider", Phys. Rev. ST Accel. Beams, 5, 011001 (2002)

Patric Muggli, Seung Lee, Thomas Katsouleas, Ralph Assmann, Franz-Joseph Decker, Mark J. Hogan, Richard Iverson, Pantaleo Raimondi, Robert H. Siemann, Dieter Walz, Brent Blue, Christopher E. Clayton, Evan Dodd, Ricardo A. Fonseca, Roy Hemker, Chandrashekhar Joshi, Kenneth A. Marsh, Warren B. Mori, and Shuoqin Wang , "Boundary effects: Refraction of a particle beam", Nature, 411, 6833, (2001).

P. Catravas, S. Chattopadhyay, E. Esarey, W. P. Leemans, R. Assmann, F.-J. Decker, M. J. Hogan, R. Iverson, R. H. Siemann, D. Walz, D. Whittum, B. Blue, C. Clayton, C. Joshi, K. A. Marsh, W. B. Mori, S. Wang , T. Katsouleas, S. Lee, and P. Muggli, "Measurements of radiation near an atomic spectral line from the interaction of a 30 GeV electron beam and a long plasma", Phys. Rev. E, 64, 046502 (2001).

M. J. Hogan, R. Assmann, F.-J. Decker, R. Iverson, P. Raimondi, S. Rokni, R.

H. Siemann, D. Walz, D. Whittum, B. Blue, C. E. Clayton, E. Dodd, R. Hemker, C. Joshi, K. A. Marsh, W. B. Mori, S. Wang, T. Katsouleas, S. Lee, and P. Muggli , P. Catravas, S. Chattopadhyay, E. Esarey, and W. P. Leemans, "E-157: A 1.4-m-long plasma wake field acceleration experiment using a 30 GeV electron beam from the Stanford Linear Accelerator Center Linac", Physics of Plasmas ,7, 2241-2248, (2000).

P. Muggli, K. A. Marsh, S. Wang, C. E. Clayton, S. Lee, T. Katsouleas, and C. Joshi, "Photo-ionized lithium source for plasma accelerator applications", IEEE, Transaction on Plasma Science, 27, 791-799, (1999).

ABSTRACT OF THE DISSERTATION

X-ray synchrotron radiation in a plasma wiggler

by

Shuoqin Wang

Doctor of Philosophy in Electrical Engineering
University of California, Los Angeles, 2002
Professor Chandrashekhar Joshi, Chair

A relativistic electron beam can radiate due to its betatron motion inside an ion channel. The ion channel is induced by the electron bunch as it propagates through an underdense plasma. In the theory section of this thesis the formation of the ion channel, the trajectories of beam electrons inside the ion channel, the radiation power and the radiation spectrum of the spontaneous emission are studied. The comparison between different plasma wiggler schemes is made. The difficulties in realizing stimulated emission as the beam traverses the ion channel are investigated, with particular emphasis on the bunching mechanism, which is important for the ion channel free electron laser. This thesis reports an experiment conducted at the Stanford Linear Accelerator Center (SLAC) to measure the betatron X-ray radiations for the first time. We first describe the construction and characterization of the lithium plasma source. In the experiment, the transverse oscillations of the SLAC 28.5 GeV electron beam traversing through a 1.4 meter long lithium plasma source are clearly seen. These oscillations lead to a quadratic density dependence of the spontaneously emitted betatron X-ray radiation. The divergence angle of the X-ray radiation is measured. The absolute photon yield and the spectral brightness at 14.2 KeV photon energy are

estimated and seen to be in reasonable agreement with theory.

CHAPTER 1

Introduction

A key feature of a plasma is its ability to support various kinds of waves or collective modes of oscillation. These plasma waves correspond to charge density fluctuations along with their associated electric fields. Although collective phenomena in plasmas are known to be common in space or in man-made plasma reactors, only recently it has been possible to produce and manipulate such waves in a controllable manner in the laboratory, thanks to the developments of powerful laser and particle beam drivers and reproducible plasma sources. These collective fields induced in a plasma by such drivers can be incredibly strong. Although these fields are not desirable in some applications such as laser fusion, whereas electrons accelerated by the fields can prematurely heat the fuel in a fusion capsule and make efficient implosions difficult, they are desirable in other applications. Some of the applications of collective fields, induced by a short but intense particle beam, are shown in Fig. 1.1. These are

(a) Plasma Wake Field Accelerator [1]. According to theory, the longitudinal wake field of a plasma wave that has a phase velocity of speed of light c, is on the order of $\sqrt{n_p\ (cm^{-3})}\ V/cm$, where n_p is the plasma density. Electric fields as large as 100 GV/m have been shown in experiments [2], which is three orders of magnitude larger than the typical breakdown voltage of a conventional rf electron accelerator operating at 3 GHz.

(b) Plasma lens [3]. A relativistic electron beam (REB) can get focused as it

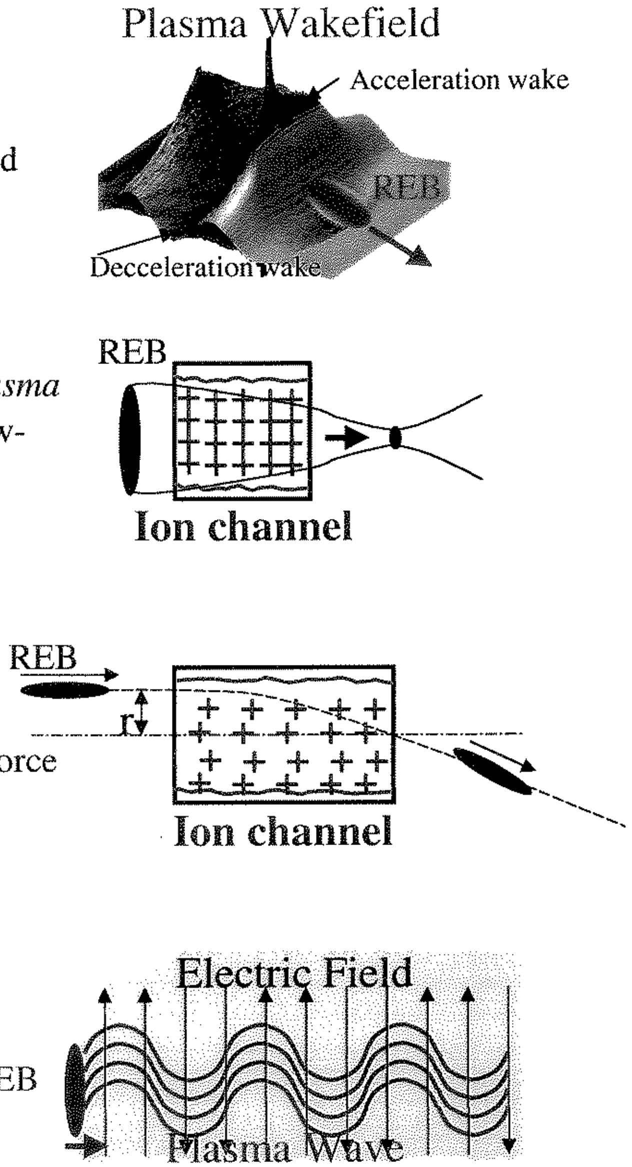

(a) *Beam Acceleration* in a Plasma Wake Field Acceleration (PWFA) scheme

(b) *Beam focusing/Plasma Lens* in a plasma "blow-out" regime

(c) *Beam Steering* with asymmetric ion force

(d) *Beam Wiggling* with a plasma wave

Figure 1.1: Schematics of four different relativistic beam handling techniques using a plasma.

traverses a plasma under certain conditions. Especially if the beam density is larger than the plasma density and the transverse size of the beam is smaller than the plasma skin depth (so called blow-out condition), the beam head expels plasma electrons and leaves behind an ion channel. The main body of the beam experiences the focusing force exerted by the uniform column of ions that are left behind. Ideally, this plasma lens is free of geometric aberration because the focusing force is linear. In a recent experiment [4], this focusing gradient reached 4×10^6 T/m with the plasma density close to 10^{19} cm^{-3}, which is far greater than 250 T/m from a conventional small aperture iron core quadrupole.

(c) Beam Steering with asymmetric ion focusing force [5]. The above mentioned ion channel can also be used to steer an REB. In such a beam steering scheme, an REB pulse traversing the ion channel has a transverse displacement with respect to the axis of the channel. Due to the asymmetric ion focusing force, the beam is steered toward the channel direction. This scheme opens up the possibility of making a fast plasma switcher of an REB.

(d) Plasma Wiggler [6]. In a conventional synchrotron that uses a magnetic wiggler or an undulator, an REB oscillates transversely due to a periodic magnetic force resulting from a series of magnetic poles while it travels longitudinally through the device. An REB can also be wiggled in a similar mannar in a plasma. The pendulum restoring force is due to the Coulomb force rather than the Lorentz force as in a wiggler/undulator. This Coulomb force can be either supplied by a plasma wave [6], or by background ions [7]. This thesis will focus on the last part of the above mentioned applications. That is: synchrotron X-ray radiation due to electron betatron motion in an ion channel.

The motivation for exploiting this kind of novel synchrotron device is as follows. Synchrotron sources are used to generate intense X-rays [8] for many applications, in the fields of biology, chemistry, material science, physics and environmental science. However these facilities are very large, complicated and expensive, and as a consequence can only be hosted at several national labs in the world. Almost all the synchrotron sources have mainly two parts: a high energy electron storage ring and undulator magnets. Whereas the storage ring provides an REB with required parameters (energy, emittance and current), the undulator magnets wiggle the REB via the Lorentz force. It has been suggested [6] that the Coulomb force can be used to replace the Lorentz force to wiggle electrons. However the required electric fields are so great that they can only be supported by a plasma. A wiggler with a plasma electric field to wiggle electrons is called a plasma wiggler. There are several schemes to realize such a wiggler [6][7][9][10]. A plasma wiggler has at least two potential advantages, smaller wiggling wavelength and larger wiggling strength in comparison with its magnetic counterpart.

The organization of the thesis is as follows. In Chapter 2, pros and the cons of a plasma wiggler with a magnetic wiggler/undulator are compared first. This is followed by a quantitative discussion of the spontaneous emission of x-rays which includes radiation power, radiation angle, and spectrum, from a plasma wiggler when an ion channel is employed. Although similar calculations have been presented elsewhere due to the similarity of trajectory of a beam electron traversing a plasma wiggler and a magnetic wiggler, these calculations are more specifically related to a specific experiment and are very helpful in analyzing the experimental data. The difference between two plasma wiggler schemes, a plasma wiggler using an ion channel [7], and a plasma wiggler using a plasma wave [6] are also addressed.

In order to experimentally demonstrate the existance of the ion channel synchrotron X-ray radiation, one needed an REB and a suitable plasma source.

While the SLAC beam provided the necessary REB, a plasma source had to be developed in which the $\sim 30\ GeV$ SLAC beam underwent at least one complete oscillation. Chapter 3 is concerned with the construction of a 1.4 meter long lithium plasma source. Such a meter long plasma source, with a uniform plasma density distribution, is a pivotal component in this and other plasma related beam handling experiments. The plasma source is essentially a $2\ m$ long heat pipe oven containing a uniform lithium metal vapor with its density tunable from $2 \times 10^{15}\ cm^{-3}$ to $6 \times 10^{15}\ cm^{-3}$. The plasma is then created by ionization of the vapor with an ArF excimer laser ($193\ nm$). Various diagnostics of vapor densities and plasma densities are discussed. All the important oven parameters, such as vapor temperature profiles, vapor density distributions, heater powers, were measured in the laboratory at UCLA.

The demonstration of X-ray emission from a plasma wiggler was carried out as a parasitic project of a PWFA experiment called E-157. The E-157 experiment is reviewed in Chapter 4. The goal of the E-157 experiment was to demonstrate high gradient acceleration of electrons in a plasma over a meter length. It used the 28.5 GeV REB from the 3-km Stanford linear Accelerator to interact with the above described 1.4 meter long plasma source with the plasma densities in the range of $10^{13} - 10^{15}\ cm^{-3}$. This experiment demonstrated almost all the important beam handling observables as mentioned earlier.

Chapter 5 details the synchrotron X-ray radiation due to electron betatron motion in the E-157 experiment. Background theory of Thomson scattering and Bragg scattering is reviewed briefly. Following that, experiments techniques including X-ray scattering and X-ray fluorescence imaging are discussed. This is followed by major experimental results of X-ray emission as a function of plasma density, the divergence angle of the beam and the absolute X-ray yield.

Is it possible to realize lasing (FEL) in a plasma wiggler? This question is briefly addressed in Chapter 6. In principle, SASE (self-amplified-stimulated-emission) [11] is possible in a plasma wiggler, and the corresponding device is named as the ion channel laser(ICL) [7]. However, there is a much more stringent requirement on beam emittance in an ICL than in a magnetic undulator which makes it difficult to realize ICL lasing in practice, particularly at short wavelengths. Preliminary simulation results on beam micro-bunching in the interval of the radiation wavelength as the beam traverse an ion channel are presented.

The conclusion drawn from this work is made in Chapter 7.

CHAPTER 2

Theory of Radiation from Electron Betatron Motion

2.1 Introduction

A relativistic electron may radiate photons when moving in a curved trajectory. This kind of radiation is normally characterized as synchrotron radiation. Synchrotron motion plays a key role in producing intense X-rays in the 10 KeV range which is not easily accessible with other light sources.

Conventional synchrotron radiation sources use a magnetic field to bend electron trajectories. Curved crystals or other devices are used to select specific frequencies from the broad spectrum of bending magnet radiation. The need for brighter sources (more photons per unit frequency interval) led to the development of magnetic devices called wigglers and undulators to be placed in the synchrotron ring. The magnetic properties of these devices cause the electrons to undergo periodic oscillatory motions that result in the concentration of the radiation into a much more monochromatic spectrum or a series of discrete frequency peaks. More details about a magnetic wiggler/undulator can be found in Appendix A.

In conventional synchrotron radiation sources, an electrostatic field has never been used to replace the magnetic field for oscillating relativistic electrons. This is because a 1 *Tesla* magnetic field, a typical value for a conventional magnet, is equivalent to a 300 MV/m electrostatic field. This is much too high to be sustained by a normal conductor material. However, this is not the case if a space charge wave in plasma is exploited as a medium to support such a large and periodic electrostatic field. Since such a plasma has already been ionized it can shield the effect of electric field on the boundary material within a few Debye lengths.

A plasma wiggler is attractive at least for two reasons. First, the effective wiggler wavelength can easily be made shorter than that of a conventional magnetic wiggler. The wiggler wavelength needs to be smaller in order to reach higher frequency radiation for a certain energy beam, in view of Eq. A.1. In the present state-of-art magnetic undulators, the minimum λ_w obtained is in the range of $0.1 \sim 1\ cm$, as is limited by the practical difficulty of placing very strong and very small permanent magnets close together in an alternating array. However, in a plasma wiggler that employs a relativistic plasma wave, a typical plasma wiggler wavelength is [12]

$$\lambda_w \sim \sqrt{\frac{\pi}{n_p \cdot r_e}} \sim \sqrt{\frac{10^{15}\ cm^3}{n_p}} \cdot mm. \tag{2.1}$$

Thus plasma density of $10^{17}\ cm^{-3}$ corresponds to a plasma wavelength $0.1\ mm$. Secondly, the effective magnetic strength B_W, which will be defined in the later section, can be extremely large in a plasma wiggler compared to a conventional magnetic wiggler. This can therefore lead to a larger efficiency of spontaneously emitted radiation for the same energy of incident electrons [1].

---

[1] The radiation efficiency is the normalized energy loss by the electron with the Lorentz factor γ as it traverses a wiggler in a length L. The efficiency can be expressed as [13]

$$\eta = \frac{\Delta E}{E} = \frac{\gamma}{3e^2} \cdot r_e^3 \cdot L \cdot {B_W}^2 \tag{2.2}$$

where r_e is the classical electron radius, $2.8 \times 10^{-13}\ cm$.

However, a plasma wiggler has disadvantages when compared to its magnetic counterpart. For instance, possible beam-plasma interactions and plasma instabilities can degrade the beam quality and therefore the brightness of the emitted radiation when a plasma wiggler is employing.

In this chapter, I describe a different type of plasma wiggler, where the electrostatic field is provided by the plasma ions rather than a plasma wave.

It is noted that an ion channel has been used in the past to guide a relativistic electron beam by balancing self-space-charge repulsion with the ion focusing force [14] [15]. Usually the ion density for this application is relatively low, in the range of $< 10^{12}\ cm^{-3}$. An ion channel has also been exploited as a plasma lens to focus charge particles [3]. The effective focusing gradient for an plasma lens in an ion channel is $B_\theta/r = 2\pi n_{ion}e \approx 3 \times 10^{-9}[\frac{n_{ion}}{cm^{-3}}][\frac{G}{cm}]$. The field can reach $100\ MG/cm$ with a plasma density $3 \times 10^{16}\ cm^{-3}$.

In this chapter, however, an ion channel is applied to wiggle an electron beam. We call this kind of device a plasma wiggler with an ion channel(PWIC).

A relativistic electron beam (REB) traversing a PWIC will radiate photons, as it does in a magnetic wiggler. This can be understood intuitively as follows. As shown in Fig. 2.1, a high density ion column sustains an electrostatic potential well around the symmetric axis of this column, which can be expressed as

$$\phi = -\pi n_{ion} e r^2 \tag{2.3}$$

The corresponding force on an electron at the position $\vec{r}$ would be

$$\vec{F}_{ion}(r) = (-e)(-\nabla\phi) = -2\pi n_{ion} e^2 \vec{r} \tag{2.4}$$

An electron propagating in this ion channel potential will undergo harmonic motion in the transverse direction. The resulting periodic acceleration leads to

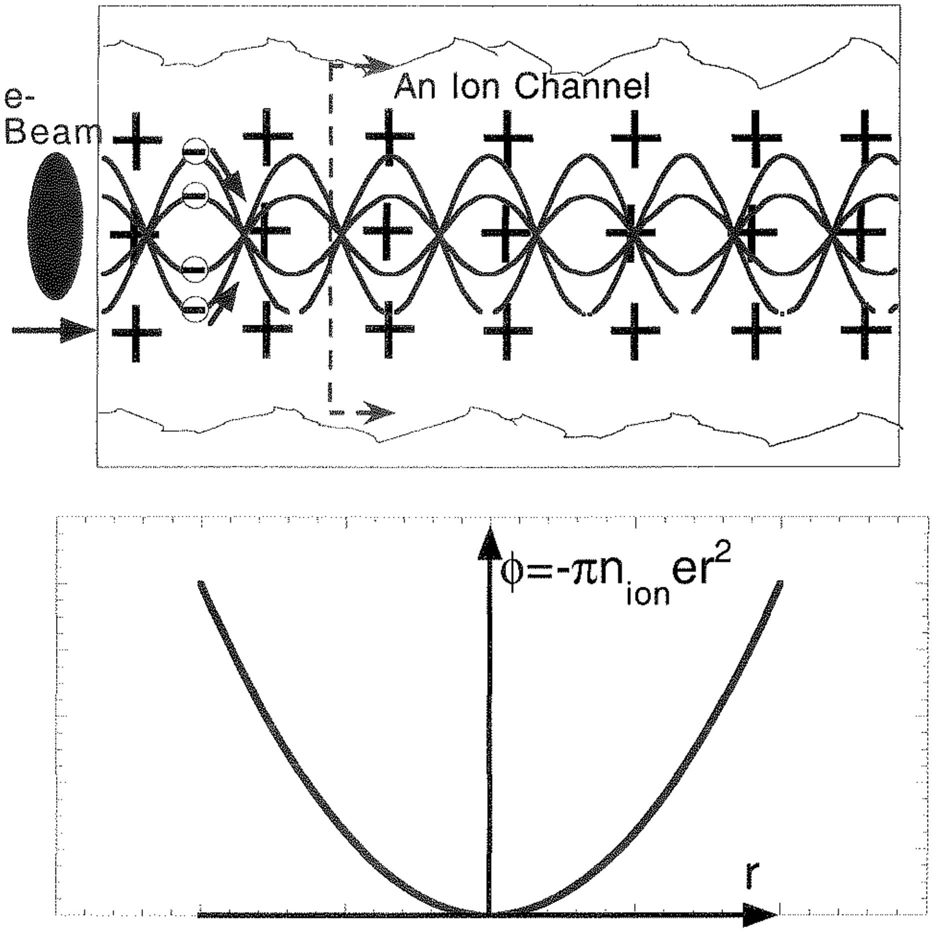

Figure 2.1: (Above) An electron beam traverses a preformed ion channel. While individual electrons are going through betatron motions with betatron frequency ω_β, the envelope of the beam oscillates with the frequency $2\omega_\beta$; (Below) The transverse profile of the potential well due to the ion column.

synchrotron radiation. Due to its relative robustness in producing an ion channel, it turns out to be the first plasma wiggler device operating in the X-ray regime realized in the experiment.

It should be noted that the synchrotron radiation of a relativistic electron beam in an ion channel has been explored theoretically in Reference [16], and stimulated radiation in an ion channel has been further developed in Reference [7]. The possibility of the realization of this stimulated radiation will be discussed in Chapter 6.

In the following sections, earlier plasma wiggler schemes are briefly reviewed first. Then a plasma wiggler with an ion channel is detailed. The formation of the ion channel and a relativistic electron motion inside the ion channel are studied with the help of the 3-D particle-in-cell simulation. The spectrum of the radiation, radiation angular distribution, etc. are numerically calculated in terms of beam and plasma parameters. Finally essentials of this plasma wiggler with an earlier proposed plasma wiggler scheme are compared.

2.2 Earlier Plasma Wiggler Schemes

In earlier plasma wiggler schemes, the plasma wiggler was essentially a relativistic plasma density wave. This plasma wave can be excited by several ways, such as by two beating laser beams, by a short laser pulse (laser wakefield scheme) or by a short pulse of relativistic electrons (plasma wakefield scheme) propagating through a plasma [17]. The plasma wave can be either parallel [9] or perpendicular [6] to the direction of the incident electron beam. The time-varying electrostatic field from this plasma wave appears like an "electromagnetic wave" in the beam frame. The beam electrons scatter these "photons" which subsquently appear as frequency shifted real photons in the laboratory frame [6].

A typical geometry of a plasma wiggler with a plasma wave (PWPW) is shown in Fig 2.2, in which the plasma wave is perpendicular to the incident electron beam. The magnitude of the electrostatic field associated with the plasma wave can be expressed as [12]

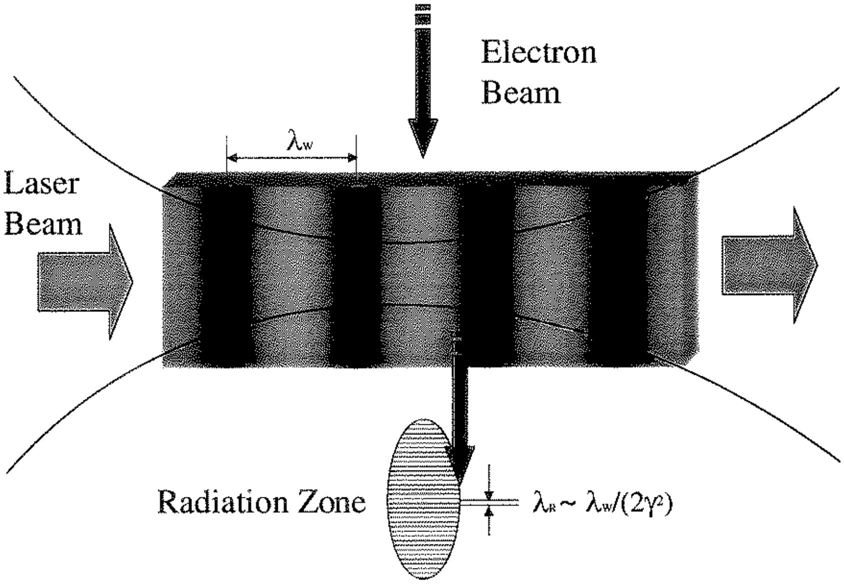

Figure 2.2: The geometry of a plasma wiggler with a plasma wave perpendicular to the direction of the relativistic electron beam. The wiggler wavelength is λ_w and ideally the radiation wavelength is $\lambda_R \sim \lambda_W/(2\gamma^2)$ due to the double doppler shift, as shown in Eq. A.1. The electron beam drifts in the direction that the plasma wave moves due to the net poderomotive force [12].

$$E_{pw} = E_p sin(\omega_p t) \approx \frac{4\pi e \delta n_p}{\omega_p/c} sin(\omega_p t), \tag{2.5}$$

where δn_p is the perturbed plasma electron density. The second equation in Eq. 2.5 is obtained from 1-D Poisson's equation: $\nabla \cdot \vec{E} = -4\pi e \delta n_p$. The maximum density rarefaction occurs when $\delta n_p = n_p$ with n_p the plasma density, known as the cold plasma wavebreaking limit [18]. This electrostatic field wiggles the beam electrons transversely with the frequency ω_p. Since both the phase velocity of the plasma wave v_{ph} and the velocity of the relativistic electrons v_g are very close to the speed of light in vacuum c, the corresponding wiggler wavelength is just the plasma wave wavelength,

$$\lambda_w = 2\pi c/\omega_p. \tag{2.6}$$

The effective magnet strength in such kind of a plasma wiggler is

$$B_{eff} = \frac{4\pi e \delta n_p}{\omega_p/c} sin(\omega_p t) \approx 3 \times 10^{-3} \sqrt{\frac{n_0}{cm^{-3}}} (gauss), \tag{2.7}$$

where $B_{eff} = E_{pw} c/v_{ph} \approx E_{pw}$. The corresponding radiation wavelength and its harmonics due to this wiggling motion is expressed as

$$\lambda_r = m\lambda_0 \approx \frac{m\lambda_w}{2\gamma^2} \tag{2.8}$$

with m the harmonic number, due to the double Doppler shift (referring to Appendix A). It is interesting to note that in such a kind of plasma wiggler, in the linear approximation, the effective wiggler strength K is always no more than one, since

$$K_{pw} = \frac{e\lambda_w E_{pw}}{2\pi mc^2} \approx \frac{\delta n_p}{n_p} \tag{2.9}$$

in view of Eq. A.4, and 2.5. Therefore, the spectrum of the radiation tends to be discrete, and the bandwidth of each spike depends on the number of wiggler periods. The pulse width of the radiation is the same as the incident electron pulse width.

The challenge to realize such a kind of plasma wiggler is to produce a uniform and transversely wide plasma wave. So far there is not any experiment demonstrating this scheme.

2.3 A Plasma Wiggler with an Ion Channel (PWIC)

2.3.1 The Formation of an Ion Channel

Now I will discuss an alternative method of producing a plasma wiggler: an ion column. A conventional method to produce a high-density ion column channel is to shoot a dense relativistic electron beam (REB) into plasma, the head of which pushes plasma electrons away and leaves behind plasma ions. If the REB density n_b is larger than the plasma density n_p, plasma is said to be in the underdense condition, plasma electrons are expelled transversely and stream backward to neutralize the ions. If the REB is also so narrow that its RMS size σ_r satisfies $\omega_p \sigma_r / c << 1$ [2], the plasma return current flows mainly outside the beam. An ion channel is therefore left inside this plasma sheath.

The transverse size of the ion channel can be simply estimated by realizing that a plasma electron at the edge of the channel receives zero net transverse force, i.e.,

$$\vec{F_\perp} = F_{REB}\hat{r} + F_{ion}\hat{r} = (\frac{4\pi{\sigma_r}^2 n_b e^2}{b}(1+\frac{v_p}{c}) - 2\pi b n_p e^2)\hat{r} = 0, \qquad (2.10)$$

where the REB is assumed to have a Gaussian distribution transversely with its RMS size σ_r, b is the radius of the ion channel, v_p is the longitudinal velocity of the plasma electron directing opposite to the REB velocity. The above equation gives the ratio of the radius of the ion channel and the radius of the REB as

$$\frac{b}{\sigma_r} = \sqrt{\frac{2(1+\frac{v_p}{c})n_b}{n_p}}, \qquad (2.11)$$

which can be further simplified as

$$\frac{b}{\sigma_r} = \sqrt{\frac{2n_b}{n_p}}, \qquad (2.12)$$

---

[2] A regime with both the above mentioned conditions satisfied, i.e., $n_b > n_p$ and $\omega_p \sigma_r / c <<$ 1, is often called a "blow-out" regime.

since $v_p/c << 1$ is true in most cases. Plasma electrons stream backward to neutralize ions. The time scale for these electrons to return back to the channel is $1/\omega_p$. Therefore the main body of a short REB ($\sigma_z < \pi c\omega_p$), or any REB trailing behind with a distance shorter than $\pi c/\omega_p$ would propagate inside an ion channel.

The formation of the ion channel was demonstrated in the computer simulation with a 3-D Particle-In-Cell simulation code, called QUICKPIC [19]. The beam and plasma parameters used in the simulation are as follows. An REB with the Lorentz factor $\gamma = 60000$ contained 1.8×10^{10} electrons. It had Gaussian density distributions both transversely and longitudinally with $\sigma_r = 40\ \mu m$ and $\sigma_z = 0.7\ mm$, respectively. The density of the plasma was varied from about $10^{12}\ cm^{-3}$ to $2 \times 10^{14}\ cm^{-3}$. These are the typical parameters of the E-157 experiment [20], which will be detailed in Chapter 4. Fig. 2.3 is a snapshot demonstrating both the beam and plasma density distribution inside the simulation window as the REB propagated through the plasma. As the front of the beam expelled the plasma electrons away and experiencing dynamic ion densities, the main body of beam electrons were experiencing an ion column with a uniform ion density.

The transverse force witnessed by a beam electron which was σ_z from the beam center in the longitudinal direction is shown in Fig. 2.4 as the function of the distance from the axis of the ion channel. The force is linearly proportional to the distance from the axis of the ion channel r, as mentioned earlier in Eq. 2.4. Further away from the axis and beyond the edge of the channel, the force decays due to shielding of plasma electrons as expected [21]. The transverse force witnessed by a beam electron which is σ_r from the beam center in the transverse direction is drawn in Fig. 2.5. The scanning routine to yield the above figure

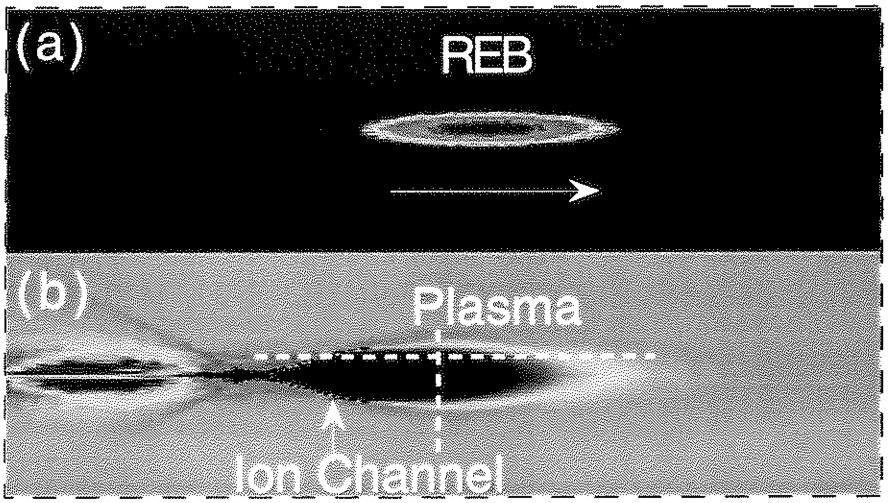

Figure 2.3: A snapshot of (a) the beam density distribution and (b) the plasma density distribution inside a simulation window with the QUICKPIC code. The dashed lines in (b) indicate the transverse and longitudinal positions where the fields in Fig. 2.4 and 2.5 are plotted.

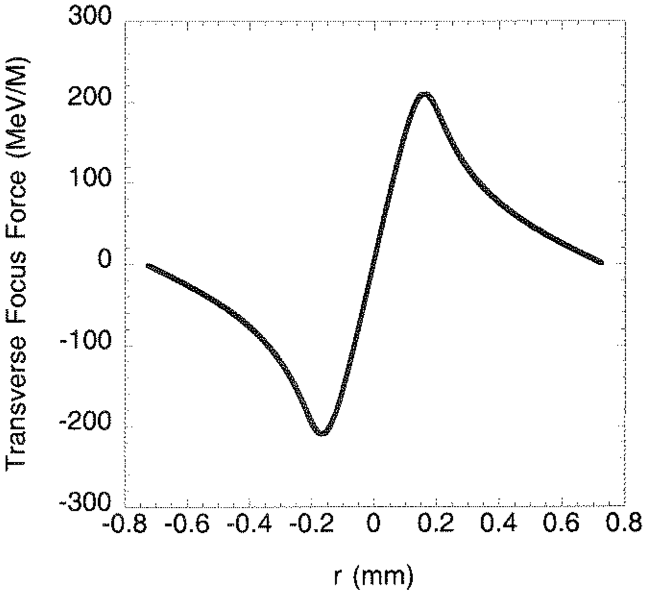

Figure 2.4: The transverse force as the function of the distance from the axis of the ion channel. The scanning routine to yield the above figure is indicated as the vertical dash line in Fig. 2.3(b).

is indicated as the horizontal line in Fig. 2.3(b). The beam charge distribution along the ion channel is also drawn in Fig. 2.5. As shown in Fig. 2.5, the main

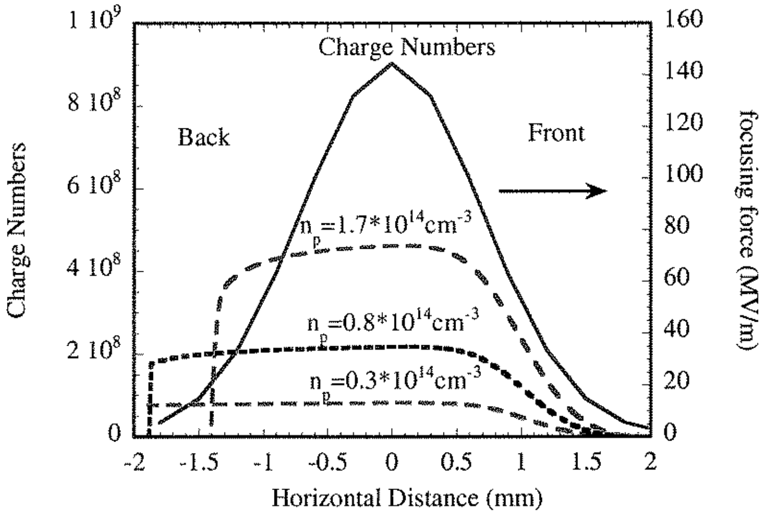

Figure 2.5: Beam charge distribution along the ion channel, and the transverse forces witnessed by a beam electron, which was σ_r from the beam center in the transverse direction, at 3 different plasma densities.

body of the beam experiences an almost constant ion focusing force along the ion channel over the wide range of densities used in the experiment[3]. The length of the ion channel is shorter as the plasma density is larger, as indicated by Fig. 2.5. This is because the time scale for plasma electrons to rush back to the channel is $\sim 1/\omega_p$, which is proportional to the plasma density. As the plasma electrons rush back they produce a plasma density spike on the axis of the ion channel with the consequent defocusing force on the plasma electrons.

---

[3] The slight difference of the focusing force along the channel at the highest ion density $1.7 \times 10^{14}\ cm^{-3}$, as shown in Fig. 2.5, is due to the head-to-tail tilt of the incident REB. An REB with a head-to-tail tilt was very common in the E-157 experiment.

2.3.2 Electron Betatron Motion Inside an Ion Channel

As an REB traverses an ion channel, the beam electron receives two kinds of forces: the Lorentz force due to self-fields of the beam and the ion focusing force. However, the ion focusing force dominates the Lorentz force provided that the ion density n_{ion} satisfies $n_{ion} >> n_b/\gamma^2$. The above equation is called Budker condition [22], which is assumed to be true in a PWIC.

Therefore with the zero-order approximation, the following equations govern the motion of a beam electron in an ion channel,

$$\frac{d\gamma c\beta_r}{dt} = \frac{-\omega_p^2 r}{2}, \tag{2.13}$$

$$\frac{d\gamma}{dt} = -\frac{c\beta_r k_p^2 r}{2}, \tag{2.14}$$

and

$$\frac{d\gamma\beta_z}{dt} = 0, \tag{2.15}$$

with β_r and β_z the normalized velocity of the electron in the transverse and longitudinal directions respectively. It is noted that in a magnetic wiggler, the total energy of a beam electron is constant, while its axial momentum varies; whereas in a PWIC, the electron's total energy varies but its axial momentum remains constant.

Provided that the transverse velocity of the electron $c\beta_r$ is non-relativistic, i.e., $\beta_r << 1$, the above equations can be solved explicitly and lead to simple harmonic solutions under the initial condition that $r = r_0$, $\beta_r = 0$, $\beta_z = \beta_{z0}$, $\gamma = \gamma_0$, at $t = 0$. These solutions are

$$r = r_0 \cdot \cos\xi, \tag{2.16}$$

$$\beta_r = -r_0 k_\beta \sin\xi, \tag{2.17}$$

$$\gamma = \gamma_0 + \frac{\gamma_0 (r_0 \cdot k_\beta)^2}{2}(1 - \cos(2\xi)), \tag{2.18}$$

sand

$$\beta_z = \beta_{z0}(1 - \frac{r_0^2 k_\beta^2}{4}) + \frac{\beta_{z0}^2 r_0^2 k_\beta^2}{4} \cos(2\xi) = \bar{\beta}_z + \frac{\beta_{z0}^2 r_0^2 k_\beta^2}{4} \cos(2\xi), \tag{2.19}$$

where $d\xi/dt = \omega_\beta = \omega_p/\sqrt{2\gamma}$, and $k_\beta = \omega_\beta/c = \omega_p/(\sqrt{2\gamma}c)$.

It is interesting to note that equations 2.16, 2.17, and 2.19 are identical to the description of an electron motion inside a magnetic wiggler even though it is governed by different conservation laws.

2.3.3 Spontaneous Radiation from Betatron Motion

Based on equations 2.16, 2.17, and 2.19, The single electron trajectory of an REB in an ion channel is given by

$$k_\beta \vec{r}(t) = (a_x \cos\xi,\ 0,\ (1 - \frac{1}{2\gamma^2} - \frac{a_x^2}{4})\xi + \frac{a_x^2}{8}\sin 2\xi), \tag{2.20}$$

where a_x is the normalized initial radius of the electron with $a_x = k_\beta r_0$. Without losing generality, it is assumed that the electron trajectory is in the vertical (x-z) plane, as shown in Fig 2.6. The observation direction $\hat{n}$ has a vertical angle ϕ and a horizontal angle ψ, and can be expressed as $\hat{n} = (\phi, \psi, 1 - \theta^2/2)$ with θ the azimuthal angle satisfying $\theta^2 = \phi^2 + \psi^2$.

In view of the trajectory as described in Eq. 2.20, the radiation power from an electron is [23]

$$P(t) = \frac{2e^2\gamma^2}{3m^2c^3}[\dot{\vec{p}}^2 - m^2c^2\dot{\gamma}^2] \approx \frac{2e^2\gamma^2\dot{p}_x^2}{3m^2c^3} \approx \frac{2c}{3}e^2\gamma^4x^2k_\beta^4\cos^2\xi. \tag{2.21}$$

Therefore the average power over the integral number of the betatron period is

$$\bar{P} = \frac{c}{3}e^2\gamma^4x^2k_\beta^4. \tag{2.22}$$

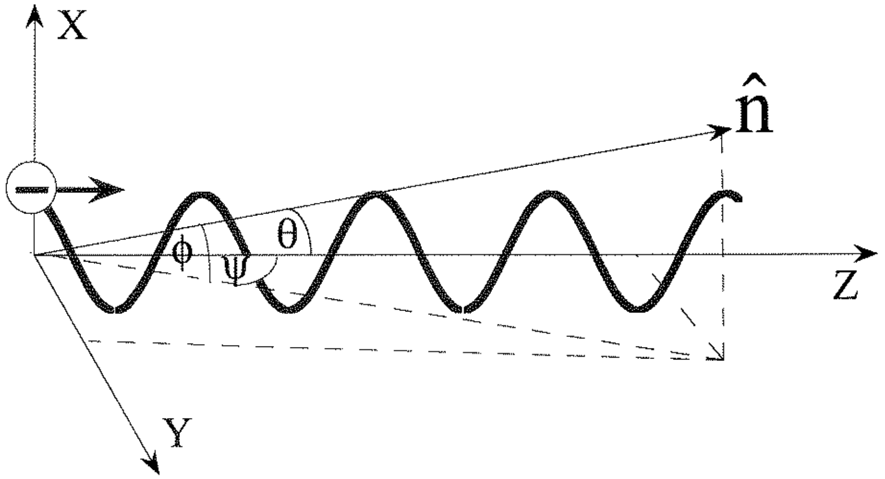

Figure 2.6: The coordinate system with $\hat{n}$ the direction of the observation. An electron's trajectory is assumed to be in the x-z plane without losing generality.

The radiation power is proportional to k_β^4, and therefore to the square of the plasma density. The radiation efficiency is

$$\eta = \frac{\bar{P} \cdot (L/c)}{\gamma m c^2}, \tag{2.23}$$

or

$$\eta = 5.8 \cdot 10^{-11} \cdot [\frac{E}{GeV}][\frac{n_p}{10^{15} cm^{-3}}]^2 [\frac{x}{\mu m}]^2 [\frac{L}{m}] \tag{2.24}$$

in practical units. The total radiation power from an REB with the beam size σ_r, and the current I is

$$P = \eta(\sigma_r) \cdot E_{beam} \cdot \frac{I}{e}, \tag{2.25}$$

and is

$$P(KW) = 0.58 \cdot [\frac{E}{GeV}]^2 [\frac{n_p}{10^{15} cm^{-3}}]^2 [\frac{\sigma_r}{\mu m}]^2 [\frac{I}{KA}][\frac{L}{m}] \tag{2.26}$$

in practical units. Here it is assumed that there are no phase relations among the radiation fields emitted by each electron. Therefore the total radiation power is the sum of radiation power emitted by each electron.

The normalized wiggler strength seen by an electron, according to the definition of Eq. A.2 is

$$K_s = \gamma_b \omega_\beta r_0 / c. \tag{2.27}$$

The wiggler strength for an REB, which has a Gaussian distribution around the axis of the ion channel with its transverse RMS size σ_r, is

$$\langle K \rangle \approx \gamma_b \omega_\beta \sigma_r / c, \tag{2.28}$$

and is

$$\langle K \rangle \approx 0.186 \cdot [\frac{E}{GeV}]^{1/2} [\frac{n_p}{10^{15} cm^{-3}}][\frac{\sigma_r}{\mu m}] \tag{2.29}$$

in practical units. For comparison, the wiggler strength of an REB in a conventional magnet wiggler is given as

$$K_{magnet} = \frac{eB}{k_u mc} = 0.934[\frac{\lambda_u}{cm}][\frac{B_0}{T}]. \tag{2.30}$$

It should be noted that the wiggler strength in a PWIC depends on the beam energy and the beam spot size, while in a magnetic wiggler it does not.

The angular distribution of radiation from an electron in an ion channel is similar to that in a magnetic wiggler. The angular opening of the radiation is about $1/\gamma$ on the horizontal plane ($\psi = 0$), and the radiation beyond this angle is not significant based on the time-contraction effect. The vertical angle opening $\Delta\phi$ depends on the magnitude of the electron's deflection angle. The deflection angle ϕ_d of the electron satisfies

$$\phi_d = \frac{|v_x|}{c} = a_x |\sin \xi| = \frac{K_s}{\gamma} |\sin \xi|. \tag{2.31}$$

$\Delta\phi$ is about $1/\gamma$ if $K_s < 1$, and is about K_s/γ if $K_s > 1$.

The angular radiation of a plasma wiggler can be understood more quantitatively by adopting the equation of angular radiation of a bending magnet [23],

$$\frac{dI}{d\psi d\phi} = \frac{7m_p}{16} \frac{e^2}{\rho} \frac{1}{(1/\gamma^2 + \psi^2)^{5/2}} [1 + \frac{5}{7} \frac{\psi^2}{(1/\gamma^2 + \psi^2)}], \tag{2.32}$$

where m_p is the number of period of the betatron motion, and ρ is the radius of the curvature of the betatron motion satisfying $\rho^{-1} \approx a_x k_\beta \sqrt{1 - \phi^2/a_x^2}$, with ϕ is the observation angle as shown in Fig. 2.6 [4].

Figure 2.7(a) is the visualization of the angular distribution of the radiation from a single electron with $K_s = 5$, based on Eq. 2.32. Figure 2.7(b) is the visualization of the angular distribution of the radiation from an REB with $\langle K \rangle = \gamma\sigma_r = 5$. The radiation from an REB is the sum of the radiation from each electron, and therefore is symmetrically distributed with the solid angle about $\langle K \rangle/\gamma$.

The radiation spectrum in a PWIC is calculated as follows. It is known that the normalized radiation intensity I per unit solid angle $d\Omega$ and per unit frequency interval $d\omega$ emitted by a single electron in an arbitrary orbit $\vec{r}(t)$ and $\vec{\beta}(t)$ can be calculated from the Lienard-Wiechart potentials [23],

$$\frac{d^2 I}{d\omega d\phi d\psi} = \omega^2 \left| \int \hat{n} \times (\hat{n} \times \vec{\beta}) e^{i\omega(t - \frac{\hat{n}\cdot\vec{r}}{c})} dt \right|^2, \tag{2.35}$$

where the radiation intensity is normalized to $e^2/(4\pi^2 c)$. Since the trajectory of an electron traversing an ion channel is described by equations 2.16, 2.17, and 2.19, therefore the radiation spectrum from an electron traversing an ion channel

---

[4] The radiation from a wiggler is equivalent to that from a sequence of bending magnets provided that $K_s > 1$. As $K_s > 1$, the time-contraction becomes nonuniform and concentrated in small portions of the trajectory slope is within an angle γ^{-1} to the observation direction [25]. ρ satisfies

$$\frac{1}{\rho} = \frac{|\dot{v}_\perp|}{c^2} = a_x k_\beta |\cos\xi|, \tag{2.33}$$

with $d\xi/dt = \omega_\beta$. The radius of the trajectory slope within an angle γ^{-1} of an observer's view is a function of ϕ, therefore, can be approximated as

$$\frac{1}{\rho} \approx a_x k_\beta \sqrt{1 - \phi^2/a_x^2}, \tag{2.34}$$

provided that $|\phi| \leq a_x$.

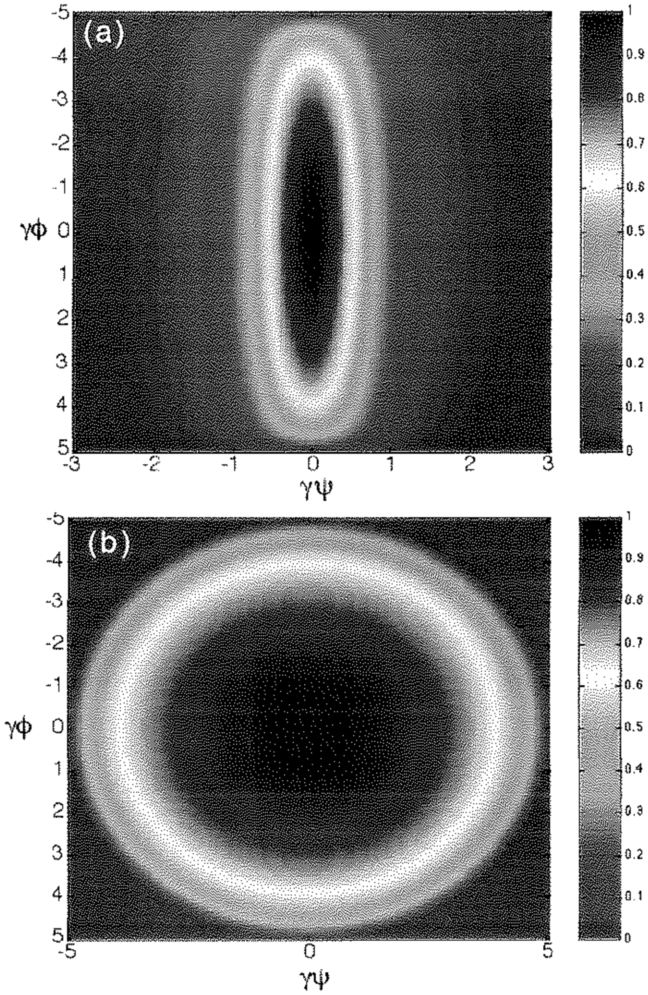

Figure 2.7: (a) The angular distribution of the radiation from an electron with $K_s = 5$, based on Eq. 2.32. The trajectory of the electron's betatron motion is assumed to be in the x-z plane. ϕ is the angle between the observation direction and the y-z plane, while ψ is the angle between the observation direction and the x-z plane. (b) The angular distribution of the radiation from an REB with $\langle K \rangle = 5$.

is

$$\frac{d^2I}{d\omega d\phi d\psi} = \frac{e^2\omega_N^2}{4\pi^2 c}|A_\sigma(\omega_N)\hat{e}_x + A_\pi(\omega_N)\hat{e}_y|^2, \tag{2.36}$$

where

$$A_\sigma(\omega_N) = \int_{-T}^{T} (\varphi - \beta_x) \cdot e^{i(p_1\xi + p_2\cos\xi + p_3\sin(2\xi))} d\xi \tag{2.37}$$

$$A_\pi(\omega_N) = \int_{-T}^{T} \psi \cdot e^{i(p_1\xi + p_2\cos\xi + p_3\sin(2\xi))} d\xi. \tag{2.38}$$

In above equations, $\xi = \omega_\beta t + \xi_0$, $\omega_N = \omega/\omega_\beta$, $p_1 = \omega_N[(\phi^2 + \psi^2)/2 + 1/(2\gamma^2) + {a_x}^2/4]$, $p_2 = \omega_N a_x \phi$, $p_3 = \omega_N {a_x}^2/8$, and $T = k_\beta L/2$. A_σ and A_π represent the amplitude of the radiation polarized in the plane of trajectory and polarized perpendicular to the plane of trajectory respectively. Normally $|A_\pi| << |A_\sigma|$. As $K_s = \gamma a_x < 1$, both p_2 and p_3 are small and the radiation is peaked at the radiation frequency ω_1 which can be deduced by setting $p_1 = 1$. ω_1 satisfies

$$\omega_1 = \frac{2\gamma^2\omega_\beta}{1 + K_s^2/2 + (\gamma\theta)^2} \tag{2.39}$$

Harmonic radiations at $\omega_m = m\omega_1$ may occur due to the non-zero values of p_2 and p_3, whereas p_2 contributes to the even harmonics and p_3 to the odd harmonics. Based on Eq. 2.36, the radiation spectrum for an electron with its wiggler strength $K_s = 0.78$ and its interaction length $k_\beta L = 3\pi$ is numerically calculated and plotted as the function of the normalized frequency $\omega/(2\gamma^2)\omega_\beta$ and normalized observation angle. Figure 2.8 demonstrates the normalized radiation intensity in the horizontal ($\psi = 0$) plane, whereas Fig. 2.9 in the vertical plane ($\phi = 0$).

It shows in the above two figures that the even harmonics appear in the $\psi = 0$ plane, which is the plane of the electron's trajectory, but disappear in the $\phi = 0$ plane. This is due to the fact that p_2, which contributes to the even harmonics, is zero at $\phi = 0$. It also shows that significant radiation occurs only at the fundamental frequency ω_1, and is confined to an angle smaller than $1/\gamma$.

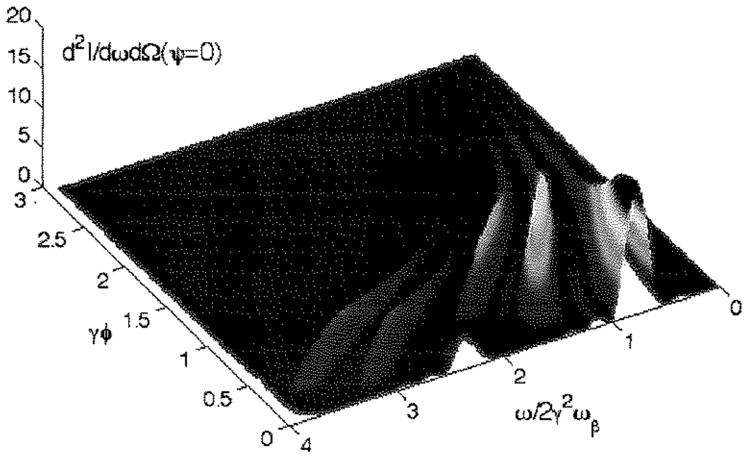

Figure 2.8: The normalized radiation intensity based on the numerical integration of Eq. 2.36, as a function of the normalized frequency $\omega/(2\gamma^2\omega_\beta)$ and the angle $\gamma\phi$ in the $\psi = 0$ plane. The wiggler strength $K_s = 0.78$ and the interaction length $L = 3\pi/k_\beta$.

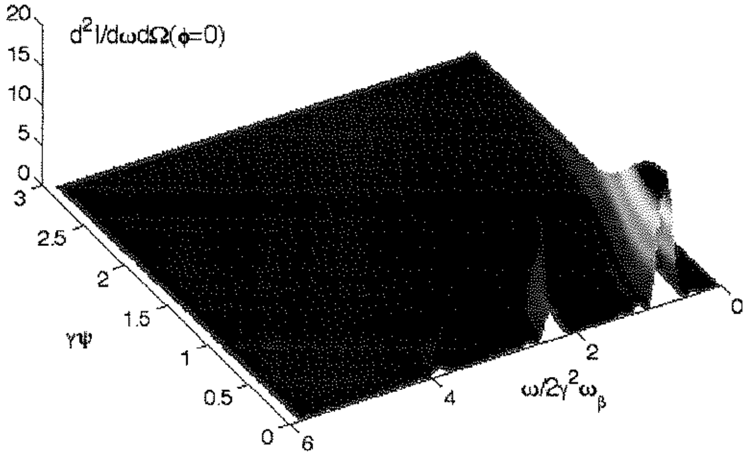

Figure 2.9: The normalized radiation intensity based on the numerical integration of Eq. 2.36, as a function of the normalized frequency $\omega/(2\gamma^2\omega_\beta)$ and the angle $\gamma\psi$ in the $\phi = 0$ plane. The wiggler strength $K_s = 0.78$ and the interaction length $L = 3\pi/k_\beta$.

Both figures demonstrate that the harmonic peaks get closer and the radiation frequencies get smaller at larger observation angles. The bandwidth of each radiation peak in the spectrum is due to the limited number of the electron's betatron oscillation periods.

As $K_s \geq 1$, significant radiation occurs in the harmonics as well as the fundamental. The angular distribution of the higher harmonics is more broader than that of the fundamental. At the same time, the peak-to-peak line separation is closer because $\Delta\omega = \omega_1$ is smaller as K_s is bigger, referring to Eq. 2.39. The normalized radiation intensity for an electron with its wiggler strength $K = 1.17$ and its interaction length $k_\beta L = 3\pi$ is plotted in Fig. 2.10 and 2.11 in the $\psi = 0$ and $\phi = 0$ plane respectively.

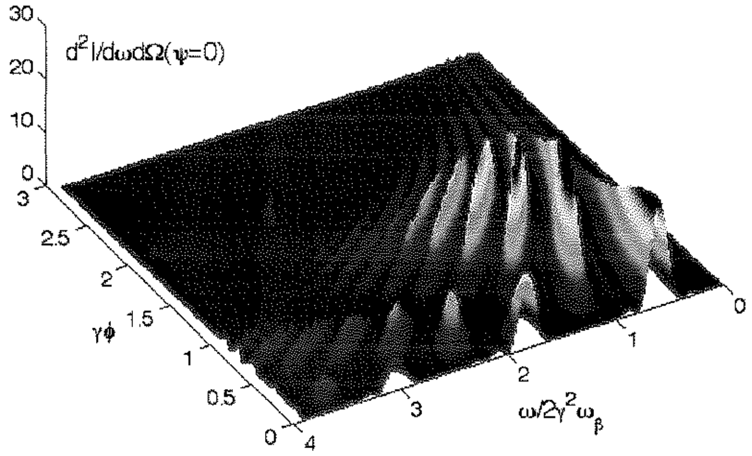

Figure 2.10: Same as Figure 2.8 except that the wiggler strength $K_s = 1.17$.

As $K_s > 1$, high harmonics of radiation dominates and the resulting synchrotron radiation consists of many closely spaced harmonics. Finite wiggler pe-

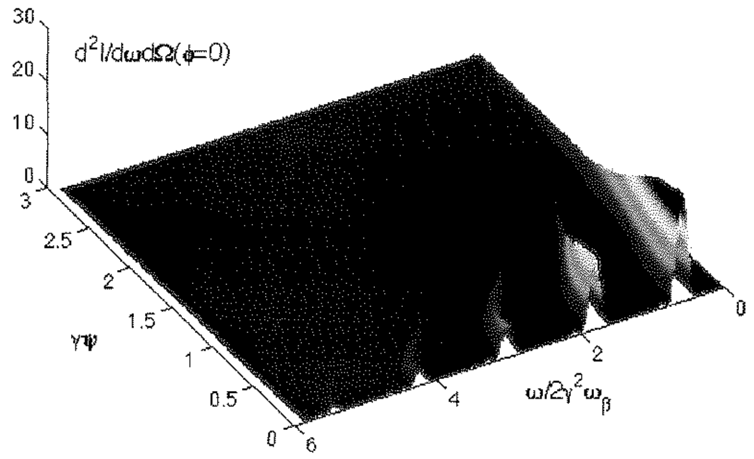

Figure 2.11: Same as Figure 2.9 except that the wiggler strength $K_s = 1.17$.

riods further broaden the linewidth causing the radiation from various harmonics to overlap. Hence, in the $K_s > 1$ case, the gross spectrum appears broadband and a continuum of radiation is generated. Numerical integration of Eq. 2.36 becomes cumbersome since the integral part becomes a very fast oscillating function as $K_s > 1$. Instead, the spectrum of Eq.2.35 under the condition of $K_s > 1$, can be asymptotically expressed as [24]

$$\frac{d^2I}{d\omega d\phi d\psi} = m_p \frac{e^2\omega^2\rho^2}{3\pi^2c^3}(\frac{1}{\gamma^2} + \theta^2)^2(K_{2/3}{}^2(\zeta) + \frac{\theta^2}{(1/\gamma^2 + \theta^2)}K_{1/3}{}^2(\zeta)), \qquad (2.40)$$

with ζ satisfying $\zeta = \frac{\omega\rho}{3c}(\frac{1}{\gamma^2} + \theta^2)^2$, m_p the period number satisfying $k_\beta L = m_p\pi$, ρ the curvature radius satisfying Eq. 2.33. The radiation spectrum from an electron with $K_s = 5.9$, based on Eq. 2.40, is plotted in Fig. 2.12. In contrast to the $K_s < 1$ case, the spectrum with $K_s > 1$ is broad in both frequency and angle. This broadband radiation extends to a critical frequency beyond which

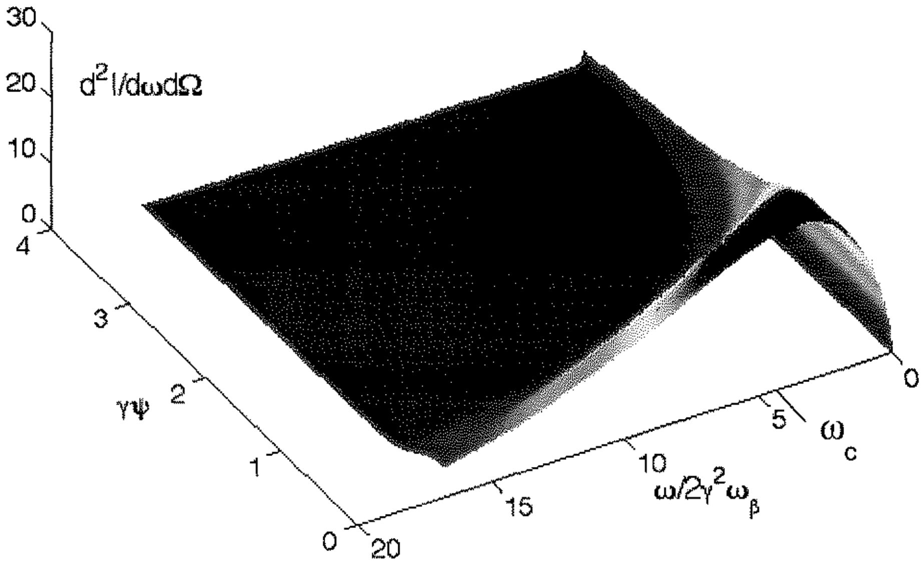

Figure 2.12: The normalized radiation intensity based on the numerical integration of Eq. 2.40, as a function of the normalized frequency $\omega/(2\gamma^2\omega_\beta)$ and the angle $\gamma\psi$ in the $\phi = 0$ plane. The wiggler strength $K_s = 5.9$ and the interaction length $L = 3\pi/k_\beta$.

the radiation intensity diminishes. The cut-off frequency can be expressed as

$$\omega_c = \frac{3\gamma^3 c}{2\rho}, \tag{2.41}$$

where ρ is the the curvature of the betatron motion as addressed in Eq. 2.32. This cut-off frequency, if observed on-axis ($\vec{n} = \vec{z}$), can be expressed in practical units[5], as,

$$(\hbar\omega_c)(keV) \approx 0.2 \cdot [\frac{E}{GeV}]^2[\frac{n_p}{10^{15}cm^{-3}}][\frac{r_0}{\mu m}] \tag{2.43}$$

As reasoned before, the radiation spectrum from an REB traversing an ion channel is equal to the sum of the spectrum from each electron in the REB. The spectrum from an REB that has a finite transverse beam size will be further broadened compared with the spectrum emitted by one electron. This is due to the fact that each electron radiate at different ω_1 because K_s depends on the transverse radius, referring to Eq. 2.39. Therefore the individual radiation spikes from each electron in the REB overlap with each other and hence the radiation bandwidth is broadened. This effect is more severe as the average wiggler strength of the REB $\langle K \rangle > 1$. It should also be noted that the polarization of the radiation from an REB particularly with a Gaussian distribution around the axis of the ion channel is unpolarized. This is because the trajectory of each electron's betatron motion may lie in the plane different from that of the other electron's.

Based on the radiation spectrum from an REB traversing an ion channel, the photon flux F, defined as the number of photons per second within a specified bandwidth, and the photon spectral brightness B, defined as the phase space

---

[5] In comparison, the critical photon energy corresponding to a bending magnet or a magnet wiggler is also given as

$$(\hbar\omega_c)(KeV) \approx 0.67 \cdot [\frac{E}{GeV}]^2[\frac{B}{T}]. \tag{2.42}$$

Therefore a 10^{15} cm^3 ion channel provides a magnet force equivalent to that a 30 $Tesla$ magnet does on a relativistic electron with a displacement from the axis of the ion channel $30\mu m$.

density of the photon flux can be calculated. According to the definition, the photon flux F and the brightness B satisfy

$$F(\omega) = (\frac{I_b}{e})(\frac{\Delta\omega}{\hbar\omega}) \int (\frac{dI}{d\omega d\phi d\psi}) d\phi d\psi, \tag{2.44}$$

with I_b the REB current, and

$$B(\omega) = \frac{F(\omega)}{S}, \tag{2.45}$$

where S is the effective phase area of the radiation source. The phase area S for an REB with its RMS beam size σ_r traversing an ion channel with the distance L can be derived based on equations given in the reference[25]

$$S \approx \pi(\sigma_r^2 + \frac{1}{4}((\epsilon/\sigma_r)^2 + (\alpha/\gamma)^2)L^2), \tag{2.46}$$

where ϵ is the geometrical emittance of the beam, and α is a constant describing the effect of the electron betatron motion on the phase area. If the REB is a phase-matched beam[6], $\alpha = 0$. If the beam is mismatched, $0 < \alpha < K$, depending on the radiation frequency. The radiation with higher frequencies are concentrated on the inner part of the radiation core and the corresponding α is small, whereas the radiation with a lower frequency has a larger α. The maximum value of α is approximately equal to K since the largest deflection angle of an electron is K/γ, based on Eq. 2.31.

---

[6] The REB is matched in an ICL when the ion focused force is balanced by the outward force due to beam emittance [26], i.e.,

$$\frac{d\vec{P}_r}{dt} = \vec{F}_{in} - \vec{F}_{out} = -\frac{m_e\omega_p^2}{2}\vec{r} + \frac{m_e c^2 \epsilon^2}{\beta_b^2 r^4}\vec{r} = 0, \tag{2.47}$$

where ϵ is the emittance of the REB. The corresponding matched radius of the beam is given by

$$r_0 = (\frac{\epsilon}{k_\beta})^{1/2}. \tag{2.48}$$

The photon flux defined in Eq. 2.44 can be numerically calculated in view of Eq. 2.35. However, for a PWIC with $\langle K \rangle > 1$, Eq. 2.44 can be asymptotically processed and yield [27]

$$F(\omega) = m_p[\frac{dN_{ph}(\omega)}{d\psi}]\langle \Delta\psi \rangle = m_p \cdot C_\psi \cdot I \cdot E \cdot \frac{\Delta\omega}{\omega} \cdot S(\omega/\omega_c) \cdot \langle \Delta\psi \rangle, \qquad (2.49)$$

where

$$C_\psi = 3.967 \cdot 10^{16} \frac{photons}{\sec \cdot mrad \cdot A \cdot GeV}, \qquad (2.50)$$

$S(\omega/\omega_c)$ is the universal function satisfying

$$S(\frac{\omega}{\omega_c}) = \frac{9\sqrt{3}\omega}{8\pi\omega_c} \int_{\frac{\omega}{\omega_c}}^{\infty} K_{5/3}(x)dx, \qquad (2.51)$$

and $\langle \Delta\psi \rangle$ is the average of the deflection angles of the electrons in the REB, which is $\sim K/\gamma$.

Using the above equations we show in Table 2.1 what might be achievable using the SLAC beam in the near future.

It should be noted that in estimating the radiated power in the above example, it is assumed that the ion channel is preformed. If the REB itself is used to form the ion channel, the front part of the beam may not experience focusing force of the fully formed ion channel, and therefore the overall radiation efficiency may be somewhat lower.

2.4 The Comparison Between a PWIC and a PWPW

In this section, the main characteristics of a plasma wiggler with an ion channel (PWIC) and a wiggler with a plasma wave (PWPW) are compared.

Both plasma wigglers exploit collective electrostatic fields to wiggle electrons to produce synchrotron radiation. In both cases the output radiation frequency

Beam Parameters		
Beam energy	30 GeV	
Charge per bunch	3.2 nC	
Transverse Emittance (Normalized)	50 $mm - mrad$	
Bunch length (RMS)	300 $fsec$	30 $fsec$
Beam size (RMS)	30 μm	
Plasma parameters		
Plasma density n_p	$6 \times 10^{15}\ cm^{-3}$	
Plasma length L_p	50 cm	
X-ray parameters		
Wiggler strength K	75	
Photon critical energy E$_c$	3.2 MeV	
Peak flux distribution at E_c $(photons/(sec \cdot 0.1\% bandwidth)$	5.3×10^{16}	5.3×10^{17}
Peak brightness at E$_c$ (photons/$(sec \cdot mrad^2 \cdot mm^2 \cdot 0.1\% bandwidth)$	3.9×10^{19}	3.9×10^{20}
Radiation power (Watt)	1.8×10^{11}	1.8×10^{12}
Radiation efficiency	5.6×10^{-4}	

Table 2.1: Parameters for a designed PWIC radiated in the hard x-ray region based on the SLAC beam parameters.

can be tuned by simply changing the plasma density and therefore the wiggler wavelength. Of course, both schemes are vulnerable to plasma related instabilities such as the electron hose instability [28], and the two stream instability, etc.. These instabilities may limit the electron-photon interaction lengths.

The main difference between two schemes is the wiggler strength. In a PWIC, $K = \sqrt{\gamma_b \omega_p / 2} r_0 / c$ with r_0 the displacement from the symmetric axis of a single electron. While in a PWPW, $K = n_1/n_0$ in a PWPW with n_1 the perturbed plasma density. Therefore each electron with different r_0 has different K in a PWIC, while K in a PWPW is independent of the characteristics of the beam electrons. Consequently, beam electrons react more collectively in a PWPW than in a PWIC. This collective behavior is schematically shown more clearly in Fig. 2.13. In a PWIC, different electrons go through different trajectories and the envelope of the beam varies periodically. In a PWPW, beam electrons have identical trajectories and the whole body of the beam moves in a sinusoidal motion. As we know in the SASE (spontaneous amplified stimulated lasing) mechanism, this collective motion may eventually lead to the interaction between radiation field and beam itself. The interaction leads to electron bunching on the radiated scale length and enhances the radiation further. Due to the the above reason, a PWIC appears to be a more suitable candidate for a short-wavelength, broad-band, high flux wiggler, while a PWPW is more suitable for a narrow-band, high brightness undulator and a better candidate of a plasma SASE laser. The characteristics of both wigglers are summarized in Table 2.2.

2.5 Summary

In this chapter, the basic theory of a plasma wiggler with an ion channel (PWIC) has been introduced. The comparison between a plasma wiggler and

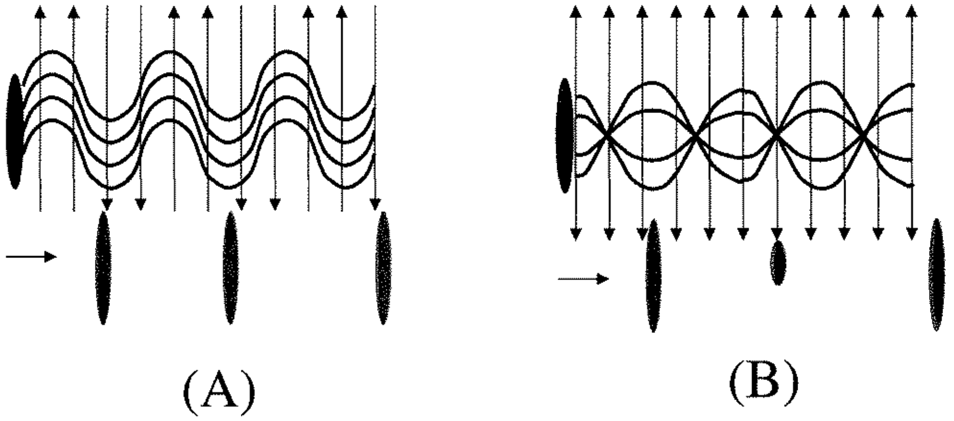

Figure 2.13: An illustration of the electron beam trajectories in (A) a plasma wiggler with a plasma wave (PWPW) and in (B) a plasma wiggler with an ion channel (PWIC).

Configurations	A plasma wiggler with a plasma wave	A plasma wiggler with an ion channel
Electrostatic Field $\vec{E}_\perp$	$\frac{4\pi e\delta n_p}{\omega_p/c} sin(\omega_p t)\hat{x}$	$2\pi n_p e\vec{r}$
Wiggler wavelength λ_w (cm)	$3 \times 10^6/\sqrt{n_p(cm^{-3})}$	$3 \times 10^6\sqrt{2\gamma/n_p(cm^{-3})}$
Wiggler Strength K	$\delta n_p/n_p$	$2\pi\gamma\sigma_r/\lambda_w$
Radiation wavelength λ_r (on axis)	$(1+K^2/2)\lambda_w/(2\gamma^2)$	$(1+K^2/2)\lambda_w/(2\gamma^2)$
Effective magnet strength $B_{eff}(gauss)$	$2\pi mc^2K/(e\lambda_w)$ $\leq 3 \times 10^{-3}\sqrt{n_p(cm^{-3})}$	$2\pi n_p e\sigma_r$ $\approx 3 \times 10^{-11}n_p(cm^{-3})$ with $\sigma_r \approx 100$ μm

Table 2.2: Comparison between a plasma wiggler with a plasma wave (PWPW) and with an ion channel (PWIC).

a magnetic wiggler has been made. The formation of the ion channel has been discussed and demonstrated with a 3-D PIC simulation. The trajectory of a relativistic electron traversing an ion channel has been derived. Based on that, the spontaneous emission due to the electron's betatron motion has been discussed. The radiation spectrum from an electron has been numerically calculated. The radiation from an REB traversing an ion channel is the sum of the radiations from each electron in the beam by assuming there is no phase relation among the radiation fields from each electron. Based on that, the essentials of a PWIC such as the radiation power, the radiation angular distribution, the flux and the spectral brightness have been derived as functions of beam and plasma parameters. An example of a PWIC is proposed to demonstrate radiation of hard X-rays with its peak brightness close to $4 \times 10^{20}\ photons/(sec \cdot mrad^2 \cdot mm^2 \cdot 0.1\% bandwidth)$.

CHAPTER 3

Plasma Source Development for Experiment

3.1 Introduction

We will discuss the construction and the characterization of a plasma source in this chapter. It has already been stated that the X-ray generation experiment was carried out parasitically to the plasma wakefield acceleration experiment. Therefore the requirement of the plasma source were the same for both of these experiments. We will therefore discuss the requirements on the plasma source placed by the acceleration experiment first.

The plasma wake-field accelerator (PWFA), a scheme for achieving ultrahigh longitudinal electric fields in a beam-excited electron plasma wave, has been investigated vigorously in recent years [29]. In a PWFA scheme, a relativistic electron beam(REB) expels plasma electrons away and leads behind an ion channel. The plasma electrons rush back and produce a longitudinal plasma wake field which can accelerate the tail of the beam. The linear response of a plasma to an REB with bi-Gaussian density distribution is given by [30]

$$E[V/cm] = \sqrt{2\pi n_p[cm^{-3}]} \times \frac{n_b}{n_p}\frac{\omega_p}{c}\sigma_z e^{\frac{-\omega_p^2\sigma_z^2/2c^2}{1 + c^2/(\omega_p^2\sigma_r^2)}} sin(\omega_p(z/c - t)), \qquad (3.1)$$

where n_p is the plasma density, n_b is the REB density, ω_p is the plasma frequency defined as $\omega_p = (4\pi n_p e^2/m_e)^{1/2}$, σ_r is the RMS radialbeam size and σ_z is the RMS beam length. Equation 3.1 predicts the maximum wake amplitude to occur for a plasma density such that $\omega_p \sigma_z / c \approx \sqrt{2}$ for a narrow bunch ($\omega_p \sigma_r / c << 1$) of fixed number of beam particles. A PWFA experiment, called E-157, was proposed to demonstrate electron acceleration in a meter long distance by using a 30 GeV REB provided by the Stanford Linear Acceleration Center (SLAC). A typical SLAC beam has the number of electrons $N_b = 1.8 \sim 2 \times 10^{10}$, the RMS length $\sigma_z 0.4 \sim 0.8\ mm$, and the RMS size $\sigma_r \sim 40\ \mu m$. The beam density n_b satisfies $n_b = N_b/((2\pi)^{3/2}\sigma_r^2\sigma_z)$. The goal of E-157 aimed to achieve 1 GeV electron gain by producing 1 GeV/m accelerating wake-field. The optimal plasma density to meet such a goal can be estimated based on the linear theory. Fig 3.1 demonstrates the peak acceleration field as a function of plasma densities with the SLAC beam parameters provided above, based on Eq. 3.1. The figure shows that the optimal plasma density increases as the beam length decreases, as expected from the linear theory. It also indicates that a meter long plasma source with plasma densities tunable in the range of $10^{13} \sim 10^{15}\ cm^{-3}$ is needed for E-157[1].

Such a meter long plasma source is not only useful for the PWFA scheme, it is also desirable in other plasma based applications. For example, in a plasma wiggler scheme [7] as discussed in Chapter 2, a long and uniform plasma source is preferred in order to increase the radiation efficiency and decrease the radiation bandwidth.

A 1.4 m long homogeneous plasma source with plasma densities tunable in the range of $10^{13} \sim 10^{15}\ cm^{-3}$ was developed at UCLA. The plasma source is essentially a 2 m long heat pipe oven containing a uniform lithium metal vapor with its density tunable from $2 \times 10^{15}\ cm^{-3}$ to $6 \times 10^{15}\ cm^{-3}$. The plasma is then created by ionization of the vapor with an ArF excimer laser (193 nm).

---

[1] It should be noted that the validity of linear theory requires $n_b << n_p$, which may not be true for the SLAC beam parameters and the optimized plasma densities. Nevertheless, it serves as a useful guide in deriving the optimized plasma densities. PIC (Particle-In-Cell) simulations verified the conclusion of the theory[30].

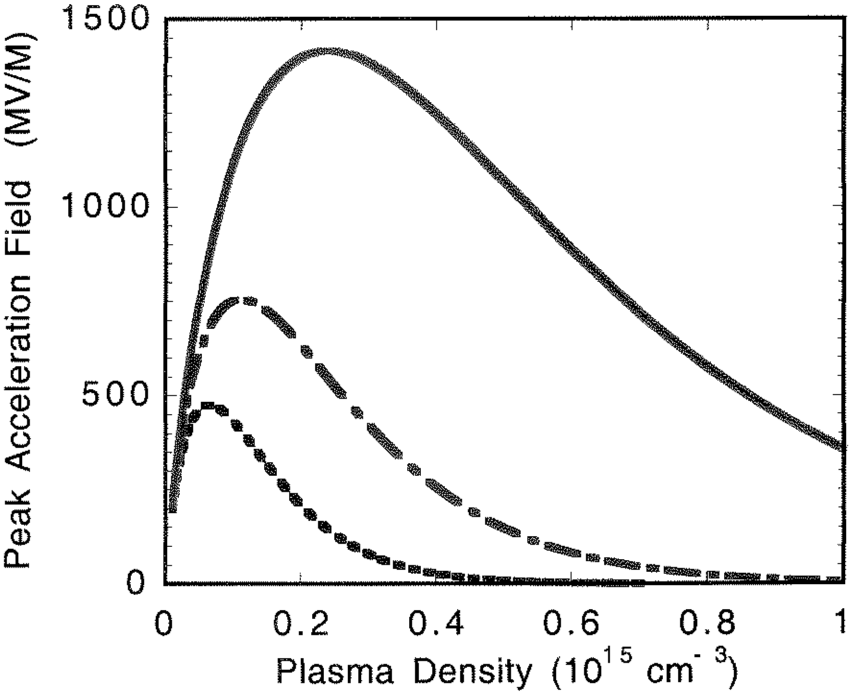

Figure 3.1: The peak acceleration field as a function of the plasma density based on Eq. 3.1. The beam charge numbers N_b is 1.8×10^{10}, and the beam size σ_r is 40 μm. The *solid* line corresponds to the beam length σ_z 0.4 *mm*; the *dot – dash – dot* line is to 0.6 *mm*; and the *dot* line is to 0.8 *mm*.

Atomic Number	3
Atomic Weight	6.94
Density (300 K gas)	0.534 g/cm^3
Thermal Conductivity	0.837 $W/(cm \cdot K)$
Heat Capacity (300 K gas)	3.582 $J/(g \cdot K)$
Melting Point	180.54 ^0C
Boiling Point (1 atm)	1342 ^0C
Lowest Ionization Potential	5.392 eV
Second Ionization Potential	75.638 eV

Table 3.1: Lithium Physical Parameters [34]

Lithium is chosen as the metal vapor source based on the following reasons. First of all, the lowest ionization potential of lithium is only 5.39 eV, while the second lowest is 75.6 eV. Therefore, with the commercial ArF laser whose photon energy $h\gamma = 6.4\ eV$, the lithium vapor can be photon-ionized with an one-photon process. Secondly, in a PWFA experiment like E-157, additional plasma created by the impact ionization should be small compared to that created by the photoionization. Lithium has a low atomic number ($Z = 3$), therefore the impact-ionization cross-section which is proportional to the atomic number Z, is small. Finally, lithium is very suitable for building the the metal vapor oven because of its high heat of vaporization and its hight surface tension [31]. The related lithium physical constants are listed in Table 3.1.

The construction of the 1.4 m long homogeneous plasma source and the diagnostics of vapor and plasma densities are fully described in the following sections. In Section 3.2 the background theory of the vapor and plasma density diagnostics is reviewed. Then in Section 3.3, the construction of a meter long lithium vapor heat-pipe oven is discussed, and the main characteristics of the oven are demonstrated. After that, vapor density measurements based on three different diagnostic techniques, the vapor temperature method, the hook method and the white light absorption method, are studied in Section 3.4. In Section 3.5 the plasma production and the corresponding diagnostic techniques, the CO_2 interferometry method and the UV light absorption method are discussed, and the diagnoses of plasma density distribution and the plasma decay time are presented. Finally a summary in given in Section 3.6.

3.2 Background Theory of Vapor and Plasma Density Diagnostics

There are two principal techniques for measuring vapor and plasma densities: the absorption method based on the measurement of the absorption coefficient, and the dispersion method where the refractive index is to be determined. The dielectric constant ϵ plays a key role in theories of all kinds of vapor and plasma density diagnostics. A general expression of the the dielectric constant ϵ for a vapor at a frequency ω associated with atomic transition from ground state i is [32]

$$\epsilon_i(\omega) = 1 + \frac{4\pi N_i e^2}{m_e}\left(\frac{M}{2\pi kT}\right)^{1/2} \int e^{-\frac{Mv^2}{2k_B T}} \sum \frac{f_{ji}(1 - \frac{g_i N_j}{h_j N_i})}{\omega_{ij}^2 - \omega^2(1 + \frac{v}{c})^2 + i\Delta\omega_{ij} \cdot \omega(1 + \frac{v}{c})} dv, \tag{3.2}$$

where $N_{i(j)}$ is the density at state i (or j), M is the mass of the atom species, T is the vapor temperature, v is the velocity of an gas electron, f_{ji} is the oscillator strength, which is a measure of the strength of the response on a real atomic transition relative to the response of a classical electron oscillator between state i and j [33], g_i, g_j are degeneracy numbers of energy states, ω_{ij} is line center frequency, and $\Delta\omega_{ij}$ is the linewidth, which represents phenomenally different kinds of line broadening mechanisms such as natural linewidth, self-broadening, pressure broadening, etc.

A lithium atom has one transition line in the visible frequency range from its ground state 2s to its excite state 2p at $\lambda_0 \approx 670.78$ nm with the oscillation strength $f = 0.74$[2]. In the vicinity of the line-center where the Lorentz broadening dominates the Doppler broadening [32], the dielectric constant in Eq. 3.2 can be simplified as

$$\epsilon(\omega) = 1 + \frac{4\pi N e^2 f}{m(\omega_0^2 - \omega^2 + i\Delta\omega_0\omega)} \tag{3.3}$$

where N is the population of the ground state 2s of lithium and is in fact the vapor density if the thermal temperature of lithium atoms is low $(k_B T < h\gamma_{ij})$.

The complex refractive index for a lithium vapor can be expressed as

$$\tilde{n}(\omega) = \sqrt{\mu\epsilon(\omega)} = \sqrt{1 + \frac{4\pi N e^2 f}{m(\omega_0^2 - \omega^2 + i\Delta\omega_0\omega)}} \approx 1 + \frac{2\pi N e^2 f}{m(\omega_0^2 - \omega^2 + i\Delta\omega_0\omega)} \tag{3.4}$$

Based on Eq. 3.4, The real part of the refractive index is

$$n(\omega) = Re(\tilde{n}(\omega)) = 1 + \frac{2\pi N e^2 f(\omega_0^2 - \omega^2)}{m((\omega_0^2 - \omega^2)^2 + \Delta\omega_0^2\omega^2)}, \tag{3.5}$$

and the absorption coefficient α, which is a function of the imaginary part of the refractive index, is

$$\alpha(\omega) = \frac{2\omega}{c} Im(\tilde{n}(\omega)) = \frac{4\pi\omega}{c} \frac{N e^2 f \Delta\omega_0 c\omega}{m((\omega_0^2 - \omega^2)^2 + \Delta\omega_0^2\omega^2)}. \tag{3.6}$$

Provided that the frequency is not so close to the linecenter, i.e., $|\omega^2 - \omega_0^2| >> \Delta\omega_0\omega$, the real refractive index can be further simplified as

$$n(\lambda) \approx 1 + \frac{N r_0 f \lambda_0^3}{4\pi(\lambda - \lambda_0)}, \tag{3.7}$$

---

[2] In fact, a lithium atom has two strong transition lines in the visible region which are at $\lambda_{01} = 670.791$ nm $(2s^{1/2} \rightarrow 2p^{1/2})$ with oscillator strength 0.248 and at $\lambda_{02} = 670.776$ nm $(2s^{1/2} \rightarrow 2p^{3/2})$ with oscillator strength 0.496 respectively[34]. However, these two line centers cannot be resolved with a conventional spectrometer.

with $r_0 = e^2/mc^2 = 2.8 \times 10^{-15}m$ the classical electron radius. Under the same condition, the absorption coefficient can be simplified as

$$\alpha \approx \frac{0.5Nr_0 f\Delta\nu_0}{(\nu - \nu_0)^2}, \tag{3.8}$$

where $\nu = 1/\lambda$ is the spectral frequency. Eq. 3.7, which is also called Sellmeier formula [35], is often applied to the dispersion method such as hook method, while Eq. 3.8 is often applied to the absorption method. It can be seen that the absorption coefficient in Eq. 3.8 is the function of the linewidth $\Delta\nu_0$, whereas the refractive index in Eq. 3.7 is not. Since the linewidth $\Delta\nu_0$ usually entangles with different kinds of line-broadening mechanisms and cannot be calculated accurately, the dispersion method normally provides more accurate measurements than the absorption method does.

As the vapor medium is partially ionized to form a plasma, the dielectric constant is modified to

$$\epsilon = 1 + \frac{4\pi Ne^2 f}{m(\omega_0^2 - \omega^2 + i\Delta\omega_0\omega)} - \frac{\omega_p^2}{\omega_0^2} \tag{3.9}$$

where $\omega_p = 4\pi n_p e^2/m$ is the plasma density. If the spectra is far away from the absorption center, the real refractive index can be deduced and approximated as

$$n(\lambda) \approx 1 + \frac{Nr_0 f\lambda_0^3}{4\pi(\lambda - \lambda_0)} - \frac{n_p}{2n_c}, \tag{3.10}$$

where n_p is the plasma density, and n_c is the critical plasma density for the wavelength λ, which satisfies $n_c = \pi mc^2/(\lambda^2 e^2)$.

If the spectra is further away from the center, the real refractive index can be simplified as

$$n(\lambda) \approx 1 - \frac{n_p}{2n_c} \tag{3.11}$$

Equation 3.11 is applied for the plasma density mesurement with the CO_2 laser interferometry method, which will be studied in Section 3.5.

3.3 The Construction of the Lithium Vapor Heat-Pipe-Oven

The theory of the construction of a metal vapor heat pipe oven was originally developed by Grover, *et al.,* [36], and since then metal vapor heat pipe ovens have been extensively used to generate well-defined homogeneous metal vapors. The homogeneity is due to the high heat conductivity, and, therefore, high heat transport capability of the metal vapor. In such a heat-pipe-oven, a metal vapor is confined by an inert gas to separate the vapor from the windows, and the parameters of the vapor, such as temperature, pressure, and optical length, etc., can be well controlled [31].

A 25 *cm* long and a 1.4 *m* long lithium heat-pipe-oven were built at UCLA in sequence. The purpose to build a shorter oven was to gain experience with the construction of an oven and the experience with the formation of plasma, and to test the different diagnostic techniques. The schematics and the characteristics of both ovens are almost the same. The details of the 25 *cm* long oven was published elsewhere [37]. The construction of the 1.4 *m* long oven and its main characteristics are presented in the following.

The schematic of a 1.4 m long heat pipe oven built for this experiment is shown in Fig. 3.2. The stainless steel tube, part of which forms the oven, is 2 *m* long (from valve to valve), with an inner diameter of 38 *mm*. A capillary structure called wick, which is made of 4 layers of stainless-steel mesh was set inside the tube. Four thermocouples were set at the inside surface of the wick, and they were purposely located at the one side of the oven, since the heat pipe was completely symmetric with respect to the center of the heater section. The tube was wrapped with a heat tape, and then covered with with a layer of 3 *mm* thick aluminum screen, and with insulation bricks. All of these covers were used to decrease the heat loss due to the radiation loss and the convection loss as the oven works at high temperatures.

The cold oven was first filled with helium at 400 $mTorr$, with 120 g lithium laying inside the center of the oven. When the oven was heated, the metal melted down and wet the wick. As the temperature inside the oven went higher, the metal then evaporated with the vapor pressure satisfying the vapor pressure curve (refer to Appendix B). Initially the vapor pressure exceeded the buffer pressure and this caused the vapor to diffuse towards both ends until it condensed again. The condensate returned through the wick back to the heated portion of the oven by the capillary action. Owing to the pumping action of the flowing vapor, it is expected that the inert gas was completely separated from the vapor and provided sharp (a few centimeters) boundaries at the two sides of the lithium vapor column. Finally an equilibrium was reached, in which the vapor was in equilibrium with the liquid phase close to the surface of the wick, and the center part of the oven was filled with the metal vapor at a pressure approximately equal to the buffer gas pressure[3], as illustrated in Fig. 3.2. Temperatures measured by the thermocouples at the equilibrium present vapor temperatures. Therefore the vapor density can be estimated with the vapor temperature by means of the lithium vapor pressure curve (refer to Appendix B), which will be detailed in the next setion.

One of the most important characteristics of a metal vapor heat-pipe-oven is that the metal vapor density and the metal vapor length can be adjusted separately. As the oven reaches the equilibrium, the vapor density is determined

---

[3] This vapor pressure is ideally equal to the buffer pressure if the Li flow velocity along the oven is zero [38]. In reality, the vapor pressure would be slightly larger than the buffer pressure due to the subsonic vapor flow along the oven.

by the buffer pressure, while the vapor length is by the heating power. The independent control of the vapor density and the vapor length is one of the most attractive features of the heat pipe oven. We demonstrate this property with Fig. 3.3 (a) and (b). As shown in Fig. 3.3(a), the vapor temperature at the center of the oven increased from about 690 ^0C to about 700 ^0C as we increased the buffer pressure from 304 $mTorr$ to 401 $mTorr$ but kept the heat power constant. As shown in Fig. 3.3(b), the length of the metal vapor with a homogeneous temperature extended from about 65 cm to 70 cm (only the right side of the oven temperature distribution is plotted) as we increased the heat power from 768 W to 781 W but kept the same buffer pressure.

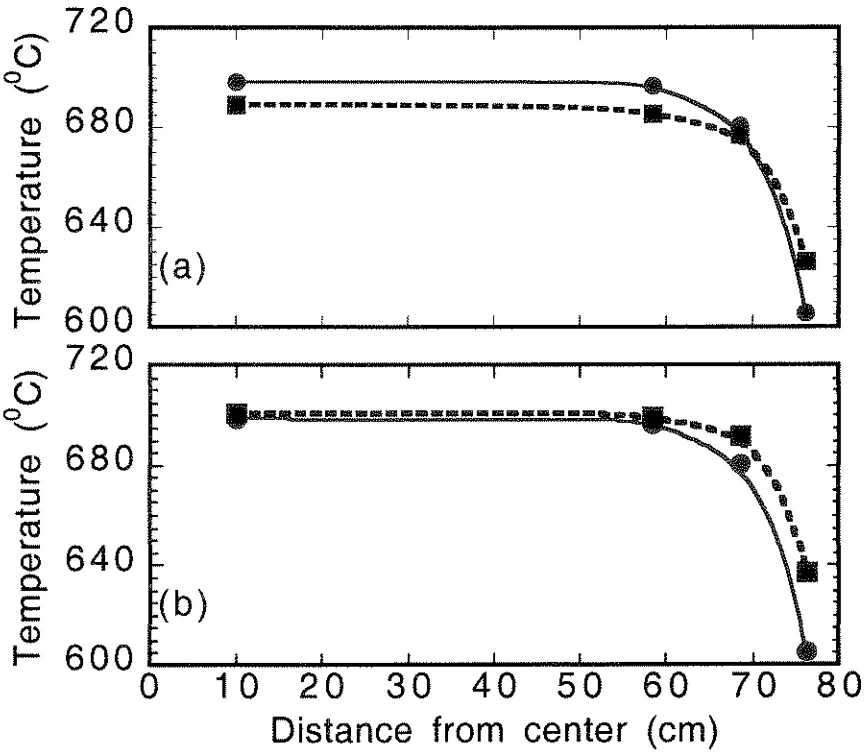

Figure 3.3: Temperature distribution along the oven (a) at the fixed heat power 768 W but different buffer pressure, 304 $mTorr$ (squares) and 401 $mTorr$(dots); (b)at the fixed buffer pressure (401 $mTorr$) but different heat power, 768 W (dots) and 781 W. (squares).

In conclusion, we have built a homogeneous lithium-vapor heat pipe oven. The vapor density and length can be adjusted separately by controlling the heat power and the buffer pressure. In the following section, the vapor density measurements at different oven conditions are presented.

3.4 Vapor Density Measurement

Vapor density inside the oven was determined by three different methods. First, lithium neutral vapor densities are deduced based on the vapor temperature measurements by thermocouples. The accuracy of this method depends on accuracy of the empirical vapor pressure curve (refer to Appendix B). However, due to possible degradation of thermocouples in the process of operation, it is important to develop independent optical methods to detect vapor densities. An interferometric dispersion method called the hook method [39] is used to diagnose the line-integrated vapor densities along the oven. The results of these two measurements are compared. A white light absorption method is also used to measure vapor densities in the oven. As stated in Sec. 3.2, measurements based on an absorption method are normally less accurate than those based on a dispersion method. However, an absorption method is normally much easier to use in the experiment than a dispersion method. This is important since it is impossible to set up a dispersion based diagnostic, like the hook method, in the harsh environment of the E-157 experiment. Calibration of the measurements from white light absorption method with those from the hook method is also discussed.

3.4.1 Vapor Density Measurement with Vapor Temperature Profiles

As addressed in Sec. 3.3, vapor temperatures were measured by thermocouples in the oven as the oven reached an equilibrium. Based on the vapor temperature T, the vapor pressure P can be estimated using the empirical vapor-pressure curve (refer to Appendix B). The vapor density can then be calculated with the thermal equilibrium equation, $n_0 = P/(k_B T)$. Once the lithium vapor density and its distribution is known, the vapor length over which the vapor density dropping 50% of the center density can be estimated.

Figure 3.4 demonstrates the calculated vapor density distribution along the oven under several different buffer pressures. The buffer pressure was adjusted to reach different vapor densities, while the heat power was adjusted for the designed vapor length 1.4 *m*.

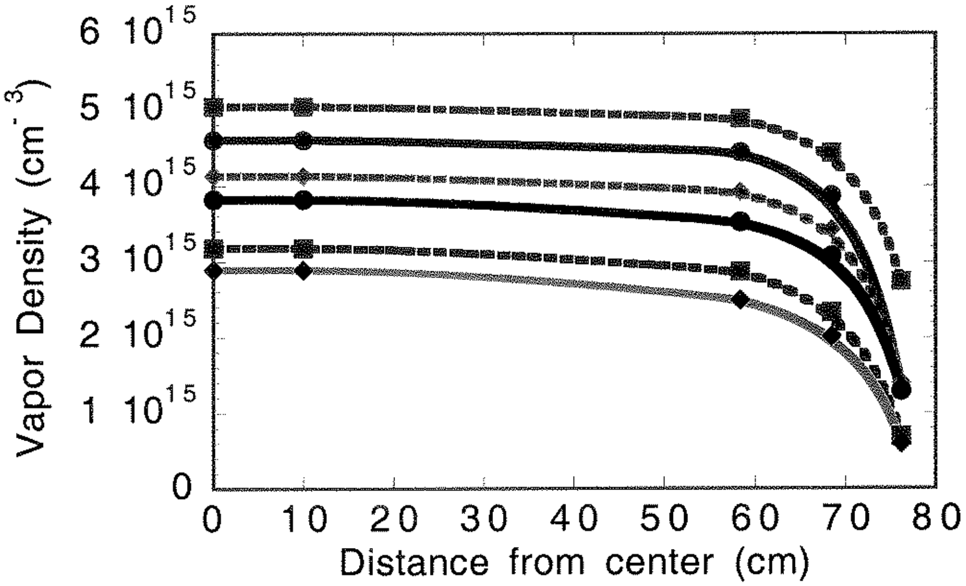

Figure 3.4: Vapor density distribution along the oven under different buffer pressures. Only half of the oven is shown. From upside down, the buffer pressure was 443 *mTorr*, 400 *mTorr*, 351 *mTorr*, 300 *mTorr*, 250 *mTorr*, and 204 *mTorr* respectively.

Pressure ($mTorr$)	Heater Current (Amp)	T1 (^0C)	T2 (^0C)	T3 (^0C)	T4 (^0C)	Vapor Density ($10^{15}cm^{-3}$)	Optical Length ($10^{17}cm^{-2}$)
443.	7.10	673.97	699.30	704.70	706.40	5.04	7.04
400.	7.04	637.00	692.00	699.50	701.40	4.60	6.47
351.	6.97	640.40	685.50	692.70	695.50	4.13	5.65
300.	6.98	636.80	679.80	687.10	691.30	3.82	5.22
250.	6.80	607.90	665.60	676.30	681.60	3.18	4.20
204.	6.80	601.80	658.30	669.10	676.60	2.88	4.04

Table 3.2: Working condition for different vapor density requirement.

Table 3.2 summarizes the oven conditions, under which data in Fig. 3.4 were produced. These conditions include the buffer pressure, the heater current, the thermocouple temperature, the calculated vapor density, and the calculated line integrated vapor density (optical length) nL. The optical lengths were estimated by numerically integrating the vapor densities along the lines shown in Fig. 3.4. They were used later for comparison with other measurements.

It should be noted that the heater current in Table 3.2 only provides a reference. In the E-157 experiment [20], a stainless steel cover was installed additionally on the outside of the oven bricks. This made the oven heater more efficient and so less heater power was needed to produce the same vapor density distributions.

3.4.2 Line-integrated Vapor Density Measurement with Hook Method

The hook method is an interferometric method. It has been extensively used in measuring atomic oscillator strengths or gas densities since the early last century [35] [40]. The essence of hook method is that the refractive index demonstrates abnormal dispersion in the vicinity of the absorption center of the media to be exploited, as shown in Eq. 3.7.

The experimental setup for the hook method in measuring the Li vapor density is shown in Fig. 3.5. A Xenon Arc lamp used as a white light source has a uniform

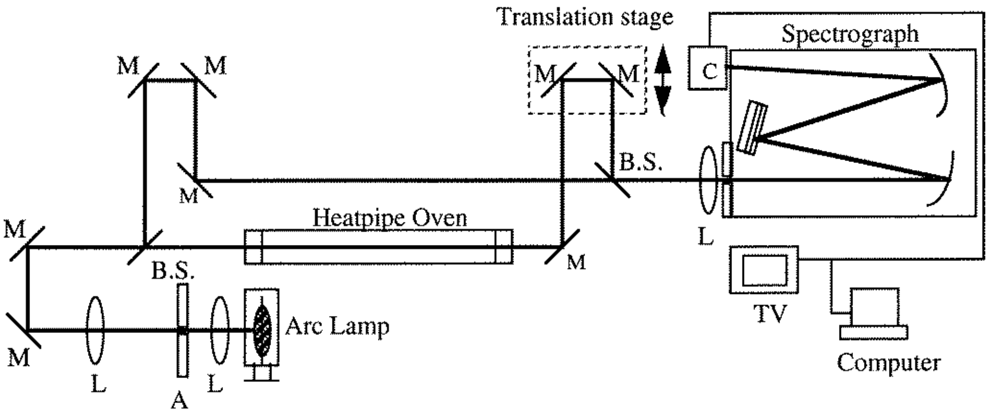

Figure 3.5: Experimental setup for hook method. Key: A-aperture; M: mirror; B.S.: beamsplitter; C: Camera; L:lens.

irradiance which covers several hundred nanometers in the visible region, and its spatial coherent length is tens of microns. The heatpipe oven was placed in one arm of the Mach-Zehnder interferometer. The interferometer light was sent to a stigmatic, f/4, 27-cm spectrograph (grating 1200g/mm) to observe the interference pattern in the vicinity of the neutral Li line at 670.78 *nm*. A typical hook interference image acquired by the CCD camera, which was set at the image plane of the spectrograph, is shown as Fig. 3.6. According to the hook method [40], the wavelengths representing hook positions are determined by

$$p = L\frac{dn(\lambda)}{d\lambda}, \tag{3.12}$$

where p is the order of fringes on which the hooks positions are measured, L is the length over which the white light goes through the lithium vapor, and $n(\lambda)$ is the real refractive index as addressed in Eq. 3.7. With Eq. 3.7 and 3.12, the line-integrated vapor density n_0L can be derived as

$$n_0L = \frac{p\pi\Delta^2}{r_0 f\lambda_0^3}, \tag{3.13}$$

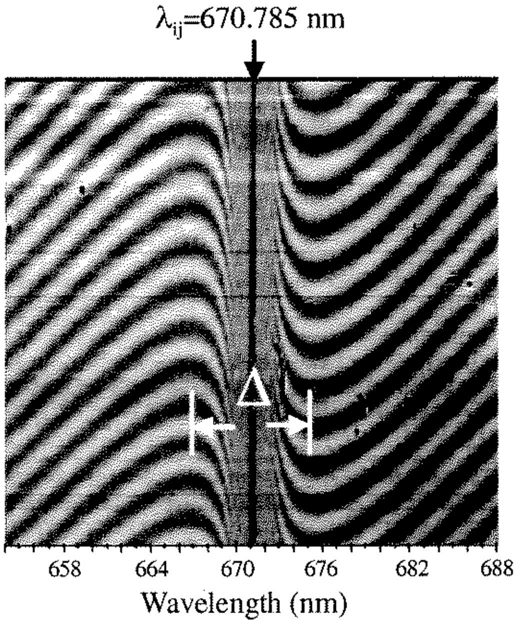

Figure 3.6: A typical hook image recorded in the plane of the imaging spectrograph. The image was taken as the oven center temperature was around 500^0C. A number of interference fringes form hooks at both sides of the absorption center $\lambda_0 = 670.78\ nm$. Two thin vertical lines mark hook positions and Δ represents the wavelength difference between hooks.

with Δ the wavelength difference between hooks, $r_0 = 2.8 \times 10^{-13}\ cm$ the classical electron radius, and $f = 0.75$ the Li oscillator strength at $\lambda_0 = 670.78\ nm$. Note that the the line-integrated vapor density $n_0 L$ measured with the hook method does not depend on the linewidth.

Figure 3.7 demonstrates optical lengths measured with the hook method and with the vapor temperature method discussed in Sec. 3.4.1 as a function of buffer pressures. The oven conditions for this figure have been summarized in Tab 3.2. The agreement between the above two methods is very good.

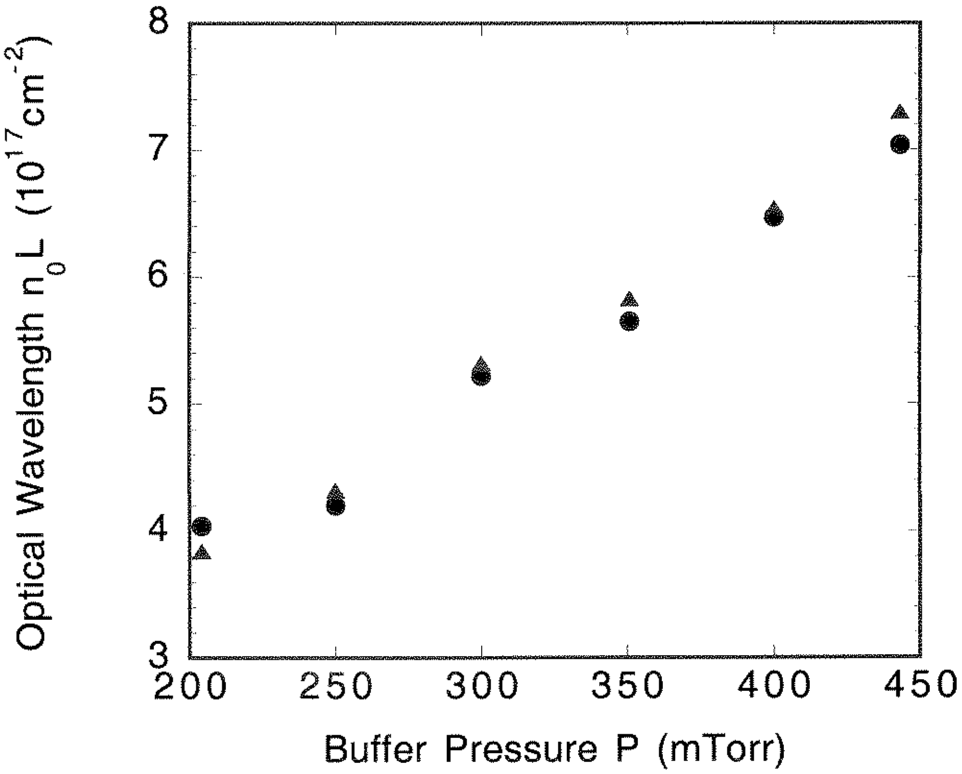

Figure 3.7: Measured optical lengths as a function of buffer pressures. The *dots* in the figure are the optical lengths measured with the hook method, and the *triangles* are optical lengths deduced with the thermocouple temperature measurements.

3.4.3 Vapor Density Measurement with White Light Absorption Method

The essence of the white light absorption method is that the absorption coefficient α strongly increases around the frequency corresponding to a resonant transition of the atoms of the vapor, as addressed in Eq. 3.8.

As discussed in section 3.2, measurements from an absorption method are normally less accurate than those from a dispersion method because of the dependence of the absorption coefficient α on the linewidth $\Delta\nu_0$. There are several mechanisms can contribute to the linewidth, which include the natural linebroadening, the self-broadening (collisional), the foreign or buffer gas pressure broadening (collisional) and the Doppler broadening. Fortunately, based on conditions of our oven (see Tab. 3.2), the self-broadening dominates the natural linebroadening and the foreign-gas pressure broadening [41]. Doppler broadening can be ignored if the measurement is only applied to the Lorentzian wings of the absorption curve [32]. The theory predicts that the self-broadening linewidth $\Delta\nu_{SB}$ is proportional to the vapor density n_0, which is

$$\Delta\nu_{SB} = K \cdot \frac{r_0 \cdot f \cdot n_0}{\nu_0} \tag{3.14}$$

where ν_0 is the spectral frequency of the lithium line center, r_0 is the classical radius of an electron, f is the lithium oscillator strength at its linecenter, and K is the constant of proportionality. The published values of K vary by a factor of two, For instance, $K = 1, 0.585, 1.047, 1.333$ respectively from references [42] -[45]. So far we haven't found any reference giving a conclusion on the difference of K. This may be due to the reason that K may not be an independent constant. In order to find the value K for the white light absorption method to be applicable under our oven conditions, we calibrated K by comparing vapor densities measured with the white light absorption method and with the hook method.

The schematic for the white light absorption method is shown in Fig. 3.8. The Arc lamp and the spectrograph are the same as those used in the hook measurement. A pencil of white light was sent through the Li heat pipe oven, and then spectrally analyzed with a spectrograph. Figure 3.9 demonstrates a typical transmission curve around the Li absorption center as the oven center temperature was around 700^0C.

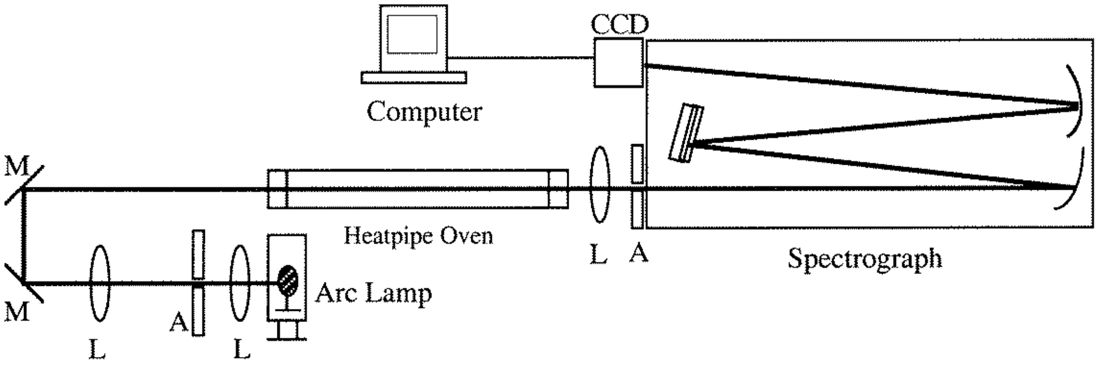

Figure 3.8: Experimental setup for the white light absorption method. Keys: A: aperture; L:lens; M:mirror.

In theory, the transmission T of the white light propagating through the oven satisfies

$$T = e^{-\alpha \cdot L} = e^{-\frac{K \cdot r_0^2 \cdot f^2 \cdot n_0^2 L}{2\nu_0(\nu-\nu_0)^2}}, \tag{3.15}$$

in views of Eq. 3.8 and 3.14, with L the lithium vapor length assuming to be 1.4 m. All the other variables in Eq.3.15 have been addressed in equations of 3.8 and 3.14.

By curve-fitting the transmission curve at the wings of the absorption center with Eq. 3.15, the vapor density n_o can be deduced. A least-square-fit curve with Eq. 3.15 is also plotted in Fig. 3.9.

The vapor densities measured from the both the hook method and the white light absorption method as a function of the oven center temperatures are shown

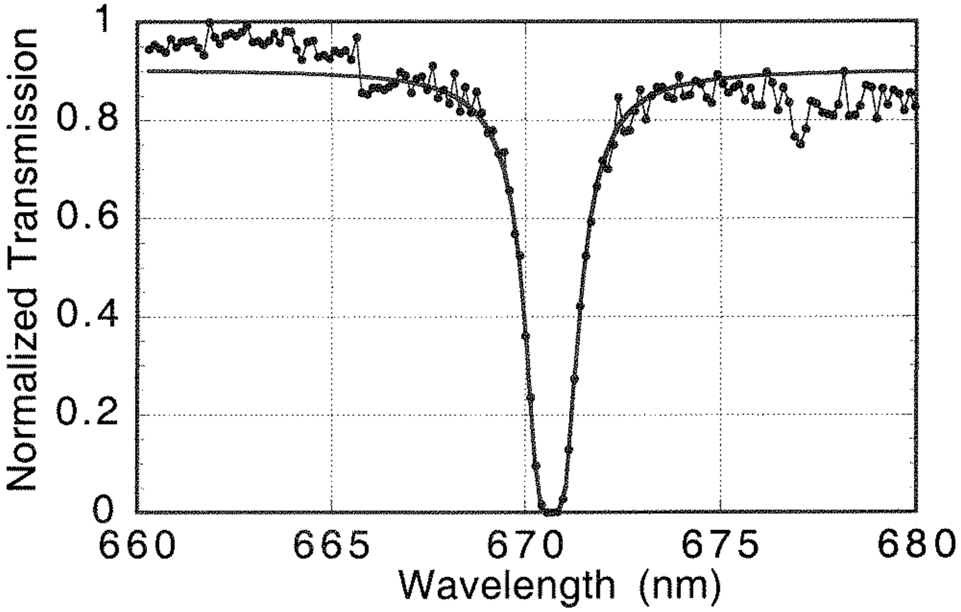

Figure 3.9: Measured white light transmission (dots) in the vicinity of the lithium line center $\lambda_0 = 670.78$ nm. The least-Square-Fit curve is plotted based on Eq. 3.15. The measurement was taken as the oven center temperature was around 700^0C.

in Fig. 3.10. Different empirical values of K were used to derive the vapor densities in the white light absorption method. The vapor densities measured with the hook method were deduced by assuming the lithium vapor length 1.4 m. The error bars of white light absorption measurements were from errors of of the curve-fit processes, while those of hook measurements were due to systematic errors. We conclude from the figure that the white light absorption measurements agree with the hook measurements quite well if the empirical $K = 1.333$ is used to characterize the white light absorption method.

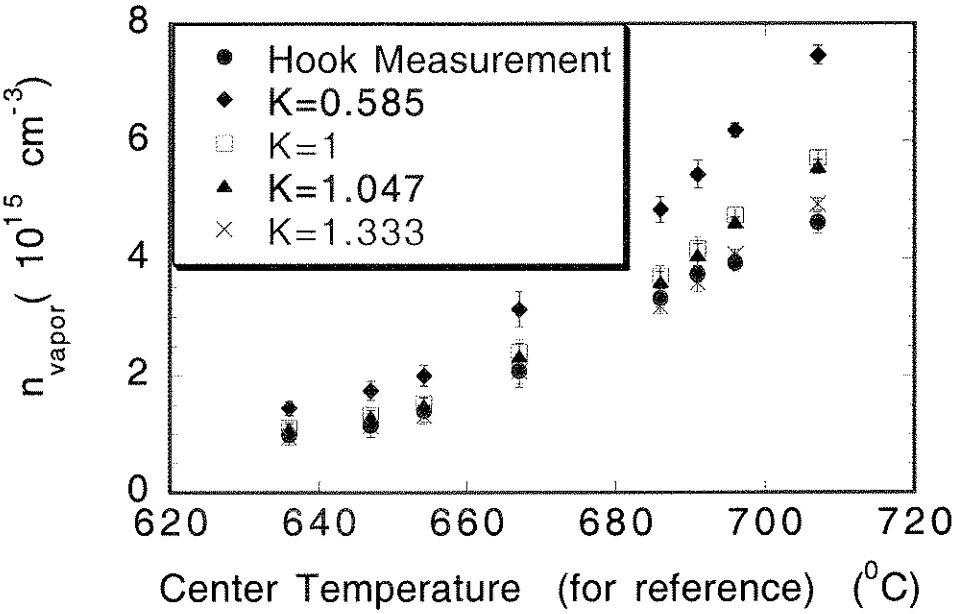

Figure 3.10: Lithium vapor density measurements from the hook method, and the white light absorption method under different values of K as a function of the oven center temperatures. K is the constant of proportionality addressed in Eq. 3.14.

3.5 Plasma Production and Diagnostics

The plasma is produced as a pulsed UV laser beam (193 nm, 6.4 eV) traverses the lithium vapor column and photoionizes the lithium atoms (the ionization potential of lithium 5.39 eV). Then the plasma decays locally due to recombination and diffusion processes. This relative slow plasma decay process (on microseconds scale) enables us to resolve plasma density evolution by interferometric diagnostics.

In this section, first the plasma production and the measurements of plasma density distribution along the 1.4 m oven are discussed. After that, the measurement of the plasma decay time with CO_2 laser interferometry in the 25 cm long plasma source is studied. Since the plasma parameters such as the plasma density, the plasma temperature, etc. are very close for both 25 cm and 1.4 m lithium plasma sources, the measured plasma decay time in the short oven provides a good reference for the estimation of the plasma decay time in the long oven.

3.5.1 Plasma Production and Plasma Density Distribution Measurement by a UV laser

As a 193 nm UV laser beam traverses the lithium vapor column, the laser energy $E(z)$ attenuates according to

$$E(z) = E_0 \cdot e^{-\int_0^z n_0(z)\sigma dz}, \tag{3.16}$$

where E_0 is the laser energy at the entrance of the vapor column, σ is the photoionization cross-section of the Li atom, which is about 1.8×10^{-18} cm^{-2}[46], $n_0(z)$ is the vapor density distribution. Here we assume that UV laser energy attenuation is solely contributed to the photoionization of the lithium vapor, and that one UV photon creates one free electron from one Li atom. Therefore, plasma production satisfies that

$$dE(z) = -h\gamma \cdot n_p(z) \cdot S(z) \cdot dz, \tag{3.17}$$

where $h\gamma = 6.4\ eV$ is the UV photon energy, $S(z)$ is the laser beam size, and $n_p(z)$ is the plasma density distribution. Combining Eq. 3.16 and Eq. 3.17, we have

$$n_p(z) = \frac{n_0(z) \cdot \sigma \cdot E(z)}{h\gamma \cdot S(z)} = \frac{n_0(z) \cdot \sigma \cdot E_0 \cdot e^{-\int_0^z n_0(z)\sigma dz}}{h\gamma \cdot S(z)} \tag{3.18}$$

It can be seen from Eq. 3.18 that the plasma density n_p is proportional to laser energy $E(z)$, while the uniformity of plasma depends on the uniformity of the laser fluence $E(z)/S(z)$. In other words, the beam has to be focused in order to compensate the attenuation of the laser energy $E(z)$ along the lithium vapor oven.

The schematic for the plasma production and the plasma density diagnostic is illustrated in Fig. 3.11. A UV telescope (fused silica lenses with $f1 : f2 = -3 : 1$) was set in front of the laser to adjust the beam sizes $S(z)$ along the oven. A couple of UV mirrors were used to guide the laser beam through the oven. The UV laser intensity profiles were measured by analyzing the fluorescence images produced by the 193 nm radiation on a BK7 substrate. Two UV energy meters were used to measure the UV energy at the entrance and the exit of the oven. Slices (a)-(c) shown in Fig. 3.11 are typical UV fluorescence images measured at the exit, the middle and the entrance of the oven, respectively. The visible black lines in the slices are due to the nonuniform gain inside the laser cavity.

Figures 3.12(a) and (b) demonstrate the measured results of the vapor density distribution $n_0(z)$, the beam sizes $S(z)$ and the plasma density distribution $n_p(z)$ for a particular experimental run. The vapor density distribution $n_0(z)$ along the oven, as shown in Fig. 3.12(a), was measured as the vapor pressure was set

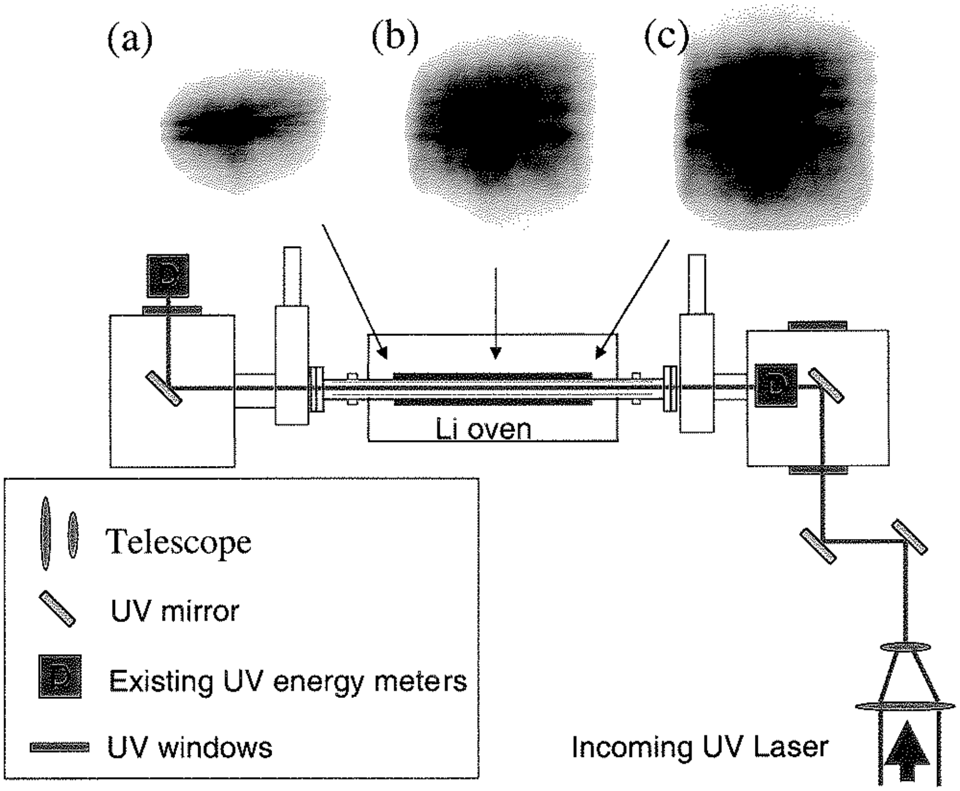

Figure 3.11: The experimental arrangement for a UV ionized Li plasma source. Three slices (a), (b) and (c) are UV fluorescence profiles measured at the exit, at the middle and at the entrance of the oven, respectively.

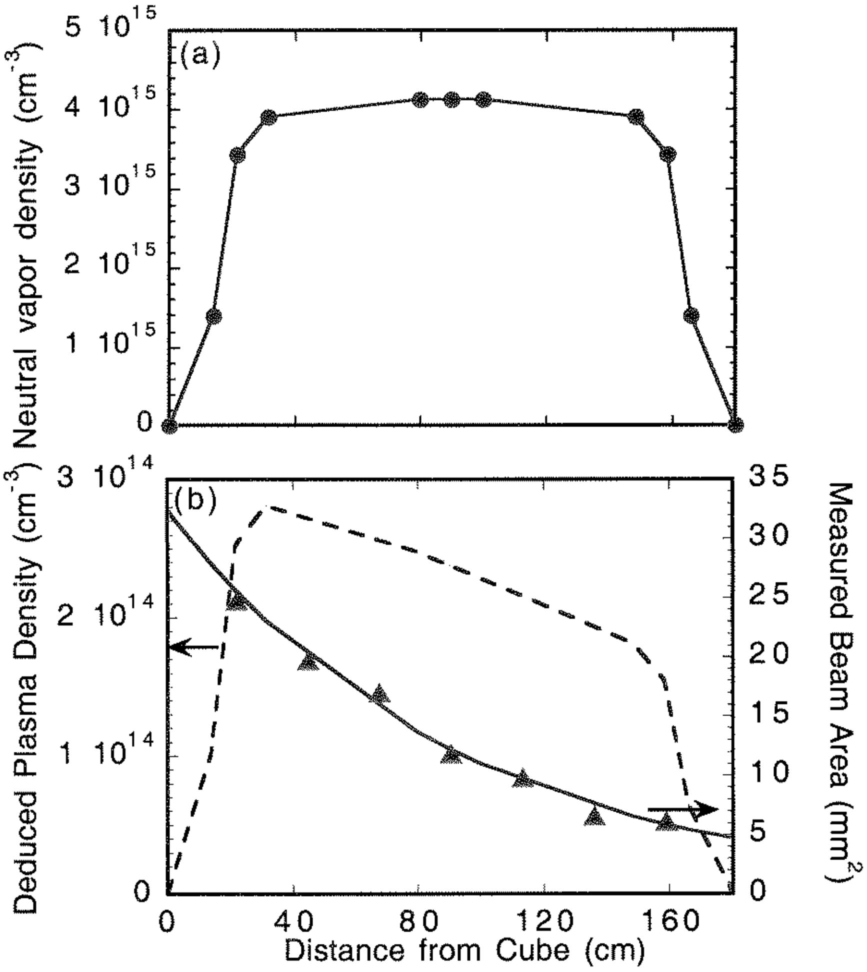

Figure 3.12: (a)Li vapor density distribution along the oven with the vapor pressure set at 351 $mTorr$.(b)Measured laser beam areas (triangles) and the deduced plasma density distribution (dash line) along the oven.

at 351 $mTorr$. The 1.4 m long column of $4 \times 10^{15}\ cm^{-3}$ vapor densities was produced. The beam sizes $S(z)$, as shown with triangles in Fig. 3.12(b), were measured by estimating the averaged area of the fluorescence images. The solid line in the figure is the curve-fit to those data. Since we expect the beam size changes smoothly with the distance along the oven, the curve-fit curve gives a better description of the real beam sizes. For this run, the UV energy at the entrance of the oven was measured to be 12 mJ. The plasma density distribution $n_p(z)$ was deduced based on Eq. 3.18, and the result is shown as the dash line in Fig3.12(b). Plasma density varied roughly from $2.8 \times 10^{14}\ cm^{-3}$ to $1.8 \times 10^{14}\ cm^{-3}$ along the 1.4 m distance of the oven for this run. Since the focusing scheme did not provide the idealized compensation of absorption loss, the variation of plasma density $\Delta n_p/n_p$ was about 50% along the oven. This would affect the maximum energy gain in the E-157 experiment.

3.5.2 Plasma Decay Time Measured with the CO_2 Laser Interferometry

A CO_2 laser interferometry was used to measure the plasma decay in the 25 cm Li plasma source. Since the probing wavelength (10.6 μm) is far away from the lithium linecenter (0.678 μm), the refractive index in the plasma source is mainly contributed from the plasma, while the the effect from the lithium neutrals can be ignored. In the schematic of the CO_2 laser (10.6 μm) interferometry, the plasma source is placed in one arm of a Mach-Zehnder interferometer. The phase shift of the interferometry signal is proportional to the difference of the refractive indexes in both arms. In our case, the phase shift $\Delta\Phi$ can be derived as

$$\Delta\Phi = 2\pi(n-1)L/\lambda_{CO_2}, \tag{3.19}$$

where n is the real part of the refractive index, and L is the length of the plasma source. The refractive index satisfies $n(\lambda) \approx 1 - n_p/(2n_c)$, as addressed in Eq. 3.11, where $n_c \approx 1.0 \times 10^{19}\ cm^{-3}$ is the critical plasma density for 10.6 μm. In view of Eq. 3.11 and Eq. 3.19, the plasma density is deduced as

$$n_p \approx -n_c \frac{\Delta\Phi}{\pi} \frac{\lambda_{CO_2}}{L}. \tag{3.20}$$

In the experiment, a hybrid scheme which includes a TEA CO_2 laser (Lumonics 101) and a LPL (low pressure laser, LP15) was employed to produce a single longitudinal mode output. Typical $10.6\mu m$ laser pulse was 200 ns FWHM with a $80\mu s$ tail. The 25 cm vapor column was placed in one arm of a Mach-Zehnder interferometer. The CO_2 laser was synchronized with a 20-ns UV laser pulse used to photoionize the lithium vapor column to create plasma. A HgCdZnTe detector (PEM L-5) with the rise time of $\sim 1ns$ was used to measure the interferometry signal. As there was no plasma in the oven, the interferometer was precisely adjusted so that the smallest interferometry signal was reached. The corresponding phase difference between two arms should be the odd multiples of π according to the basic interferometry principle. The measured smallest CO_2 interferometry signal $I_s(t)$ as a function of time is demonstrated as the curve (a) in Fig. 3.13. Additional π phase difference by extending the length of one arm by $\lambda_{CO_2}/2$ led to the largest interferometry signal $I_L(t)$, shown as the curve (b) in Fig. 3.13. This type of scanning calibration from minimum to maximum of interferometric pattern was necessary because of small detector size. Once the UV laser was fired, the plasma was created promptly (in a few nanoseconds) and it induced an additional phase shift $\Delta\Phi$. Then the plasma decayed locally due to recombination and possible diffusion, leading to decrease of the phase shift. Eventually the plasma disappeared, and hence the phase shift. The evolution of the interferometry signal $I_P(t)$ just after the plasma was produced is demonstrated as the curve (c) in Fig. 3.13.

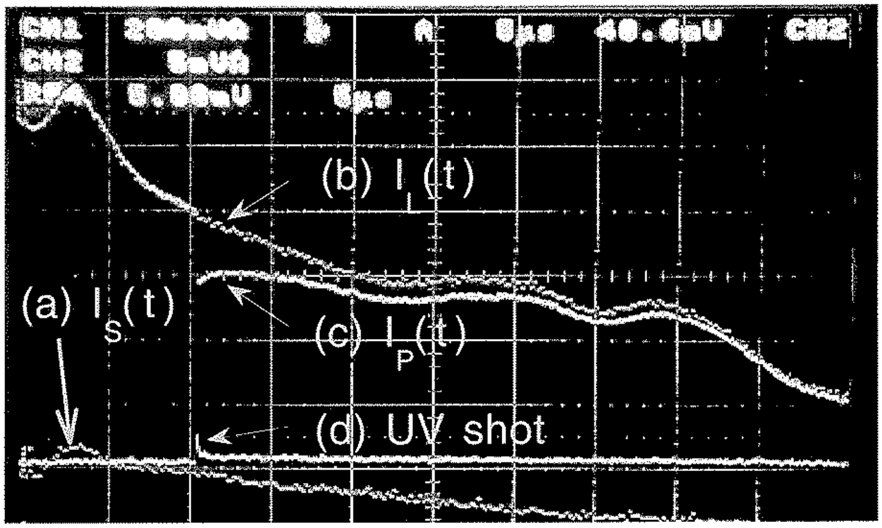

Figure 3.13: The output of an oscilloscope recording the CO_2 laser interferometry signal measured by the fast HgCdZnTe detector and the UV laser signal as the function of time. At this moment, the oven temperature was $T_{ext} \approx 720\ ^0C$. Curves (a), (b), (c), and (d) show the smallest interferometry signal $I_S(t)$, the largest interferometry signal $I_L(t)$, the interferometry signal $I_P(t)$ just after the plasma was produced, and the UV shot, as a function of time, respectively.

The phase shift was deduced based on the signal difference before and after the UV laser shot, which satisfies $\Delta\Phi(t) = cos^{-1}(1 - 2 \cdot \Delta_1(t)/\Delta_2(t))$, with $\Delta_1(t) = I_L(t) - I_P(t)$ and $\Delta_2(t) = I_L(t) - I_S(t)$. By measuring the phase shift at different time slices, the plasma density and its decay can be traced. Figure 3.14 demonstrates the deduced dynamics of plasma densities as a function of time, based on Fig. 3.13. The plasma density dropped from $2 \times 10^{14}\ cm^{-3}$ to half of this value in about 3 μS, and dropped by a factor of three in about 10 μS. The measured plasma decay time may be shorter than it should be since we assumed that the plasma length did not change during the plasma decay process. The relatively slow time scale allows for the tuning of plasma density in the E-157 experiment, on a shot-to-shot basis by varying the delay between the firing time

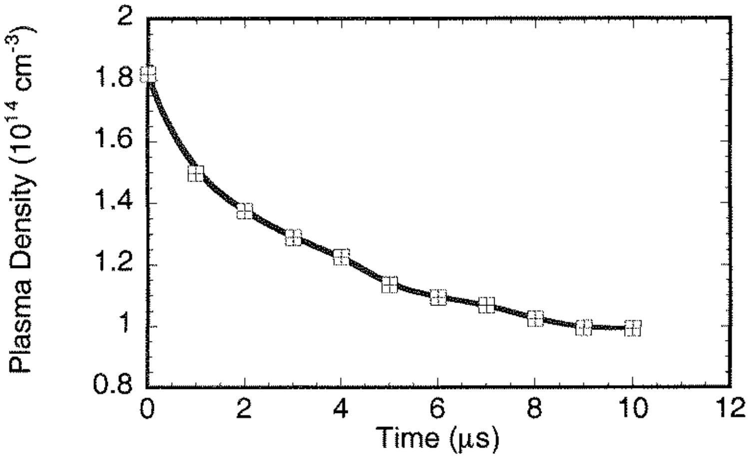

Figure 3.14: Plasma density as the function of time measured with CO_2 interferometry. The solid line is drawn for a guidance.

of the UV laser pulse and the electron beam pulse.

3.6 Summary

In summary, a 1.4 *meter* long plasma source for PWFA experiment is developed and fully characterized. This source contains a 1.4 m homogeneous lithium vapor column with the vapor density that can be tuned in the range of $(2.9 \sim 5.0) \times 10^{15}$ cm^{-3}. Various techniques, such as vapor temperature diagnostics, the hook method, and the the white light absorption method are used to measure the vapor density. The physical construction of the oven, the experimental setups for making the various measurements and experimental results are then discussed. The measured results from both the vapor temperature diagnostics and the hook diagnostics agree very well. The white-light absorption method is calibrated with the hook method in measuring the lithium vapor density, and proved to be a reliable on-line diagnostics of vapor density measurement in the real harsh experimental environment. The plasma is created by photo-ionizing the lithium vapor with a 193 nm ArF laser. The plasma density is of the order of 10^{14} cm^{-3}, which is proportional to the the UV energy. The homogeneity of the plasma column depends on the uniformity of the laser profiles along the oven. Plasma decays locally due to its recombination and possible diffusion. Plasma density distribution is measured based on UV energy diagnostics and UV beam profile measurements. Preliminary results on the plasma decay time are provided based on the CO_2 laser interferometry method on the diagnostics of a 25 cm plasma source. The plasma density drops from 2×10^{14} cm^{-3} to half of this value in about 3 μS.

Precise knowledge of vapor and plasma density distribution along the 1.4 meter oven are fundamental to the analysis of the experimental results of E-157 experiment.The oven parameters were monitored continuously during the run. White light absorption was successfully used on-line to confirm the desired vapor density. Long term experience of using this type of a plasma source have confirmed that a photoionized heat pipe Li oven is a reliable plasma source for these types of REB plasma experiments.

CHAPTER 4

An Overview of Transverse Beam Effects in E-157 Experiment

4.1 Introduction to E-157

Plasma based accelerators utilizing relativistically propagating plasma waves have been under active investigation because of their potential to accelerate charged particles at gradients that are orders of magnitude greater than those currently employed in radio frequency (rf) accelerators. Conventional rf accelerators are limited to approximately 100 MV/m, due to electrical breakdown on the wall of structure. On the other hand, the accelerating wakefield supported by a plasma wave is in the order of of $\sqrt{n_p[cm^{-3}]}$ V/cm [1], with n_p the plasma density. For plasma densities in the range of 10^{14} cm^{-3} $\sim$ 10^{18} cm^{-3}, the wakefields are in the order of $1 \sim 100$ GV/m. Specifically, such relativistic plasma waves can be excited by using either laser pulses or short electron bunches. Both techniques have shown acceleration of electrons in proof-of-principle experiments [17].

A laser-driven wakefield accelerator is able to generate high density ($\sim 10^{18} cm^{-3}$) plasma waves and therefore high field gradients($\sim$ 100 GeV/m), but only over rather small (< 1 cm) distances due to short Rayleigh lengths of the laser beam [2]. However, an electron beam driven plasma wakefield accelerator (PWFA) is capable of the long acceleration length, at the expense of a decreased accelerating gradient.

The acceleration mechanism of a PWFA scheme is illustrated in Fig. 4.1. In the so-called blow-out regime (defined in Sec. 2.3.1), the plasma electrons are expelled by the space charge of the front of an relativistic electron beam (REB), leaving behind an ion channel. The axis of the ion channel is defined by the head of the REB. Ideally this ion channel provides a uniform (along the direction of propagation of the beam), and linear (in the transverse direction) focusing force on the beam. If the electron beam is approximately half a plasma wavelength ($k_p\sigma_z \approx \sqrt{2}$), the plasma electrons then rush back into the ion channel to produce a longitudinal wake field that can accelerate electrons in the tail of the REB. This wakefield has the phase velocity which is equal to the group velocity of the drive beam, therefore, the tail of the REB can be accelerated for a very significant length before it finally outruns the accelerating field. In reality, this length is

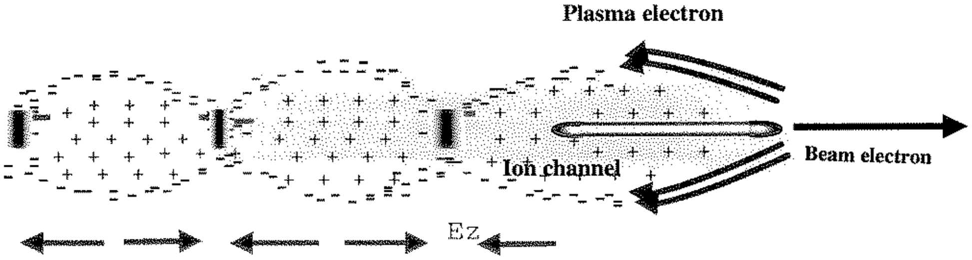

Figure 4.1: An illustration of a PWFA scheme. The drive electron bunch expels plasma electrons and generates an ion channel behind. Plasma electrons rush back and produce a longitudinal plasma wake field which can accelerate the tail of the driver.

much longer than the length of a plasma source [47], therefore, the acceleration length in current PWFA experiments is limited by the length of the plasma.

E-157[1] is the first experiment to study a PWFA over meter-scale distances. The experiment, proposed in 1997, aimed to demonstrate acceleration of electrons with gradients in excess of 100 MeV/m over a distance greater than 1 m. It was conducted at the Final Focus Test Beam facility (FFTB) at the Stanford Linear Accelerator Center (SLAC) (Refer to Appendix C for more details about SLAC and FFTB). It was carried out by a multi-institution collaboration involving Lawrence Berkeley National Laboratory (LBNL), Stanford Linear Acceleration Center (SLAC), the University of California at Los Angeles (UCLA) and the University of Southern California (USC), and spanned over the course of six runs distributed from the Summer of 1998 to the Spring of 2000.

The E-157 schematic is shown in Fig. 4.2. Typical electron beam and plasma parameters used by E-157 are given in Table 4.1.

In the experiment, the SLAC high peak-current REB from the main linac was transported through the FFTB line to a 1.4 m long lithium heat pipe oven. An ArF laser (193 nm) was used to ionize the lithium vapor to produce the plasma. The laser was synchronized with the REB, which was fired at 1 Hz or 10 Hz. The plasma density was varied either by tuning the UV laser output power, or by tuning the timing-delay between the laser firing time and and the REB arrival time at the plasma. The REB was bent by a 5.2 m long dipole bending magnet after it propagated through the plasma. The bending magnet dispersed electrons (300 MeV/mm) according to their energies in Y direction[2]. The REB was finally

---

[1] "E-157" was named by the operators of the Stanford Linear Acceleration Center. It means by that this experiment is the 157th experiment conducted on the Stanford linear accelerator.

[2] In SLAC, it is accustomed to define the beam propagating direction as Z (or S) direction (pointing east), the horizontal direction as X direction(pointing north), and the vertical direction as Y direction (pointing upwards).

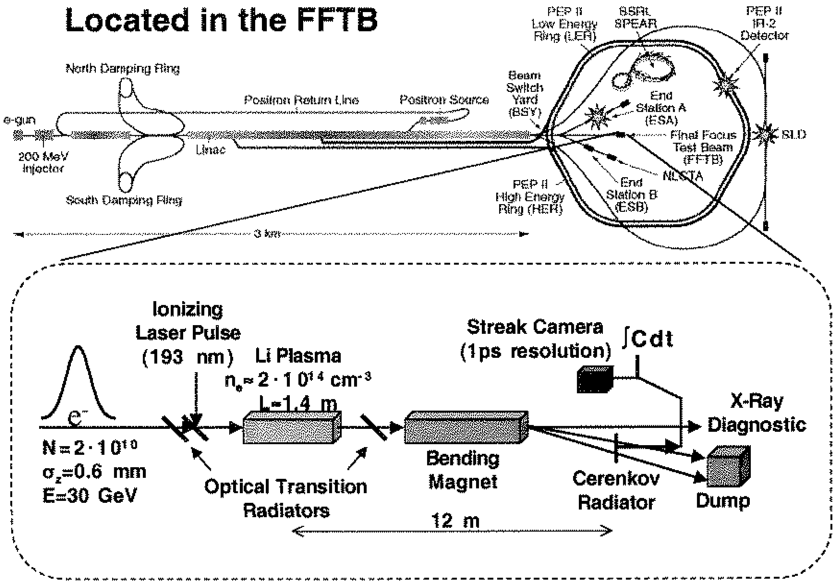

Figure 4.2: (Above) The location of E-157 experiment in the Stanford Linear Accelerator Center. (Below)The E-157 schematic.

Parameter		Value
	Beam Parameters	
Number of Electrons	N_b	$1.8 \sim 2 \times 10^{10}$
Beam Energy	E	$28 \sim 30\ GeV$
Bunch Length (RMS)	σ_z	$0.7\ mm$
Bunch Size (RMS)	σ_x	$30 - 100\ \mu m$
	σ_u	$30 - 100\ \mu m$
Normalized Emittance	$\gamma\epsilon_x$	$50\ mm - mrad$
	$\gamma\epsilon_y$	$5\ mm - mrad$
Repetition Rate		1 or 10 Hz
	Plasma Parameters	
Plasma length	L	$1.4\ m$
Plasma density	n_p	$< 3 \times 10^{14}\ cm^{-3}$
Density uniformity	$\Delta n_p/n_p$	$< 25\%$
Ionization fraction	n_p/n_0	$> 15\%$
Radius	r	$> 400\ \mu m$

Table 4.1: E-157 beam and plasma parameters.

transported to the dump.

As illustrated in Fig. 4.2, there are several diagnostic systems used in the E-157 experiment, which include:

(A) Optical transition radiation (OTR) system. Optical-transition-radiation (OTR) is produced whenever a charged beam cross the boundary between two media with different dielectric constants [48]. The radiation can be used to measure the incident beam profile by imaging the near-field radiation. E-157 exploited optical transition radiation (OTR) to monitor the REB size at the entrance and the exit of the plasma source.

(B) Cherenkov radiation system. Cherenkov radiation is emitted whenever charged particles pass through a medium with a velocity that exceeds the velocity of light in that medium [49]. In E-157, the Cherenkov radiation from the REB was transported to a streak camera so that the centroid and the beam size of the REB could be time-resolved. The system was purposely set up after the bending magnet in order to diagnose the energy variations of the beam tail. More details about the OTR system and the Cherenkov system in E-157 will be introduced in later sections.

Besides the above beam diagnostic systems, there are other conventional beam diagnostic systems provided in the FFTB (not shown in Fig. 4.2). These conventional systems include beam position monitors (BPMs) to measure beam current and beam centroids, wirescanners to measure beam size and beam emittance, etc.. Comparing with these conventional diagnostics, the OTR and Cherenkov systems in E-157 provides 2-D images of the beam shot-to-shot, and they have become indispensable diagnostic tools in the FFTB.

(C)the vapor and plasma density diagnostic systems. White light absorption method was used to diagnose the lithium vapor density in E-157. UV absorption method was used to diagnose the lithium plasma density. Both techniques and results are discussed in Chapter 3.

(D) X-ray diagnostic system. As mentioned in Chapter 2, a beam electron traversing an ion channel is forced to oscillate at the betatron frequency and therefore radiates. The radiated photons were not affected by the bending magnets and went straight through the so called photon beam line. A X-ray diagnostic system was set up at the end of the photon beam line. The X-ray diagnostic system is described in the next chapter.

Although the main intent of the E-157 experiment was to demonstrate high gradient wakefield acceleration by a meter long plasma, E-157 was also the first experiment to systematically study the transverse dynamics of an REB traversing a meter long plasma in the "blow-out" regime. Consequently, a rich variety of transverse beam effects were observed, which are summarized as follows.

(1) Bending an REB with the electrostatic force. As an REB pulse traversing the ion channel has a transverse displacement with respect to the axis of the channel, the beam is steered toward the channel direction due to the asymmetric ion focusing force. As mentioned in Chapter 2, this force can be large enough to exceed the conventional Lorentz force from its magnetic counterpart with attainable plasma densities. The bending of an REB due to the electrostatic force was demonstrated in E-157.

(2) Betatron oscillation of the REB in an ion channel. As mentioned in Chapter 2, an ion channel can also be viewed as a electrostatic potential well, in which a beam electron oscillates with the betatron frequency ω_β, and the envelope of the beam oscillates with the frequency $2\omega_\beta$. While the betatron motion of an individual electron cannot be traced experimentally, it can be represented by the oscillation of the center of mass of the beam if the drive beam has a head-to-tail offset. This is because the head of the beam defines the axis of the ion channel.

Subsequently, the bulk of the charge which has a slight offset with respect to the channel axis oscillates about the center of the channel at the betatron frequency. These oscillations can be measured as transerse deflections of the beam using beam position monitors.

(3) Hosing of the REB. One concern in a PWFA scheme is the electron hose instability [28]. As mentioned earlier, the tail of the beam will oscillate around the axis of the ion channel if the drive beam has a head-to-tail offset. This tail-flipping motion would couple to the motions of plasma electrons at the boundary of the ion channel and lead to the electron hose instability. This instability leads to the exponential growth of the tail oscillation and tears up the beam eventually. In E-157, the tail-flipping motion was investigated and and it was found that the hose instability was not as obvious as the theory predicted.

(4) X-ray radiation due to betatron motion of the REB. As the theme of this thesis, the experimental results of X-ray radiation will be detailed in the next chapter.

4.2 E-157 OTR and Cherenkov Diagnostic Systems

4.2.1 E-157 OTR Diagnostic System

Optical-transition-radiation (OTR) is produced whenever a charged beam cross the boundary between two media with different dielectric constants [48]. The radiation can not only be used to measure the incident beam profile by imaging the near-field radiation, it can also be used to measure the beam energy because the radiation energy and the radiation angular distributions are the functions of the beam energy [50]. The main advantage of OTR is that the radiation production is prompt relative to beam time scale, therefore 2-D (X,Y) visualization of the beam profile, or even 3-D visualization (X, Y, Z) with the help of streak camera is possible.

E-157 exploited the OTR mechanism to measure the beam profile at the entrance and the exit of the plasma source. A thin titanium foil was used to generate the OTR radiation. As illustrated in Fig. 4.3, Each OTR system included a 25 μm-thick Ti foil placed at a 45^0 angle with the electron beam line, an AF Micro-Nikkor 105 mm, F2.8 lens to 1:1 image the OTR, and a 12-bit Photometrics Sensys CCD camera. The CCD had a pixel size of 9 μm × 9 μm with an array size of 768×512, and the spatial resolution was approximately 20 μm[3]. The

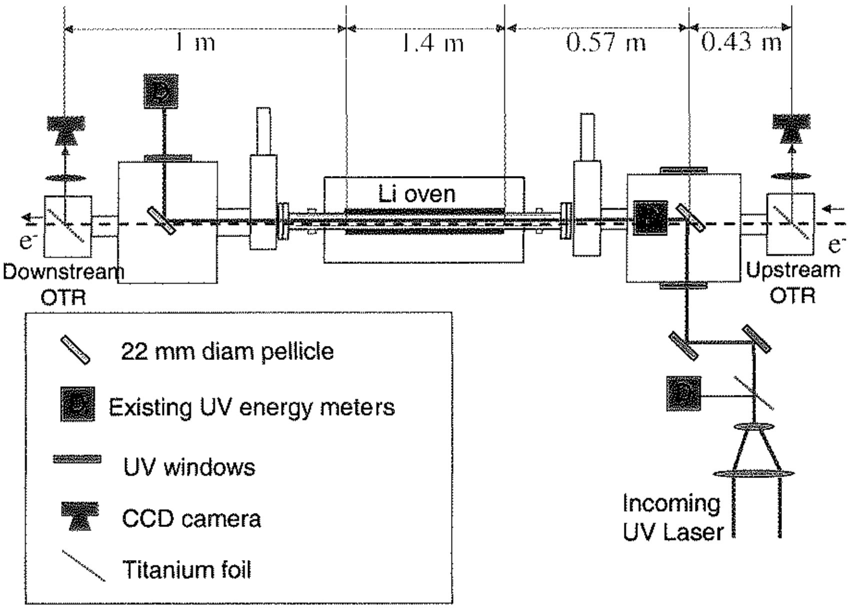

Figure 4.3: E-157 schematic at IP1. Two OTR systems were located at the upstream and the downstream of the Li oven, respectively.

---

[3] This resolution has included the effect of the OTR angular acceptance θ_a, which would lead to $FWHM \approx 1.44\lambda/\theta_a$, with λ the radiation wavelength and FWHM the full-width-half-maximum image of a point source.

image acquisition was synchronized with the beam-firing rate, which was 1 *Hz* or 10 *Hz* for the SLAC beam.

Typical OTR images acquired from the CCD cameras in the E-157 experiment are shown in Fig. 4.4. Raw images were then analyzed in Matlab routines to extract information such as the beam spot size and the beam centroid.

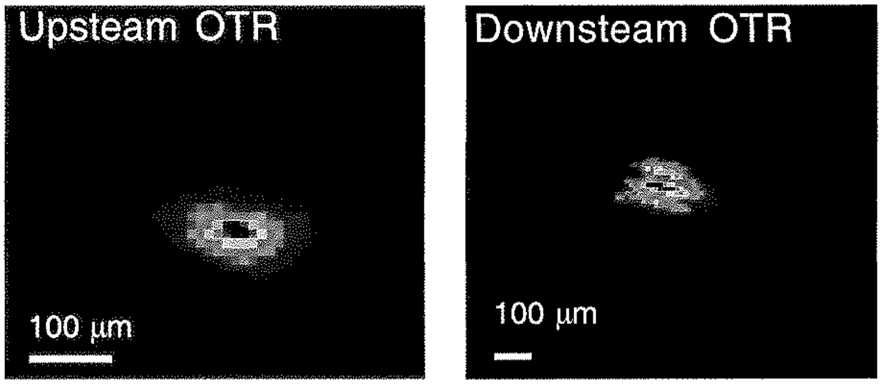

Figure 4.4: Upstream and downstream OTR images in E-157 experiment. The graininess of the downstream OTR image was not due to the beam, rather it resulted from the grain structure of the titanium foil.

4.2.2 E-157 Cherenkov Diagnostic System

Cherenkov radiation is emitted whenever charged particles pass through a medium with a velocity that exceeds the velocity of light in that medium [49]. A 3 *mm* thick aerogel with the refractive index of 1.009 was chosen as the medium in E-157. The Cherenkov radiation diagnostic system was built to temporally resolve the beam profile and electrons' energies [4].

The Cherenkov diagnostic system of E-157 is illustrated in Fig. 4.5. After

---

[4] A preliminary test proved that the photon yield from an aerogel-based Cherenkov system was more than an order of magnitude higher than that from OTR [51]. Therefore a Cherenkov system was more favorable than an OTR system in energy gain diagnostic.

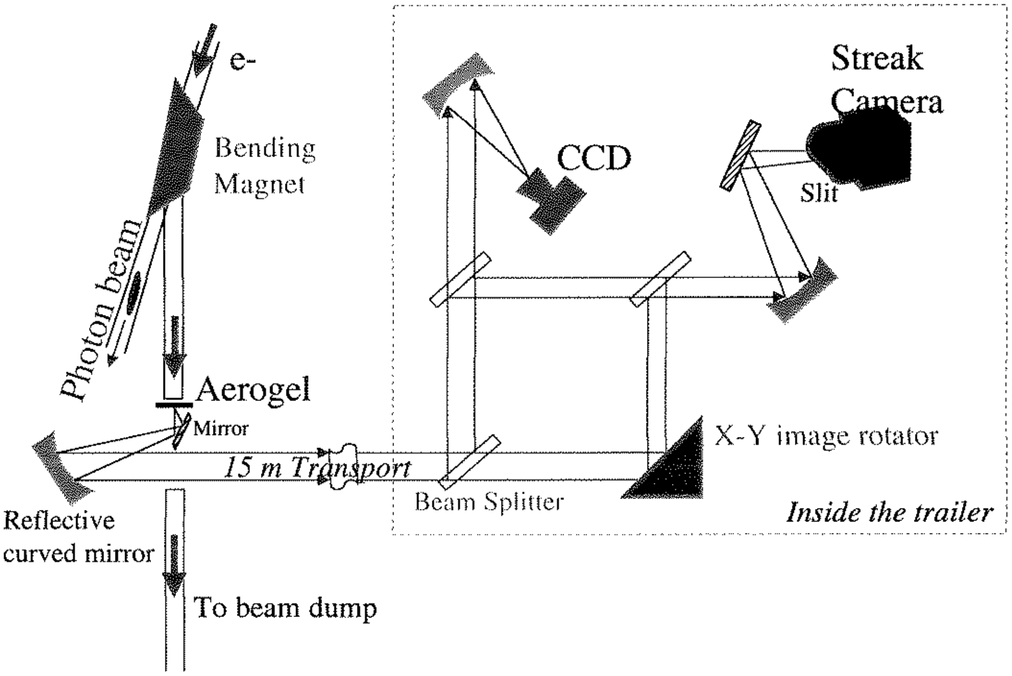

Figure 4.5: The Cherenkov diagnostic system in E-157.

an electron beam got dispersed in Y direction by the bending magnet, it hit the aerogel and emitted the Cherenkov radiation. The radiation light was imaged onto a CCD camera located in a trailer which was 15 meters away from the FFTB, by passing through a series of optical components. Some of the light was divided with a beam splitter before being sent to a Hamamatsu streak camera to get streaked in the time domain. Since a streak camera can only accept a slit of light in one axis (because another axis is used for time dimension), light was divided again and rotated, so that the streak camera resolved the image on the aerogel in both horizontal(X) and vertical (Y) direction. One arm of light was purposely delayed so that both images can be caught in one scan of the streak camera. Typical Cherenkov images from the CCD and the streak camera are shown in Fig. 4.6. Since the bending magnet dispersed the electrons in the Y direction according to their energies, the vertical part of streak images was used for energy gain diagnostics, while the horizontal part was for transverse dynamics.

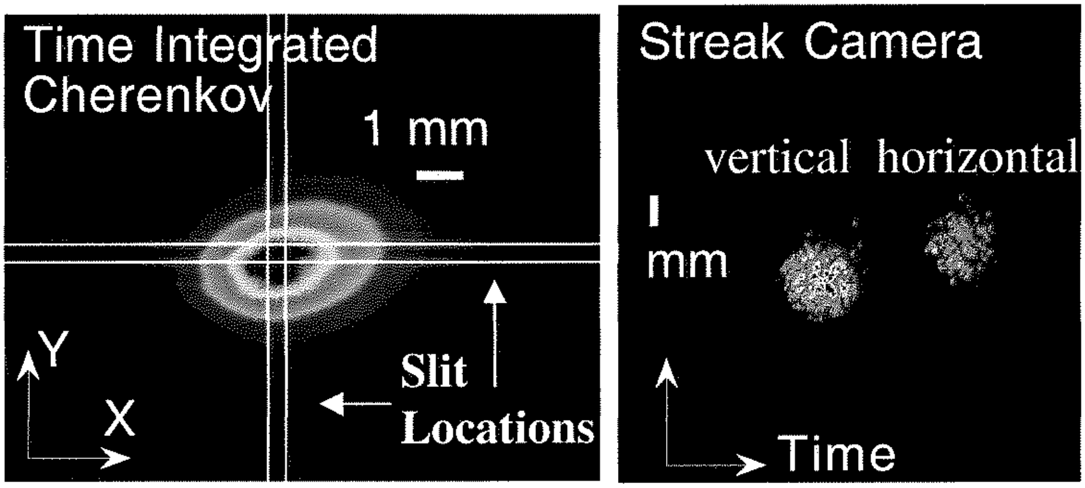

Figure 4.6: (Left) A typical time-integrated-Cherenkov image on the CCD camera. "Slit locations" indicates the parts of the beam accepted by the streak camera in X and Y directions. (Right) Typical streak camera image showing both the horizontal and vertical streaks.

The dispersion in the aerogel plane was 285 MeV/mm. The imaging resolution was about $\approx 100\ \mu m$ in both planes corresponding to 28.5 MeV in the Y plane.

4.3 E-157 Transverse Dynamics

(A) *Bending an REB with the Coulomb force* [5]

It is not new to use the Lorentz force provided by a magnet to bend an REB beam. However, it is new to use the collective Coulomb force supported by an ion column instead of the Lorentz force to bend an REB. As mentioned in Chapter 2, An electron would experience the ion channel force if it is displaced from an ion channel. This ion channel force is proportional to the ion density, which would be large enough to exceed the Lorentz force from its magnet counterpart with attainable plasma densities. The schematic for both mechanisms for bending electrons are illustrated in Fig. 4.7.

Although the schematic is so simple, it is not trivial to pre-produce an ion channel and send an REB which has a transverse displacement from the axis of the channel. We demonstrated this effect using an alternative method in the E-157 experiment. Its schematic is illustrated in Fig. 4.8. An REB was sent at an angle θ with respect to the axis of a plasma column such that it encountered a plasma-neutral gas boundary. The head of the beam expelled the plasma electrons, and formed an ion channel through which the tail of the beam traversed. The ions provided the Coulomb force which, however, would have no deflected effect on the beam centroid if the beam was symmetrically distributed around the beam. However, when the beam came near the plasma-gas boundary, the ion channel became asymmetric, and the formation of an asymmetric ion-focusing force gave rise to the bending of the beam path at the interface. Figure 4.9 shows a snapshot

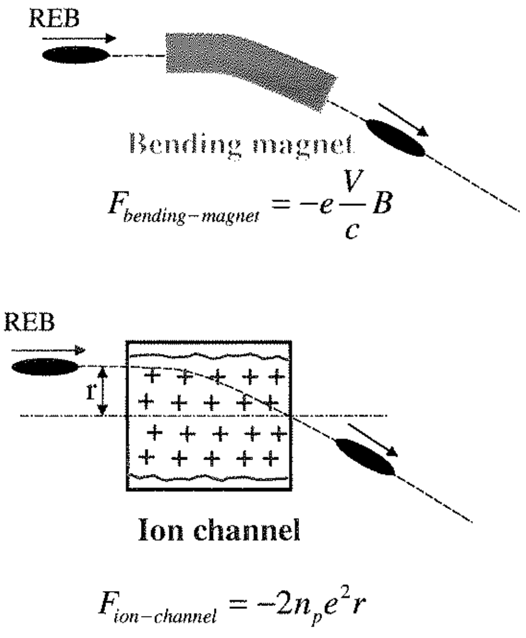

Figure 4.7: The comparison of two different schematics in bending an REB.

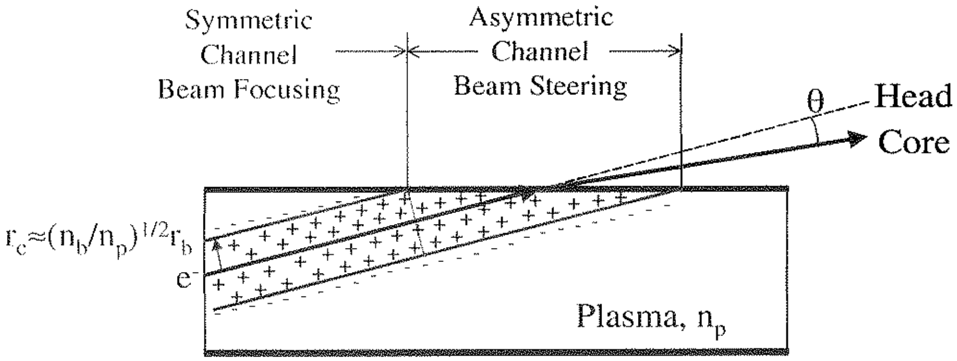

Figure 4.8: The E-157 schematic for the demonstration of bending an REB with the Coulomb force.

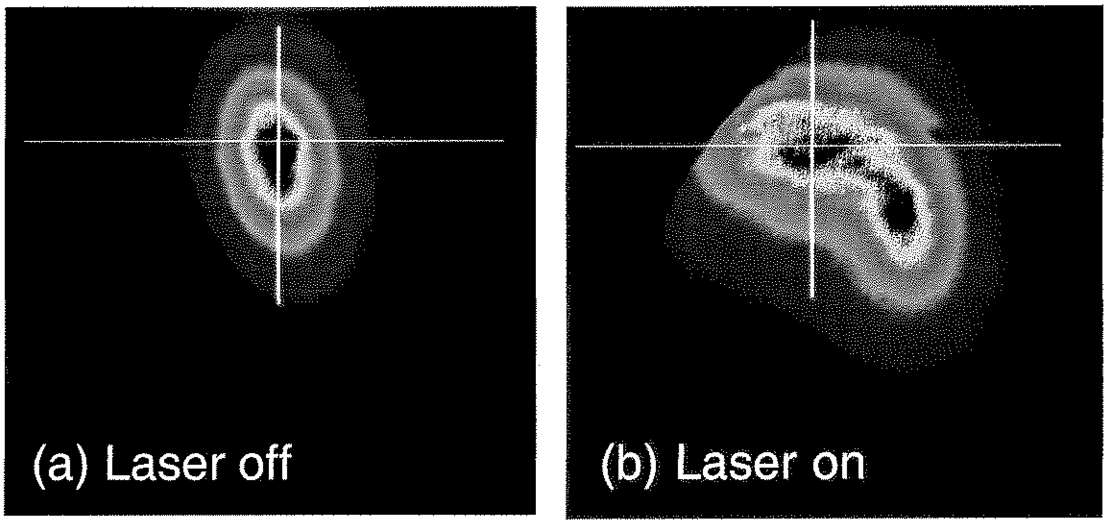

Figure 4.9: The image of the beam downstream (received by the Cherenkov time-integrated CCD camera), with (a) Laser off and (b) Laser on, shows the deflected beam and the undeflected transient. The cross hair marks the position of the head of the beam.

of a Cherenkov image with (a) plasma off and (b) plasma on. The cross hair on the figure marks the position of the head of the beam which is undeflected as expected. The rest of the beam sees an assymetric ion column and is toward the direction of this plasma column due to the Coulomb force.

(B) *Betatron oscillation of an REB in an ion channel*

As mentioned in Chapter 2, an electron traversing an ion channel oscillates transversely with the betatron frequency ω_β, and the beam envelope oscillates at $2\omega_\beta$. The motion of the beam centroid is equivalent to that of an electron if the beam has a head-to-tail tilt. The reason is as follows. Since the head of the beam produces an ion channel, the axis of the ion channel is defined by the head of the beam. Therefore the main body of the beam experiencing the ion channel has an initial transverse offset with respect to the axis of the channel. This causes the beam centroid to oscillate about the axis with the betatron frequency as an individual beam electron does.

In E-157, the multiple oscillations of the beam inside the ion channel were clearly inferred from the variations of both the beam size and periodic oscillations of the beam centroids as a function of plasma density.

Figure 4.10 plotted both the beam sizes (measured with the downstream OTR) and the concurrent X position of the beam centroids (measured with the downstream BPM) as a function of plasma density. Each dot in the figure corresponds to each shot of the REB traversing a 1.4 m plasma source. The beam was tuned to have a head-to-tail tilt at the entrance of plasma. The plasma density increased from 0 to 2×10^{14} cm^{-3}. Figure 4.10 clearly shows that the beam centroid oscillated at the half of the envelope oscillation frequency. The marks in the figure indicate the transparency points at which the beam size recovers to its original size when there is no plasma. At theses points beam electrons executed an integer number of betatron oscillations in the plasma, i.e., the phase advance experienced by each beam electron satisfies

$$\Psi \approx L_{oven}\frac{\omega_\beta}{c} = L_{oven}\sqrt{\frac{2\pi n_p e^2}{\gamma m c^2}} = m\pi, \tag{4.1}$$

with $m = 1,\ 2,\ 3\ldots$ the integral number. The corresponding plasma densities at the transparency condition can be calculated based on the above equation.

The solid curves in Fig. 4.10 were plotted based on the following theory. The focusing force of the ion channel on an inserting REB is equivalent to that of a thick quadrupole [52]. The corresponding lens strength of the quadrupole k_β is the betatron wavenumber, which is

$$k_\beta = \frac{\omega_\beta}{c}, \tag{4.2}$$

with n_i the ion density and γ the Lorentz factor of the REB. The transfer parameters C and S, which govern the trajectory of the REB from the entrance of

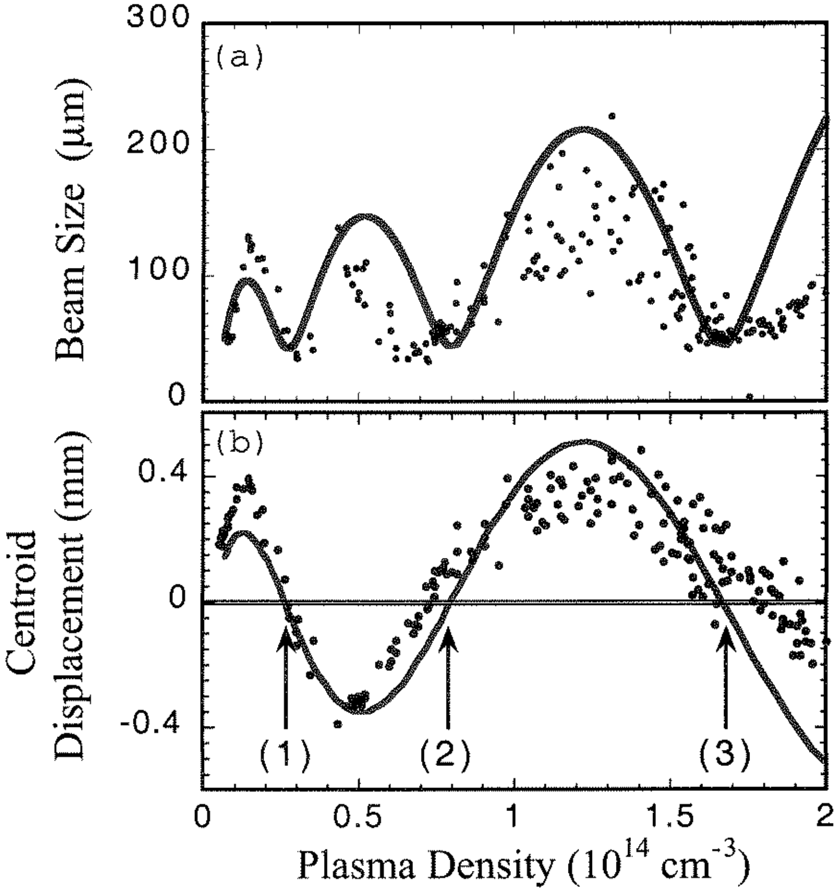

Figure 4.10: (a) Multiple oscillations of the spot-size measured with the downstream OTR system due to betatron motion of a 28.5 *GeV* electron beam traversing a 1.4 *m* long lithium plasma as a function of the plasma density. The solid line was the curve-fit with Eq. 4.6. (b) The beam centroid oscillations measured with the downstream BPM (6130) as a function of plasma density. The solid line was the curve-fit with Eq. 4.5. The marks, (1),(2),and (3), in the figure indicate the transparency points, which also correspond the minimum spots in (a).

the ion channel to the downstream BPM, are given by [52]

$$C = cos(k_\beta \cdot L_{oven}) - k_\beta \cdot L \cdot sin(k_\beta \cdot L_{oven}), \tag{4.3}$$

$$S = L \cdot cos(k_\beta \cdot L_{oven}) + (1/k_\beta) \cdot sin(k_\beta \cdot L_{oven}), \tag{4.4}$$

where $L = 2.63\ m$ was the distance from the exit of the ion channel to the BPM, and $L_{oven} = 1.4\ m$ was the oven length. Based on these transferred parameters, the beam centroid measured by the BPM satisfies

$$r = C \cdot r_0 + S \cdot r_0', \tag{4.5}$$

by assuming that the the beam centroid at the entrance of the ion channel has an offset r_0 and a transverse slope $r_0' = dr_0/dz$. The beam size at the downstream OTR was calculated based on the beta-function β of the beam, which satisfies [26]

$$\sigma = \sqrt{\beta \cdot \frac{\epsilon_\gamma}{\gamma}} = \sqrt{(C^2\beta_0 - 2CS\alpha_0 + S^2\gamma_0)\frac{\epsilon_\gamma}{\gamma}} \tag{4.6}$$

with α_0, β_0 and γ_0 being the Twiss parameters at the entrance of the oven[5], and ϵ_γ the normalized emittance of the beam. C and S are defined in equations 4.3 and 4.4 except that $L = 1.0\ m$ here, since the downstream OTR was 1.0 m away from the exit of the plasma.

The theoretical curve on Fig. 4.10(a) was obtained by fitting the experimental data with Eq. 4.6, with ϵ_γ as the fitting parameter. The curve-fit process yielded $\epsilon_\gamma = 1.5 \times 10^{-4}$. The theoretical curve on Fig. 4.10(b) was obtained from the curve-fit of the experimental data with Eq. 4.5. The initial parameters of the beam centroid r_0 and r_0' are parameters to be fit. The curve-fit process yielded $r_0 = 32\ \mu m$ and $r_0' = 0.07 \times 10^{-3}$ for this run.

---

[5] α_0, β_0 and γ_0 ($\beta_0\gamma_0 - \alpha_0^2 = 1$) at the entrance of the oven were measured with quad-scan in E-157. $\beta_0 = 0.8\ m$, $\alpha_0 = -0.25$ were reasonable E-157 parameters and were used here [52].

The agreement between the theoretical curve and the experimental data is reasonably good especially at smaller plasma plasma densities. As plasma densities become larger, more beam electrons have to be used to push plasma electrons away. Therefore the beam behavior is not well described by the above simplified theory where the a pure ion channel is assumed to be preformed.

It should be noted that another theoretical model based on the beam envelope equation was also successfully used to curve-fit the experimental data of the beam sizes measured with the downstream OTR, which were detailed in reference [53].

(C) *Sloshing and Hosing of an REB in a plasma*

As mentioned earlier, the tail of the beam oscillates with the betatron frequency ω_β in an ion channel provided that the REB has a haed-to-tail tilt. Under certain conditions, this oscillation will grow exponentially due to the electron hose instability [28]. Hosing results from the coupling of transverse beam displacements to plasma electrons at the boundary of the ion channel. As illustrated in Fig. 4.11, the sloshing of the tail with the characteristic frequency ω_β initiates the displacement of plasma electrons at the boundary. The typical oscillation frequency of the collective motion of these plasma electrons is $\omega_0 \approx \omega_p/\sqrt{2}$, which differs from ω_p because they are at the boundary between a region of electron density n_p and a region of zero density. The coupling of this two harmonic oscillating drivers can be described by the following two differential equations [28],

$$c^2\partial_s^2 x_b + \omega_\beta^2 x_b = \omega_\beta^2 x_c, \tag{4.7}$$

$$\partial_\xi^2 x_c + \omega_0^2 x_c = \omega_0^2 x_b, \tag{4.8}$$

where $\xi = z - ct$ and $s = z$. In these equations the beam centroid x_b is driven by the channel centroid x_c, and vice versa. This coupling would lead to the

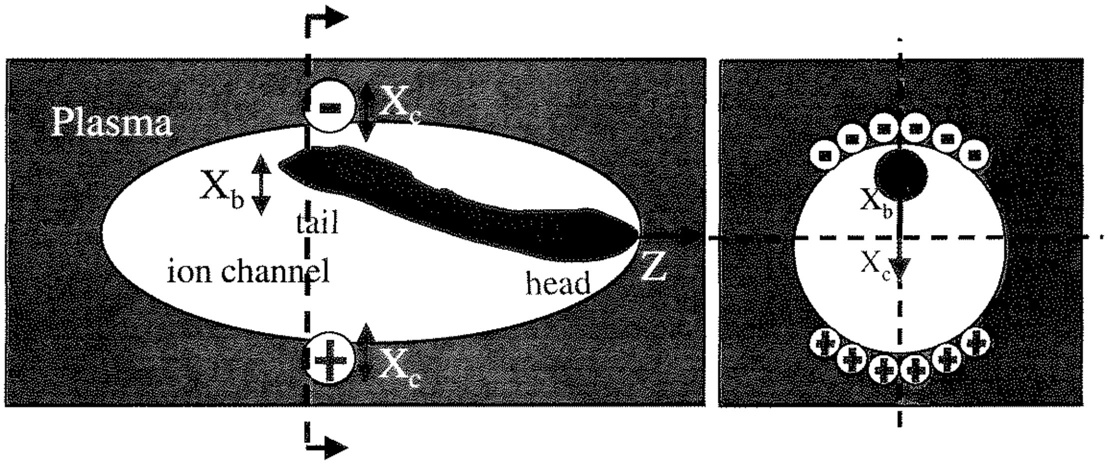

Figure 4.11: (Left) An illustration showing that an REB beam with a head-to-tail tilt enters the plasma in z direction, forming an ion channel for the tail to experience. (Right) A beam slice in the ion channel, displaced by an amount x_b, induces a displacement x_c of the channel.

exponential growth of the tail oscillation. At the same time the different segments of the beam would oscillate at different frequencies. Hose instability raises a serious issue about the ability to propagate an REB over long distances in dense plasmas.

In the E-157 experiment, we diagnosed the relative position of each beam segment by temporally resolving the Cherenkov images in the non-dispersion (X) plane [54]. As there was no plasma (the laser was off), we measured the initial positions of the beam slices and used them as the initial condition for theoretical estimation. We then acquired the beam slices at three different transparency points. By doing so, we minimized the drifting distance of each beam segment due to its transverse momentum acquired from the ion channel. Finally we compared the experimental data with theory and plotted Fig. 4.12.

The dashed lines in Fig. 4.12 are the time-sliced beam centroids (dashed lines) measured with the Cherenkov radiation images. The solid curves are based on the numerical integrations of equations 4.7 and 4.8 using the initial conditions provided in Fig. 4.12(a). Figure 4.12(c) and (d) clears show that the theory predicts a much larger tail growth than the experimental data. They also show that the beam segments began to oscillate at different frequencies at these plasma densities. The experimental data does show a slight tail growth at the third transparency point by comparing Fig. 4.12(a) and (d). However, it was most likely due to the initial transverse momentum of the beam segments at the entrance of the plasma.

The discrepancy between the theory and the experimental results is probably due to the fact that the theory assumes that a pre-formed channel with a constant radius exists whereas in many experimental situations the dynamically formed ion channel has a longitudinally varying radius. The theory also neglects any non-ideal experimental factors such as asymmetric beams and longitudinal density gradients. All these factors tend to suppress the hosing growth.

A computer simulation (OSIRIS) based on E-157 parameters also indicates a smaller growth rate of hose instability than the theory described in Eq. 4.7 and 4.8 [55].

4.4 Summary

The main transverse effects in the E-157 experiment has been reviewd in this chapter.

The beam diagnostic systems built in E-157, the OTR and the Cherenkov system, have been introduced. They provide 2-D and 3-D visualization of the beam profile on a pulse to pulse basis, and have become indispensable tools in FFTB and SLAC. The main E-157 transverse effects have been reviewed, such

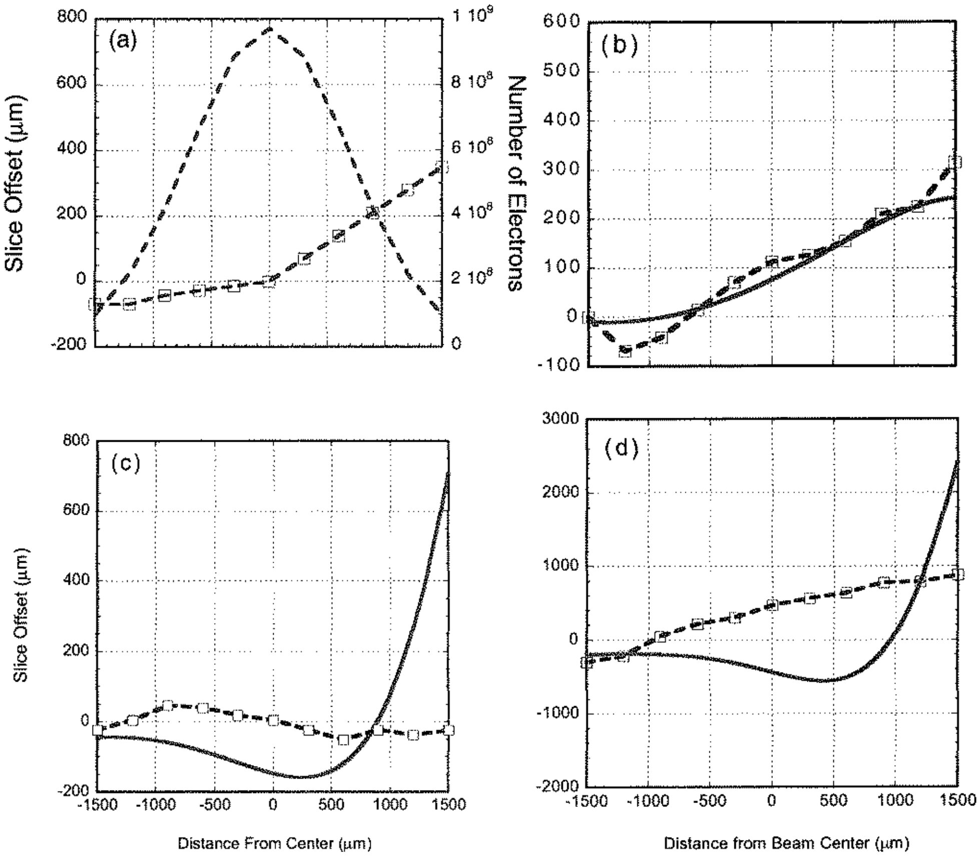

Figure 4.12: Time-sliced beam centroids (dashed lines) measured with the Cherenkov radiation images recorded by the streak camera are compared with those from the theoretical estimation (solid lines) based on Eq. 4.7 and 4.8 at three transparency points. (a) $n_p = 0$, the beam centroids shows a initial head-to-tail (left-to-right) tilt. (b) $n_p \approx 0.3 \times 10^{14}\ cm^{-3}$, $\omega_\beta L_{oven}/c \approx \pi$. (c)$n_p \approx 0.8 \times 10^{14}\ cm^{-3}$, $\omega_\beta L_{oven}/c \approx 2\pi$. (d)$n_p \approx 1.7 \times 10^{14}\ cm^{-3}$, $\omega_\beta L_{oven}/c \approx 3\pi$.

as bending an REB with the Coulomb force; betatron oscillations of an REB in an ion channel; sloshing and hosing of an REB in a plasma. Theories related to these phenomena have been addressed. Agreements between experimental results and theories are reasonable for most phenomena.

CHAPTER 5

X-Ray Emission From Betatron Motion In A Plasma Wiggler

5.1 Introduction

Synchrotron light sources are used for basic and applied research in physical, chemical and biological sciences, and in engineering [8]. These use magnetic undulators and wigglers to generate high brightness photon beams in the X-ray region using relativistic electron beams. In this chapter it is shown that an ion channel induced by an electron beam as it propagates through a plasma can wiggle the beam electrons to generate X-ray radiation. Because a dense column of ions can provide an effective wiggler strength that can be much greater than that provided by a conventional magnet, such plasma wigglers /undulators [6][9][12] could impact future generation light sources.

It is known from Chapter 2 that an electron beam injected into an ion column undergoes betatron oscillations of its transverse envelope or beam size. An individual electron within this beam executes simple harmonic motion about the axis of the ion channel with betatron frequency $\omega_\beta = k_\beta c = \omega_p/\sqrt{2\gamma_b}$ where $\omega_p = \sqrt{4\pi n e^2/m}$ is the plasma frequency, n is the plasma density, and γ_b is the relativistic Lorentz factor of the beam. The betatron motion of a relativistic electron with an initial displacement r_0 from the axis of the ion channel is described by $\vec{r} = \vec{r_0} \cos\phi$, leading to $\vec{\beta_r} = -\vec{r_0} k_\beta \sin\phi$, and $\dot{\vec{\beta_r}} = -\vec{r_0} k_\beta \omega_\beta \cos\phi$ with $\dot{\phi} = \omega_\beta$. The total radiation power as a consequence of this motion is given by [23] $P(t) = \frac{2e^2\gamma_b^2}{3m^2c^3}[\dot{\vec{p}}^2 - m^2c^2\dot{\gamma_b}^2] \approx \frac{2}{3}ce^2\gamma_b^4 r^2 k_\beta^4 \cos^2\phi$ where $\vec{p_r} = \gamma_b mc\vec{\beta_r}$. Therefore the total power is proportional to ω_β^4 which scales as the square of the plasma density. The spectrum of this betatron radiation has resonance frequencies at $\omega_r = 2m_h\gamma_b^2\omega_\beta/(1 + K^2/2 + (\gamma_b\Omega)^2)$ where $m_h = 1, 2, 3\cdots$ is the harmonic number[24]. The wiggler strength K is given by $K = \gamma_b\omega_\beta r_0/c$, and $\Omega << 1$ is the observation angle measured from the axis. For a beam with a transverse size σ_r, each electron has a different r_0 and radiates a different ω_r and the spectrum of radiation therefore tends to be broad. If $K >> 1$, high harmonic radiation dominates the spectrum and a broadband spectrum is generated as from a conventional wiggler. This broadband spectrum is characterized by the critical frequency [23] given by $\omega_c = 3\gamma_b^3 c r_0 k_\beta^2/2$. The full width at half-maximum (FWHM) beam divergence angle is $\theta \sim K/\gamma_b$ which can be extremely narrow for an ultra-relativistic beam. Although microwave radiation has been observed in this underdense or ion-focussed regime [56], no measurements of X-rays have been reported to our knowledge.

The plasma wiggler experiment was conducted as a parasitic experiment to E-157. As shown in Fig. 4.2, the X-ray diagnostic system was located at the end of photon beam line in FFTB. We used Thomson scattering technique and Bragg scattering technique to detect the X-ray photons in our experiment. Thomson scattering technique was used to measure the relative values of X-ray power as a function of plasma density and Bragg scattering was used to measure photon numbers because the photon energy can be precisely determined at the Bragg angle. We also used a fluorescer to visualize the X-ray images at the end of photon beam line.

In the following sections, I first review the background knowledge of both Thomson scattering and Bragg scattering techniques. Then I introduce two preliminary experiments, the first is about X-ray scattering, and another is about X-ray imaging. After that, I address the main X-ray experimental results and their comparisons with theoretical estimations. I summarize this chapter in the final section.

5.2 X-ray Diagnostic Techniques

5.2.1 Thomson Scattering

According to the classical electromagnetic theory [23], a free electron may scatter an incident plane wave of monochromatic electromagnetic radiation with the scattered intensity satisfying the *Thomson formula* [57], which is $I_e = r_e^2 I_0(1+cos^2\theta)/2$, with I_e the energy scattered per unit solid angle per unit time, r_e the classical electron radius, I_0 the incident power per unit area, and θ the angle between the incident radiation vector and the scattered radiation vector.

The Thomson scattering radiation energy applied to an atom with bounded electrons Z is formulated as [57] $I_s = f_a^2 I_e$, with f_a the mean atomic scattering factor. The factor f_a only depends on a parameter $s = sin(\theta/2)/\lambda$ with the scattered angle θ and the radiation wavelength λ. f_a is available for most known atoms [58]. Figure 5.1 demonstrates f_a of a $Z = 14$ silicon atom as a function of the radiation energy at two difference scattered angles, $\theta = 8^0$ and $\theta = 18^0$.

It should be noted that for a single atom the scattered intensity due to Compton scattering would be appreciable compared to that due to Thomson scattering, especially at the large scatterd angle [57]. However, in Compton scattering since the incident and the scattered radiations do not have the same wavelength, there

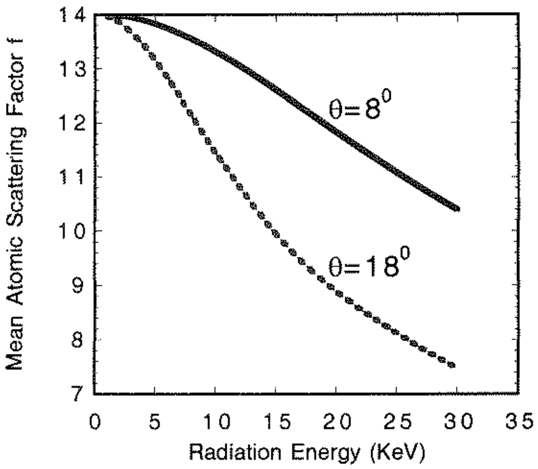

Figure 5.1: The mean atomic scattering factor f_a of a $Z = 14$ Silicon atom as the function of the radiation energy at two difference scattered angles, $\theta = 8^0$ and $\theta = 18^0$ [58].

is no definite phase relation between them and the radiation from each scattering element is incoherent. In the scattering of X-rays from crystals, very large numbers of atoms co-operatively scatter so that the amplitudes of the Thomson scattering from different atoms add together whereas for Compton scattering it is the intensities which add. Therefore Compton scattering may be ignored in considering scattering of X-rays from a crystal.

5.2.2 Bragg Scattering

If a continuous spectra of X-rays hit a crystal at an angle θ and the grid planes of the crystal have a spacing d, then The "reflection" (scattering) of X-rays at wavelength λ would be enhanced dramatically if the relation between d, θ , and λ is given by the Bragg reflection condition,

$$2dsin\theta = m\lambda, \tag{5.1}$$

where m is an integer. The reflectivity of photons satisfying Bragg reflection condition would be effectively close to 100% if the scattering crystal is perfect and its thickness is more than thousands of scattered wavelength [59]. The resolution of the scattered photon energy can be expressed as

$$E/dE = -d\theta/tan(\theta), \tag{5.2}$$

with the scattered photon energy $E = hc/\lambda$, and $d\theta$ the angle resolution of the X-ray Bragg spectrometer system[1].

Bragg scattering techniques have been extensively used in monochromators in many synchrotron light-source beamlines for photon energies of 500 eV to 100 KeV. For lower energies one need to use organic crystals or multilayer structures such as gratings.

5.3 Preliminary Experiments

5.3.1 X-ray Scattering

The schematic of X-ray scattering diagnosis used in E-157 is shown in Fig. 5.2. The crystal used for Thomson and Bragg scattering of incident X-rays out of photon beam lines was a 5″ diameter, 1 mm thick silicon crystal (Virginia Semiconductor, INC.). The crystal was set on a rotation stage whose angle resolution was $\leq 0.25^0$. Two SBDs (surface barrier detectors) (Model 142A of EG&G), D1 and D2, were set about 30 cm away from the center of the crstal with the refletion angle θ being 8^0 and 18^0 respectively.

---

[1] This resolution also includes the angular resolution intrinsic to the the crystal structure, which is characterized by the FWHM of the Rocking curve [57] of the crystal. For a perfect, 1 mm thick Si crystal used in the vicinity of (111) direction, the FWHM of its Rocking Curve is no more than 7″ [60], which is much smaller than the angular resolution of a conventional X-ray Bragg spectrometer.

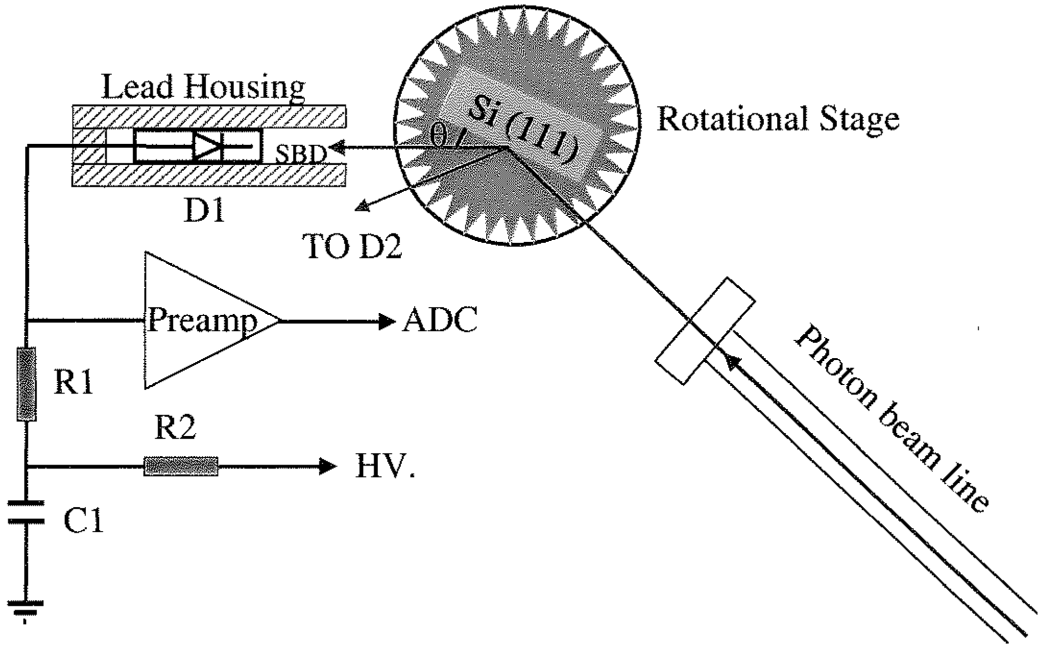

Figure 5.2: The schematic of X-ray scattering diagnosis in E-157. An SBD is reversely biased through two large resistors R1 and R2. The current generated by the incident radiation is collected by the input capacitance of the charge sensitive preamp. High voltage is supplied by a NIM module. Only one detector D1 together with its circuit are drawn. D2 has an identical circuit as D1, which is omitted in the figure.

SBDs together with low-noise current amplifiers are extensively used in measuring the X-ray flux. A SBD in E-157 experiment is essentially an n-type silicon substrate with a layer of oxidation and two metal contacts. The oxidation layer forms a "surface barrier" which causes the device to behave like a diode. When the SBD is reverse biased, depletion region forms adjacent to the silicon-oxide junction. When radiation passes through the depletion region, electron-hole pairs are created through ionization. These free charges are accelerated by the electric field in the depletion region and are subsequently collected at the electrodes. The average photon energy required to generate an electron-hole pair is 3.6 eV. For example, an 1 KeV X-ray photon can create $\sim$ 300 pairs. Once the charge Q is generated in the SBD, it is collected on a capacitor C, and produces the voltage $V = Q/C$, which is read out through a charge sensitive preamp. Since the SBDs are sensitive to any type of radiation, measures must be taken to insure that the radiation of interest dominates the signal. The detectors were therefore inserted into open ended lead containers with the thickness of the lead more than $2''$. The lead containers effectively blocked radiation from other directions hit the detectors.

Figures 5.3(a) and (b) demonstrate X-ray signals received by both detectors as a function of the rotational angle of the silicon crystal with plasma off. The peaks in the figures are due to Bragg scattering. The corresponding respective photon energy, received by D1(D2) which had a reflection angle 8^0 (18^0), was 6.5 KeV (14.2 KeV). The FWHM of Bragg peak could not be resolved due to the limitation of the resolution of the rotational stage.

Apart from the Bragg peaks, other X-ray signals in the figures were due to Thomson scattering. These signals increased as the rotational angle got smaller, and reached maximum as the rotational angle near 0^0. This is because the inten-

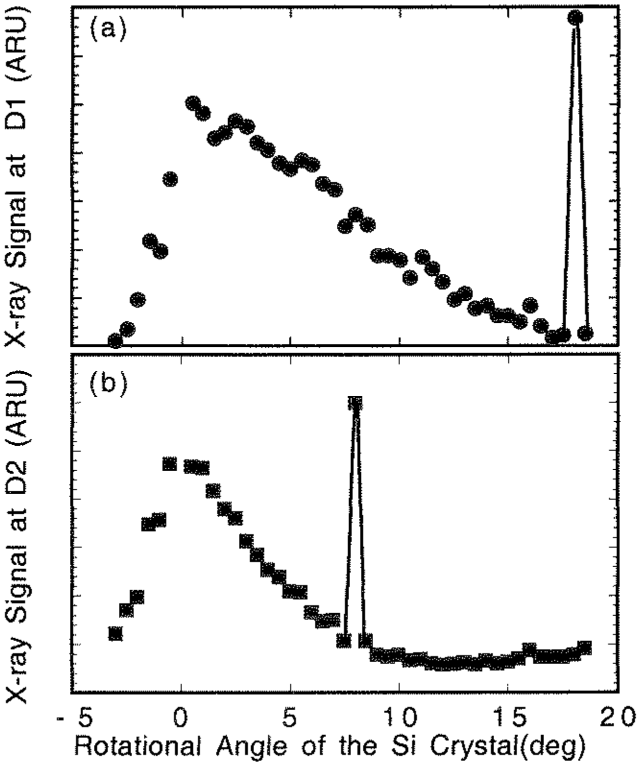

Figure 5.3: X-ray signals received by (a) D1 and (b) D2 as a function of the rotational angle of the silicon crystal with plasma off.

Item	Material	Thickness (μm)	transmission
1	Al	5	0.86
2	Al	75	0.66
3	Al	100	0.63
4	Cu	25.4	0.32
5	Si	1000	0.25
6	Cu	100	0.05
7	Mo	127	0.02
8	Cu	254	0.01

Table 5.1: Eight different filters, their thickness and their relative transmissions of X-rays covering photon energies from 2 KeV to 30 KeV.

sity of Thomson scattering radiation increases with increase of the the volume of the scattering atoms. At $\theta \approx 0^0$ there is the longest interaction length overlapping with the inserting X-rays, and therefore yield the largest Thomson scattering signal.

It should be noted that even though the X-rays in the FFTB are broadband, X-rays received by SBDs at the end of the photon beam lines are only in the range from 2 KeV to 30 KeV in the spectrum. This is because those photons with their energies smaller than 2 KeV were stopped by two 75 μm thick beryllium windows and those with energies larger than 30 KeV were transmitted through the depletion region ($\sim 1\ mm$ thick) of SBDs. The following experiment verified the above argument.

Eight different foils were set respectively in front of D1 to measure the transmission of Thomson scattered radiation. Parameters of these foils such as material, thickness and transmissions are listed in Table 5.1. The transmission values are calculated by numerically integrating the X-ray transmissions from 2 KeV to 30 KeV [61]. Figure 5.4 shows the comparison between the measured X-ray transmission values and the theoretical ones. They agreed with each other reasonably well.

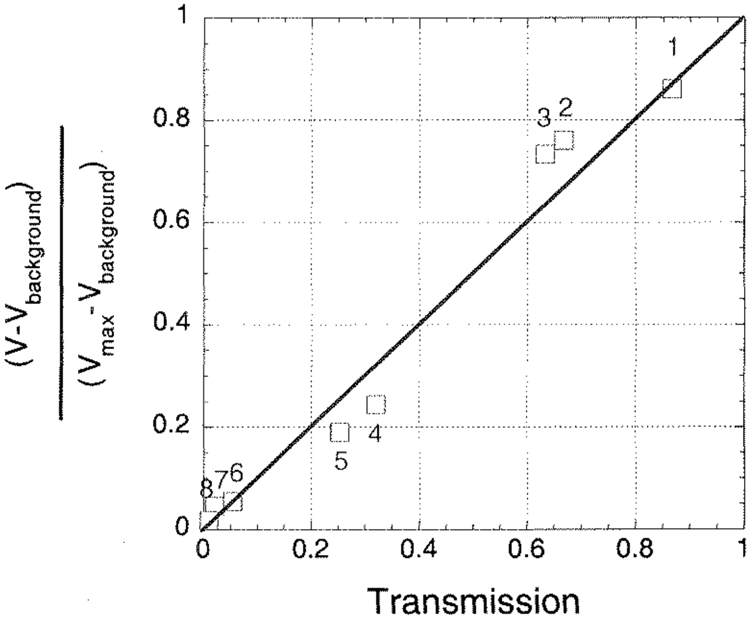

Figure 5.4: The measured X-ray transmissions $(=(v - v_{background})/(v_{max} - v_{background}))$ of eight foils were plotted against the corresponding theoretical transmissions. V_{max} was the SBD signal without any filter in front of the SBD, while $V_{background}$ was the SBD signal with a thick Pb in front of the SBD. The marks corrsponds to the items listed in Tab. 5.1. The solid line is drawn to guide the eye.

5.3.2 X-ray Fluorescence Techniques

The schematic of the X-ray image diagnostic is shown in Fig. 5.5. A fluorescer, which is a 10 μm thick aluminum film covered with a very fine material of photostimulated phosphor, was set at the exit of the photon beam line in FFTB, with a 8-bit CCD camera recording the X-ray fluorescence image. Figure 5.6 is a

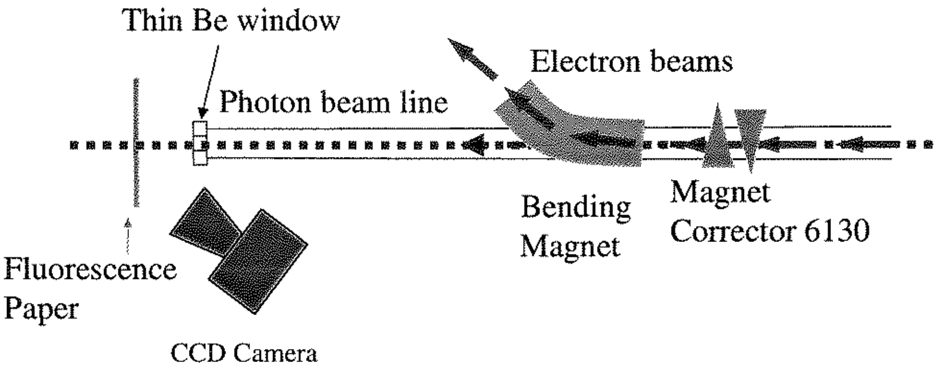

Figure 5.5: X-ray fluorescence schematic.

typical fluorescence image recorded by the camera on which radiations from different sources were annotated. The radiation at the "head" part of the "tadpole" would be from bremsstrahlung, transition radiation, and betatron radiation if the plasma is on, while the radiation at the tail part is from synchrotron radiation due to all of the upstream magnets. The following experiment illustrated how a radiation image could be varied by moving the beam centroid. A magnet corrector located before the bending magnet in FFTB was used to move the beam centroid in both the X and Y direction. This manipulation caused synchrotron radiation and produced the displacements of the "tail" from the "head" on the fluorescence image, noted as δx and δy in Fig. 5.6. Figure 5.7 demonstrates a series of X-ray fluorescence images as the beam was moved in X and Y directions respectively with the magnet corrector. Therefore the position of the beam cen-

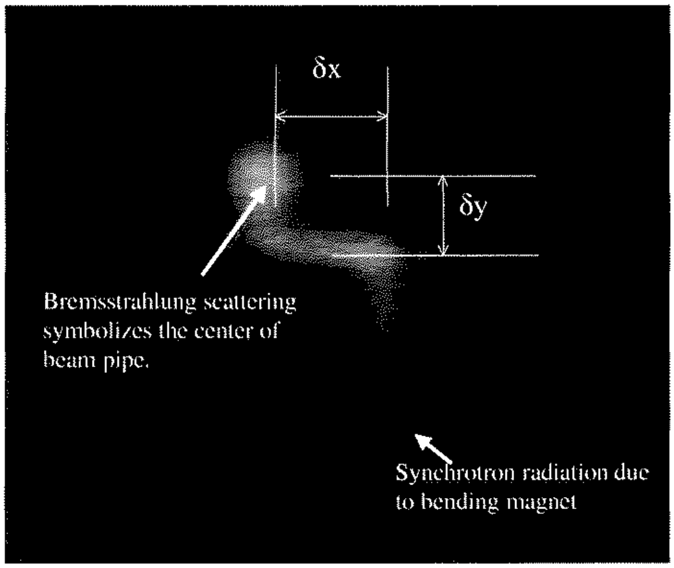

Figure 5.6: A typical fluorescence image with a "tadpole" shape recorded by the CCD camera.

troid can be traced by the displacements of δx and δy in the X-ray images. We

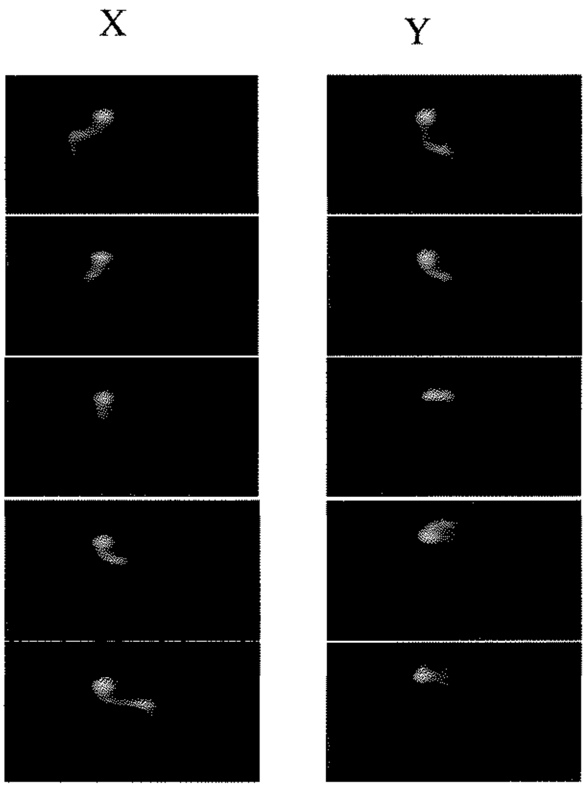

Figure 5.7: A series of X-ray fluorescence images showing the electron beam displacements in X (Left) and Y (Right) directions.

measured the beam centroids with a downstream BPM and plotted against the displacements of δx and δy in X-ray images, as shown in Fig. 5.8. The correlation between them is very good.

5.3.3 Experimental Results of X-ray Emission from Betatron Motion

The experiment to detect X-ray emission from betatron motion in a plasma was carried out at the Stanford Linear Accelerator Center (SLAC) using the

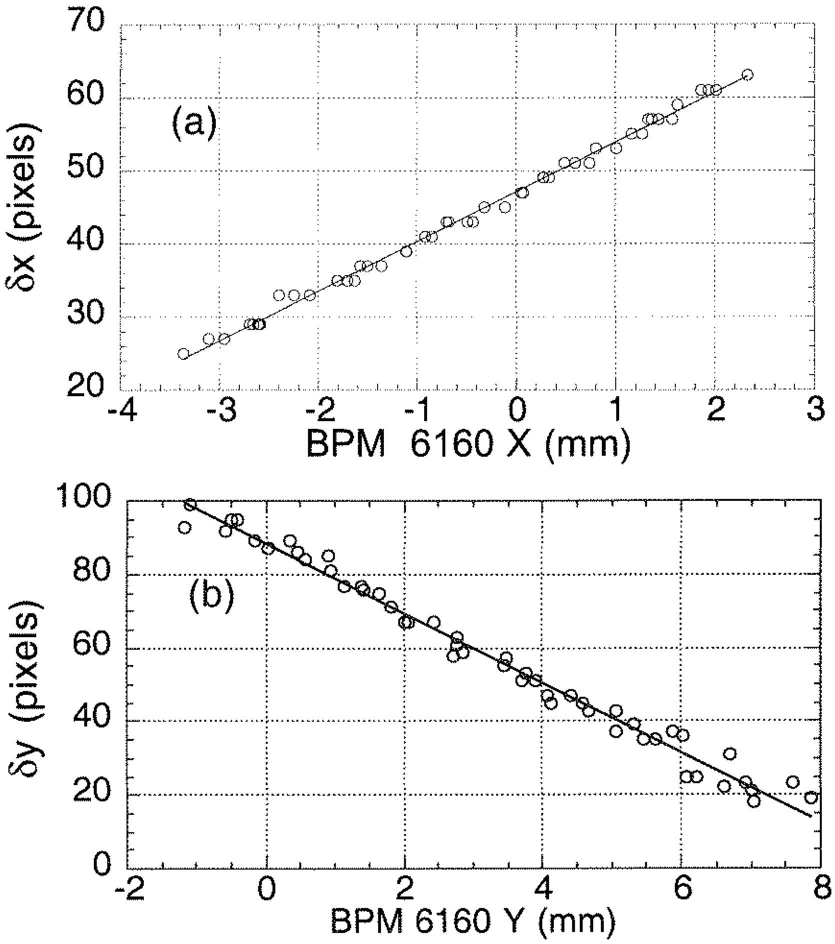

Figure 5.8: The correlation plot between the displacements of beam centroids measured with the BPM and the displacements δx and δy in the fluorescence images. The lines are drawn to guide the eye.

Final Focus Test Beam (FFTB). The 28.5 GeV SLAC beam containing typically 1.8×10^{10} electrons per bunch (with $\sigma_r = 40\ \mu m$ and a longitudinal bunch length $\sigma_z = 0.7\ mm$) was focussed near the entrance of a lithium plasma of length $L_p = 1.4\ m$ produced by single photon ionization of a lithium-vapor column by an ArF laser[20]. Therefore the plasma density, in the optically thin limit, is simply proportional to the total laser energy absorbed by the plasma. The plasma density was thus varied by varying the laser energy. The plasma density deduced from the UV absorption measurements was calibrated against a more direct measurement of plasma density using CO_2 interferometry in an offline experiment[37]. The typical plasma diameter was 2 mm. A schematic of the experimental set-up is shown (not to scale) in Fig. 5.9. The electron beam had a small and approximately linear "head-to-tail" tilt when it entered the plasma [54]. Over the range of plasma densities used in this experiment, the peak beam density

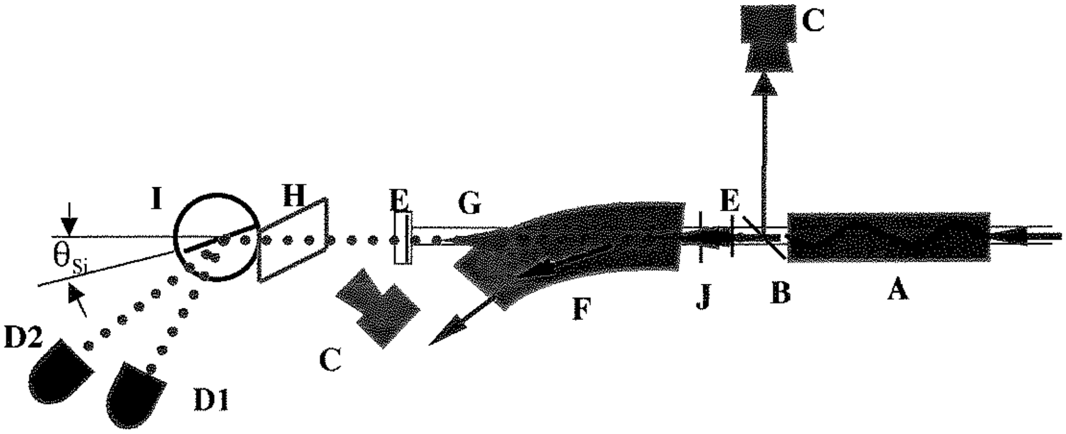

Figure 5.9: Schematic of the experimental set-up. A bend magnet separates the electrons (solid red line) from the photons (dashed blue line) after the plasma wiggler. Key: A-lithium plasma source; B-OTR Ti foil; C-CCD cameras; D1-SBD receiving Thomson scattered X-rays; D2-SBD receiving Bragg scattered X-rays; E-Beryllium vacuum windows; F-bend magnet; G-photon beam line; H-fluorescent screen, I-silicon (111) crystal on a rotation stage at angle θ_{Si}, J-beam position monitor.

was larger than the plasma density. In this so-called underdense plasma regime, the head of the beam expels the plasma electrons creating an ion channel. This ion channel in turn exerts a transversely-linear and longitudinally-uniform focusing gradient on the main body of the electron beam. At the highest density of $1.7 \times 10^{14}\ cm^{-3}$, the magnitude of this force, about 50 MG/m, is enough to cause the beam to focus from the initial 40 μm to $< 5\ \mu m$ after propagating only $\sim L_p/6$ inside the plasma. The electrons in the beam overshoot this focus (cross the axis) and the beam radius returns to the initial size after propagating $\sim L_p/3$. Thus the beam undergoes about three envelope oscillations ($k_\beta L_p \sim 3\pi$)within the full length of the plasma, whereas the individual electrons execute 1.5 betatron oscillations, crossing the axis at integer π values of $k_\beta L_p$.

These betatron oscillations were simultaneously measured in two ways. The first measurement was of the beam size 1 meter downstream of the plasma as observed from optical transition radiation (OTR) [50]. This showed that as the plasma density was raised slowly beginning from $1 \times 10^{13}\ cm^{-3}$, the radius of the beam on the OTR foil would at first increase (over-focused) but then drop back down to approximately the plasma-off size when $k_\beta(n)L_p \sim \pi$. This envelope oscillation continued [53] as n was further increased, giving a beam-size minimum at $k_\beta L_p \sim 2\pi$ and another at $k_\beta L_p \sim 3\pi$ when $n \sim 1.7 \times 10^{14}\ cm^{-3}$. These values of n where $k_\beta L_p \sim m\pi$ ($m = 1, 2, 3$) are called "transparency points" since the beam spot size coming out is similar to the beam size at the same location without the plasma. In the second, concurrent measurement shown in Fig. 5.10(a), the center of mass (centroid) of the beam was measured (using a beam position monitor placed $2.6m$ from the plasma exit) as n was increased. Due to the initial tilt on the beam, the centroid of the bunch had a small transverse offset from the axis of the ion channel, since it is the head of the bunch that defines this axis. Consequently, the motion of the centroid behaves much like that of a single electron which starts at some offset from the ion channel axis, i.e., the centroid crosses the axis at $k_\beta L_p \sim m\pi (m = 1, 2, 3)$. This is indeed what is observed in Fig. 5.10(a) where the centroid displacement returns to its initial offset ($\sim$ 0) at the same values of n where the beam size had a minimum [53] (the arrows labeled 1,2, and 3 in Fig. 5.10(a)). Both the envelope and centroid oscillations agree reasonably well with the theoretical predictions (solid line in Fig. 5.10(a)) based on the beam envelope equation for beam propagation in a uniform ion channel [53][26] up to a density of about $1.7 \times 10^{14}\ cm^{-3}$. In fact, the absolute plasma density shown in Figs 5.10(a) and (b) derived from this theoretical fit is close to that inferred from absolute absorption of the ionizing laser beam.

The electron beam exiting the plasma was bent away using a $5.2m$ long dipole magnet located three meters from the exit of the plasma. The X-rays emitted by the undulating electrons were recorded 40 m downstream of the plasma after traversing the 25 μm thick titanium OTR foil at 45^o with respect to the beam axis and two 75 μm thick beryllium windows. The X-rays were reflected by a $1mm$ thick silicon (111) crystal and detected using two 1 mm thick silicon surface barrier detectors (SBD). One of the SBDs (D2) could be placed to precisely receive the Bragg-reflected X-rays, while the other (D1) was placed in the same plane but at a mismatched angle to receive Thomson-scattered photons from the crystal. Both detectors were well shielded using lead to decrease X-ray noise that is incident from directions other than the photon beam line. The signal on the SBDs is due to photons in the $5 \sim 30\ KeV$ energy range because photons with energies less than 5 KeV are mainly attenuated by the Ti foil while those with energies greater than 30 KeV transmitted through the detector.

Figure 5.10(b) shows the integrated X-ray power (arbitrary units) in the energy range 5 KeV to 30 KeV (red dots) as a function of plasma density using

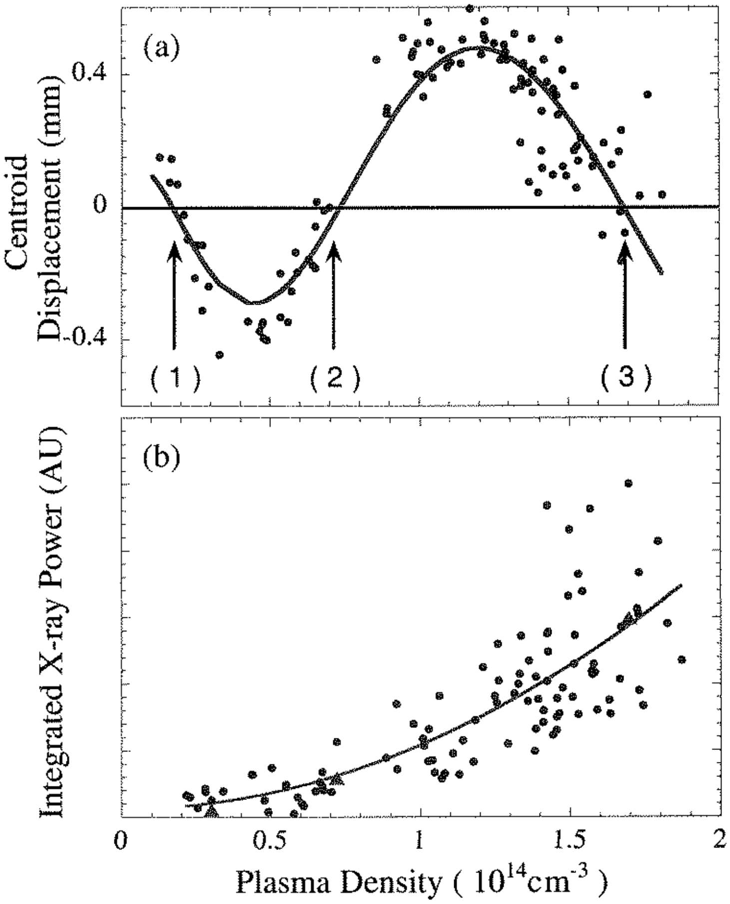

Figure 5.10: (a) The predicted (solid line) and measured displacement of the beam centroid as a function of plasma density. (b) The estimated (triangles) and the measured (dots) X-ray energy in the $5 \sim 30 kev$ range as a function of plasma density. The solid line is the quadratic fit to the experimental data.

detector D1 that received Thomson-scattered X-rays. Also shown are the relative values (blue triangles) of the theoretically expected X-ray energy yield by numerically integrating the expression for the Lienard-Wiechert potential [23][25] over all solid angles within the $5 \sim 30\ KeV$ photon energy range at the transparency points, and taking into account corrections for the transmission function of the metal foils, and the frequency response of the atomic scattering factor of silicon atoms. The details of this calculation are presented in Chapter 2 and in [62]. At low densities ($n < 1.0 \times 10^{14}\ cm^{-3}$) the shot-to-shot variation in the X-ray energy is relatively small compared to that at higher densities. The fluctuations at higher densities are caused by the n^2-dependence of the X-ray power and the fact that the actual plasma density can fluctuate ±15% about the deduced plasma density due to experimental limitations such as spatial fluctuations in the ionizing UV profile. The agreement between theory and experiment is good. Also shown is a curve representing the expected quadratic dependence of the X-ray energy on plasma density. Even though both the measurement and the numerical integration are over the $5 \sim 30\ KeV$ photon-energy range, they match well with the expression for total energy-yield over all frequencies which scales as n^2.

We have measured the absolute value of photon numbers around the $m = 3$ transparency point ($n = 1.5 \sim 1.8 \times 10^{14} cm^{-3}$) using the Bragg scattering technique. As can be seen from the inset to Fig. 5.11, as the Si crystal is rotated the signal received by detector D2 shows an enhanced peak at $\hbar\omega \sim 14.2\ keV$ when the exact Bragg condition is satisfied at $\theta_{Si} \sim 8^{\circ}$. The expected bandwidth of the Bragg signal at the $m = 3$ transparency point is determined by the range of incident angles within the X-ray beam. As stated before, this range is given by $\Delta\theta \sim K/\gamma$ which for $m = 3$, $\sigma_r = 40\mu m$, and $K = 16.8$ is $\Delta\theta \sim 0.29 mrad$. From $\Delta\omega/\omega = -\Delta\lambda/\lambda = -\Delta\theta/\tan\theta$ we have $\Delta\omega/\omega = 0.002$. Detector D2 subtends an angle off the Si crystal of $\sim 10 mrad >> \Delta\theta$ and thus easily captures this bandwidth.

We acquired two sets of data while varying the plasma density by $\sim \pm 10\%$ around the third transparency point. In the first set of data both D1 and D2 were not at the Bragg angle and therefore received radiation in the same broadband photon energy range. The signals on the two detectors for this data set are plotted against each other as triangles in Fig. 5.11, essentially showing the relative sensitivities of the two detector systems. The crystal was then rotated to $\theta_{Si} \sim 8^o$ such that D2 received, in addition to the broadband radiation, Bragg scattered photons at $14.2 KeV$ while D1 still received only the broadband radiation. A plot of the signals on D1 vs. D2 (rectangles in Fig. 5.11)shows that for the same range of signals on D1, D2 received $\sim 2.1\times$ more signal when at Bragg angle. We attribute this $\sim 250\ mV$ average additional signal to the 14.2 KeV Bragg-scattered photons. After taking into account the detector circuit response, the photon-to-electron conversion efficiency of the SBD and the transmission loss of the system, we estimate the number of 14.2 KeV photons to be 6×10^5. This number is to be taken as a lower bound as we have assumed a Bragg reflectivity of unity.

We now compare the measured number of photons at 14.2 KeV with a theoretical estimate. The number of photons in the above mentioned energy bin can be estimated by approximating the radiation spectrum of our plasma wiggler, W, with that of a bending magnet, B. We thus have $[\frac{dN_{ph}}{d\psi}]_W = m[\frac{dN_{ph}}{d\psi}]_B = m \cdot C_\psi \cdot I \cdot E \cdot \frac{\Delta\omega}{\omega} \cdot S(\omega/\omega_c)$, where $C_\psi = 3.967 \times 10^{16} photons/(sec \cdot mrad \cdot Amp \cdot GeV)$, and $S(\omega/\omega_c) = \frac{9\sqrt{3}\omega}{8\pi\omega_c} \int_{\frac{\omega}{\omega_c}}^{\infty} K_{5/3}(x)dx$ is the so-called universal function[27]. In the above expression, I is the average beam current within an electron bunch, E is the beam electron energy, m is the integral number of the betatron periods ($m = 3$), ψ is the sweep angle ($\sim K/\gamma$), ω satisfies $\hbar\omega \sim 14.2\ KeV$, and $\Delta\omega/\omega$ is is the normalized bandwidth (= 0.002). Based on the above numbers, we obtain $N_{ph} \sim 3.0 \times 10^6$ at 14.2 ± 0.014 KeV. This estimate is about five times larger than the measured number.

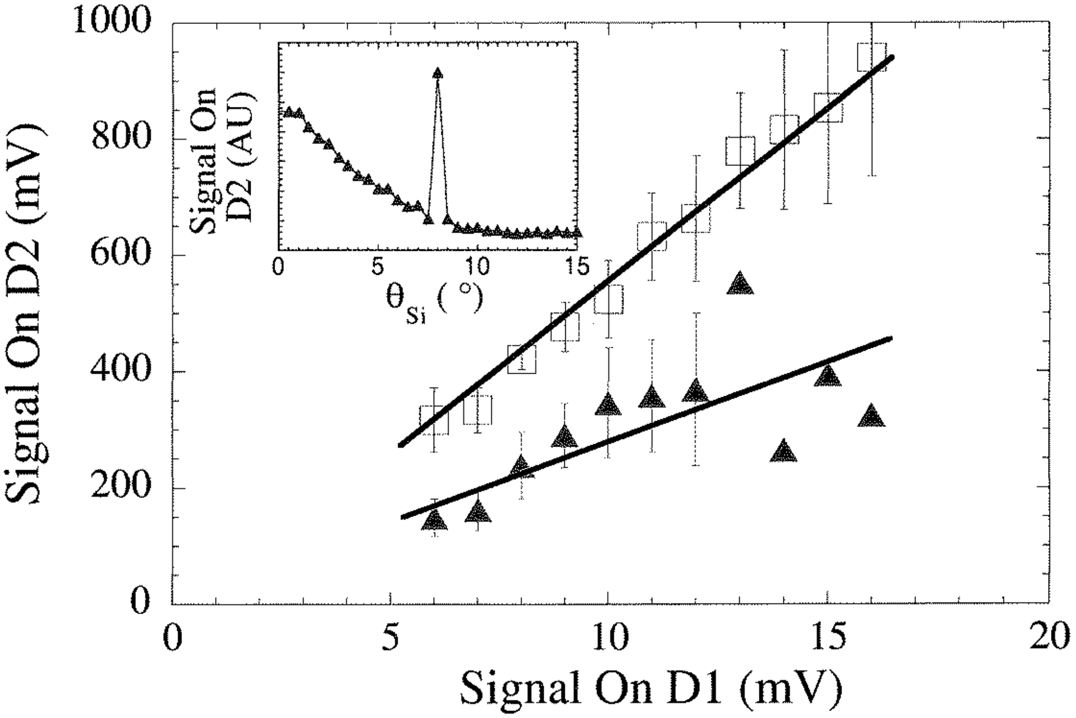

Figure 5.11: The correlation of signals on detector D2 vs. detector D1. The inset shows clear Bragg peak at 8° on D2 as θ_{Si} is varied (curve taken with plasma off and without the Ti OTR foil in the beam line).

Using the 14.2 KeV photon yield deduced at $m = 3$ and a radiation angle of $\sim K/\gamma_b$, we can estimate the photon integrated-intensity[25] to be 4.5×10^{17} $photons/(sec \cdot mrad^2 \cdot 0.1\% bandwidth)$. The effective source size S of the 14.2 KeV radiation can be approximated as $S = \pi(\sigma_r^2 + \frac{1}{4}((\epsilon/\sigma_r)^2 + (0.6K/\gamma_b)^2 L_p^2) \sim 0.06$ mm^2 where ϵ is the geometrical emittance of the beam. We therefore estimate the peak spectral brightness to be about 7×10^{18} $photons/(sec \cdot mrad^2 \cdot mm^2 \cdot 0.1\% bandwidth)$.

Figures 5.12(a) and (b) are typical X-ray images recorded by the CCD camera looking at the fluorescer with (a) plasma off and (b) plasma on. X-rays from betatron motion are embeded in the area illustrated with a rectangle in the figure. The curves plotted at the left side of the images were the sum of the fluorescence intensities along Y axis. They clearly show that there is more fluorescence in (b) than in (a). An experiment was done to measure the variations of the the fluorescent intensities inside the central area (bounded by the rectangle) as a function of plasma densities at different transparent conditions. A typical measured result is shown in Fig. 5.13. Although the figure demonstrates that the fluorescent yield grew with the increase of plasma density, it was not proportional to the square of plasma densities as might be expected from theory. This was probably due to the frequency response of the fluorescer.

Figure 5.14 shows a processed image of the fluorescence produced by the X-rays from betatron motion in the plasma ion column at the first transparency point ($m = 1$), while Fig. 5.15 is the 3-D visualization of the processed image. To obtain this image, a plasma-off image was subtracted from a plasma-on image. With the plasma off, the X-rays producing the fluorescence are generated by synchrotron radiation due to all the multipole magnets (not shown in Fig. 5.9) upstream of the dipole bend magnet, bremsstrahlung from the metallic foils, and synchrotron radiation due to the dipole bend magnet used to separate the photons from the electrons. With the plasma on, the fluorescence is generated by X-rays from all the above mentioned sources and X-rays due to betatron motion in the plasma. Because of the small initial tilt on the beam, the beam exits the plasma with a small deflection angle. This makes perfect subtraction of the contribution of the downstream dipole bend radiation impossible. Thus Fig. 5.14 shows a round spot corresponding to the "betatron" X-rays and a vertical tail that is left over from subtraction of this misaligned dipole bend radiation. The FWHM of

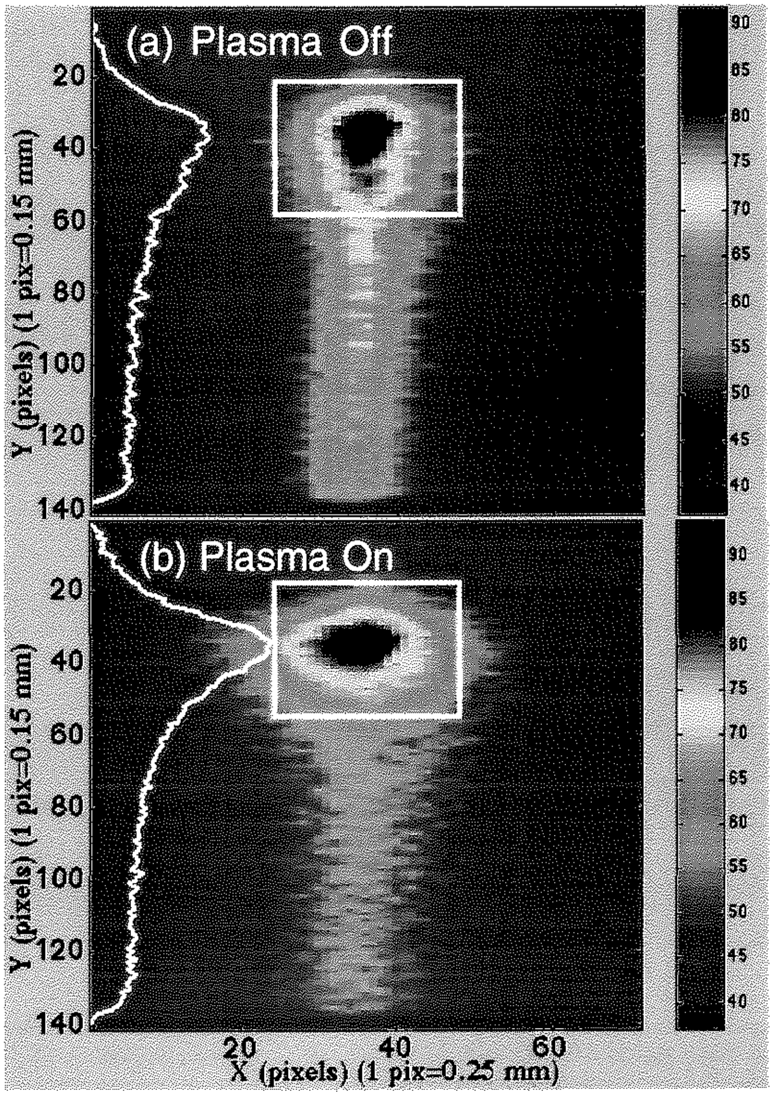

Figure 5.12: X-ray fluorescence images with a false color as (a) plasma off and (b) plasma on.

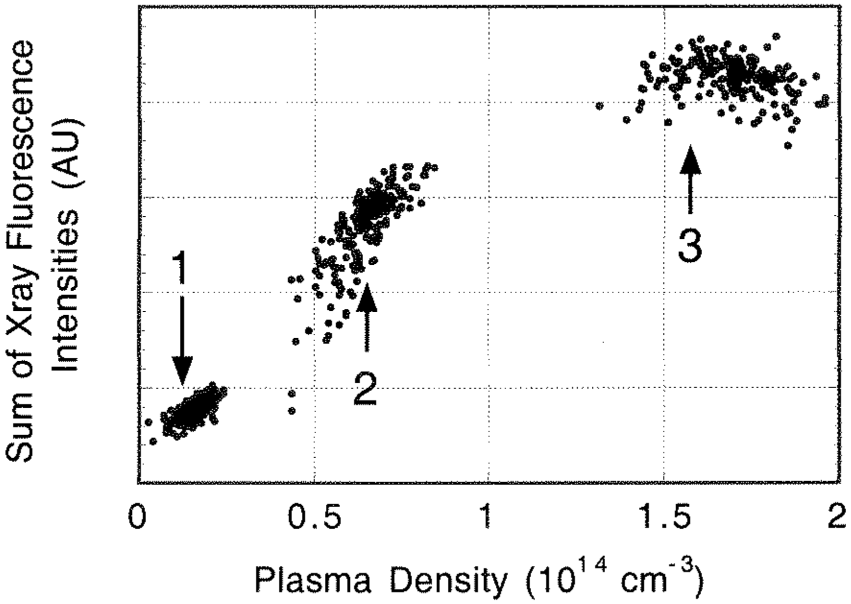

Figure 5.13: The relative values of the sum of X-ray fluorescences as a function of plasma densities. The marks in the figure imply the transparent points where the plasma density satisfies $\omega_\beta L/c \approx m\pi$, with m=1,2,3 ....

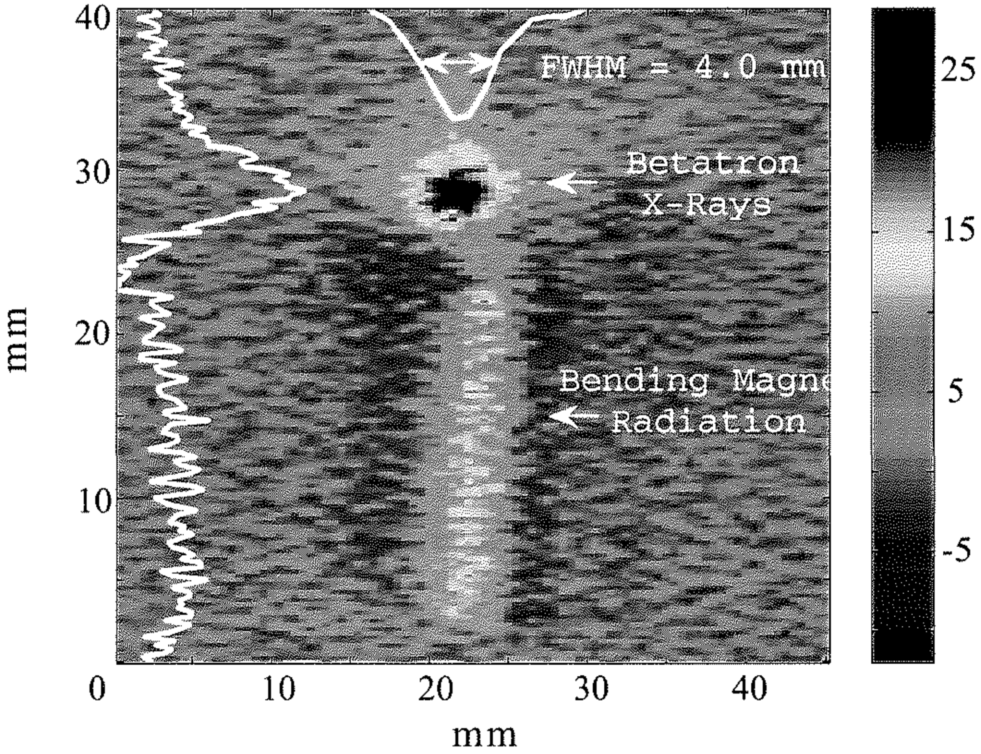

Figure 5.14: Processed image produced on the fluorescent screen as recorded by the CCD camera showing the "betatron" X-rays produced by the plasma (circle at the top) and a vertical stripe of remnant synchrotron radiation produced by the bend dipole magnet.

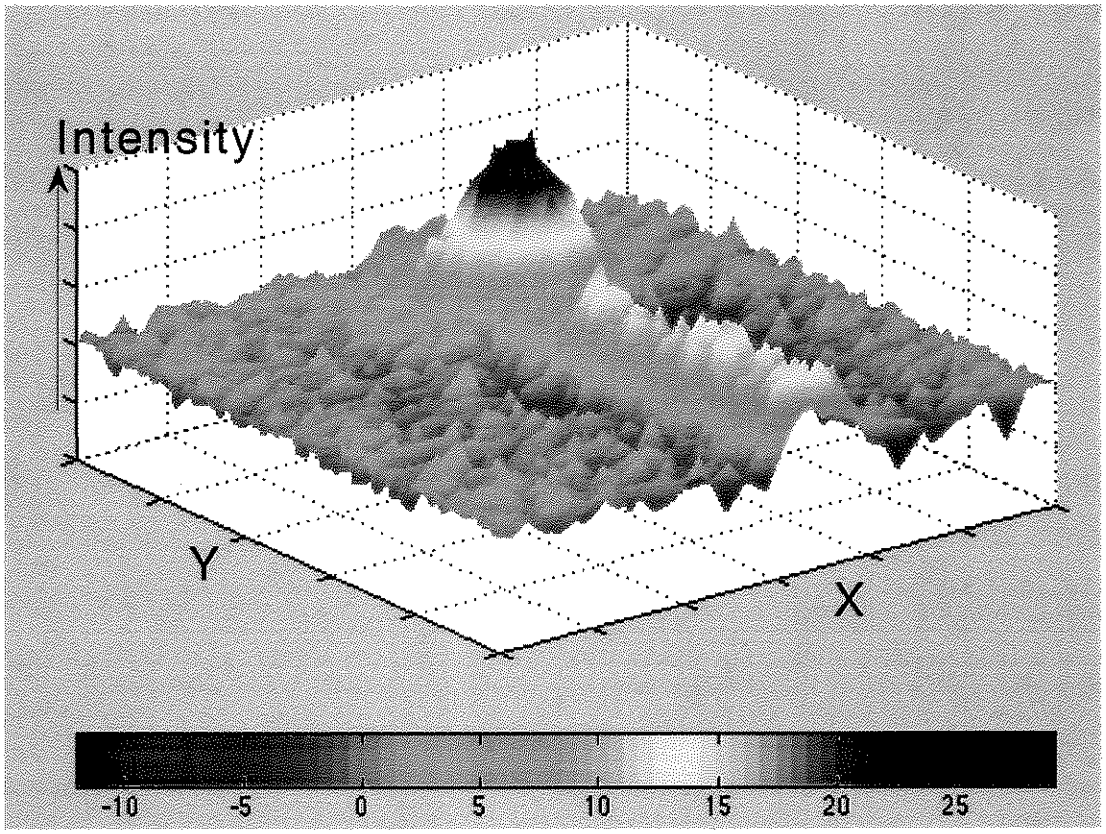

Figure 5.15: 3-D visualization of the the processed image shown in Fig. 5.14.

the plasma "betatron X-ray" fluorescence image is approximately 4 *mm* which gives a full-beam divergence angle of $10^{-4} radian$. The theoretical estimate for the angle is roughly $K/\gamma_b \sim 0.9 \times 10^{-4}$ for the present condition. Thus the measured angle is in good agreement with the theory, particularly since the fluorescent image is dominated by lower energy X-ray photons. These results are the first observation of plasma betatron radiation in the X-ray region to our knowledge.

We have shown that an ion channel induced by the beam can wiggle beam electrons to produce X-radiation. Such a plasma wiggler comprising of only a plasma cell offers simplicity of construction, flexibility in undulator wavelength, and potential savings of cost over its magnetic wiggler counterpart in future generation of light sources.

5.4 Summary

In this chapter, I have detailed the main experimental findings of this thesis: X-ray radiation from electron betatron motion in a plasma wiggler. I have introduced the experimental apparatus used in X-ray diagnosis. These are followed by experimental results, such as the relative values of the radiation power as a function of plasma density, its radiation angle, and a rough estimation of photon flux and brightness at a specific photon energy.

Due to the limitation of the experimental conditions, the details of the spectrum as well as the cut-off energy of the X-ray radiation were not diagnosed. A double-crystal spectrometer can be used to measure the spectrum in the 1-15 KeV range for the next project.

CHAPTER 6

The Challenge to an Ion Channel Laser

6.1 Introduction

Spontaneous radiation produced by a relativistic electron beam(REB) traversing an undulator will lead to stimulated emission if the radiation can feedback on the beam and create a beam-photon instability. The feedback of photons can be realized by building an optical cavity, which is often used in the microwave and the visible regions of the spectrum. Such a cavity, however, is very difficult to build in the X-ray spectral region, since the reflectivity of a mirror decreases dramatically in this region. Instead, the amplification of X-ray radiation can be realized via self-amplified spontaneous emission (SASE) [11]. In an FEL SASE process, the ponderomotive force due to the beat between the electromagnetic radiation field and the undulator magnetic field pushes the beam electrons so that some electrons are accelerated and the others decelerated, depending on their phase relations with the force. This leads to a self-bunching of the beam and consequently the amplification of the radiation. Since the amplification is produced in a single pass of a high density REB through a long undulator, it eliminates the need for an optical cavity. But the requirements on the electron beam's peak current, emittance, and the energy spread are more stringent than in other schemes. The schematic of a SASE scheme is illustrated in Fig. 6.1.

An Ion Channel Laser(ICL) is a new kind of free electron laser (FEL), in

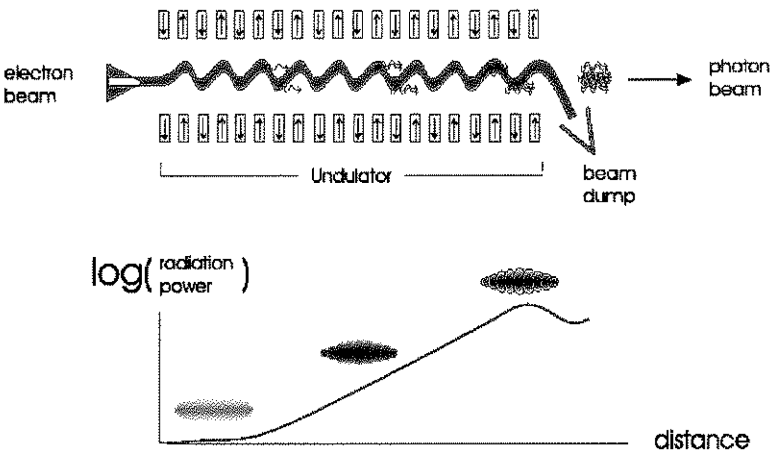

Figure 6.1: (Above) The schematic of a free electron laser operating in the SASE mode. (Below) The plot shows that the radiation power is exponentially growing while the electron beam is being bunched.

which an electrostatic field due to a uniform ion column of charge, instead of a magnetic field, is employed to wiggle an REB [7]. The original ICL schematic is drawn as Fig 6.2. As an REB with the Lorentz factor γ traverses a preformed ion column, the electro-static field supported by the ion column will force a beam electron to swing up and down transversely about the axis of the ion column with the betatron frequency ω_β. The betatron frequency is equal to $\omega_p/\sqrt{2\gamma}$ if the ion column is cylindrical symmetric, or $\omega_p/\sqrt{\gamma}$ if the column is slab symmetric, with ω_p the plasma frequency. An electron in the betatron motion will radiate spontaneously. The electron betatron motion and a radiation field can be coupled which leads to coherent radiation when the angular frequency ω and the wavenumber k_z satisfy the resonance condition

$$\omega - k_z v_z = \omega_\beta, \tag{6.1}$$

where v_z is the beam velocity. The fundamental resonance frequency, which follows from Eq. 2.19 is

$$\omega_r = \frac{2\gamma^2\omega_\beta}{(1+K^2/2)} \tag{6.2}$$

where K is the wiggler strength as described in Eq. 2.27. An ensemble of electrons, in an ICL, tend to be micro-bunched due to a beat between the radiation field with frequency ω and the electrons' betatron motion, just as in a conventional FEL. Micro-bunched electrons emit photons in phase thus coherently producing a larger radiation intensity. The larger intensity leads to more bunching and a much larger intensity. Consequently this feedback process leads to an exponential growth of the radiation.

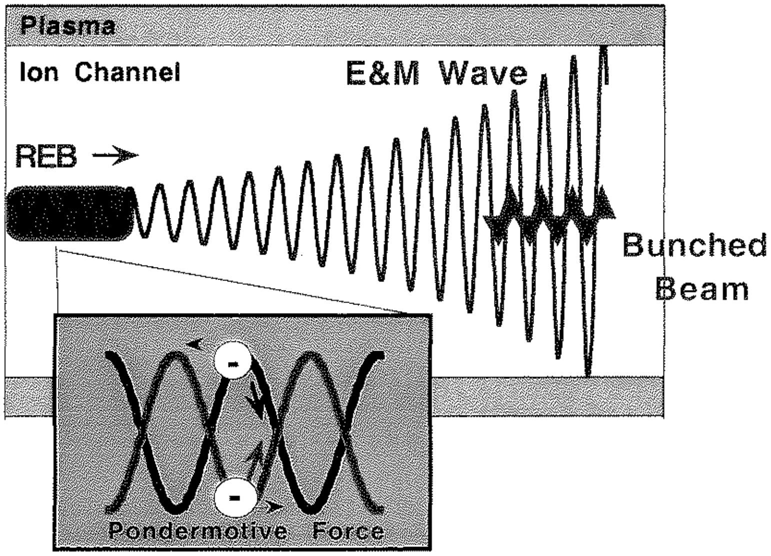

Figure 6.2: An electromagnetic wave propagates with an ion-focused relativistic electron beam. Beam electrons oscillate transversely and are micro-bunched axially by the ponderomotive force.

It is interesting to note the differences that lead to micro-bunching in an ICL and an FEL. In an FEL, all beam electrons oscillate at a given axial location in phase, and are separated with the interval of the radiation wavelength, which is $2\pi/k_z$, in the longitudinal direction. Whereas in an ICL, the betatron motion of an electron at one side of the axis of the ion channel has a π phase difference with one at the opposite side of the axis. Although those electrons at one side of the axis are bunched in the longitudinal direction as in an FEL, they have π phase difference with those at the opposite side of the axis, as illustrated in Fig. 6.2. This issue will be addressed in later sections of this chapter.

D. H. Whittum *et al.*[7] derived the exponential gain length of an ICL

$$L_g = \frac{\lambda_\beta}{2\sqrt{3}\pi\rho} \tag{6.3}$$

with

$$\rho \approx (\frac{I}{32\gamma I_A})^{1/3}, \tag{6.4}$$

where $I_A = mc^3/e \approx 17kA$, and $\lambda_\beta = 2\pi/\omega_\beta = 2\pi/k_\beta$. This growth rate is the same with that in an FEL[63] if we equate k_β in an ICL with the wiggler wave number k_u in an FEL. K. R. Chen *et al.* [64] pointed out that the growth rate would be smaller if so-called transverse bunching is taken into account. The transverse bunching has been analyzed extensively in earlier free electron devices such as the cyclotron autoresonant maser [65] [66] [67]. It can be understood intuitively as follows. Each electron oscillates with a slightly different ω_β at each transverse position due to the relativistic mass effect, referring to Eq. 2.18. These electrons tend to bunch together transversely because of the resonance condition, Eq. 6.1. The transverse bunching doesn't happen in an FEL, since in an FEL the electron wiggler wave number k_β is independent of the transverse positions of electrons. The transverse bunching mixes with the longitudinal bunching and complicates the bunching mechanism in an ICL . However,D. H. Whittum *et al.*[7] argued that the longitudinal bunching dominates over the transverse bunching in the fast wave limit($\omega \sim k_z \cdot c$).

Compared with an FEL, an ICL has the advantage in that no external magnets are required. The ICL also provides much more flexibility in tuning the radiation frequency since it is easier to change the plasma density than it is to change the distances between magnet poles in an FEL. Working in the low frequency spectral region, the ion channel can also provide an effective waveguiding to maximize the interaction length between the radiation field and the electron beam.

However, an ICL imposes a much more stringent requirement on the beam emittance, when compared with an FEL working in the SASE (self-amplified spontaneous emission) mode of operation. This disadvantage is intrinsically due to the fact that the wiggler strength K of an ICL, in view of Eq. 2.27, is a function of the transverse position of each electron in the beam. A general requirement in an FEL is that the normalized energy spread, $\Delta\gamma/\gamma$, be small compared to the so called Pierce or the gain parameter ρ, *i.e.*, $\Delta\gamma/\gamma < \rho$. In an ICL, this limits the radius of the beam electrons r_0 as follows,

$$\frac{\Delta\gamma}{\gamma} \approx \frac{(r_0 k_\beta)^2}{4} < \rho. \tag{6.5}$$

For a matched beam[1], Eq. 6.5 implies that the beam emittance in an ICL must satisfy

$$\epsilon < \frac{4\rho\lambda}{\pi}. \tag{6.8}$$

Whereas in an FEL, the emittance requirement is that $\epsilon_{FEL} < \lambda/(4\pi)$ where λ is the radiation wavelength. Therefore the beam emittance has to be much smaller in an ICL than that in an FEL since typically the Pierce parameter is very small, $\rho << 1$.

As in any other plasma related devices, the desired instability in an ICL must

---

[1] The REB is matched in an ICL when the ion focused force is balanced by the outward force due to beam emittance [26], i.e.,

$$\frac{d\vec{P}_r}{dt} = \vec{F}_{in} - \vec{F}_{out} = -\frac{m_e\omega_p^2}{2}\vec{r} + \frac{m_e c^2 \epsilon^2}{\beta_b^2 r^4}\vec{r} = 0, \tag{6.6}$$

where ϵ is the emittance of the REB. The corresponding matched radius of the beam is given by

$$r_0 = (\frac{\epsilon}{k_\beta})^{1/2}. \tag{6.7}$$

compete with other undesired instabilities. The beam-field interaction which is the essential mechanism in realizing stimulated amplification of radiation in an ICL, may be hindered by the electron [28] and ion hose instabilities [15]. A longitudinal wake field along the ion channel, which is due to plasma electrons rushing back to the axis after being blown-out, may affect the phase relations among beam electrons. It is impossible to consider these important effects altogether analytically. The best way to fully analyze the capability of the realization of an ICL is to simulate beam and plasma electron motions with a self-consistent particle-in-cell code. This is beyond the scope of the thesis. Instead, in this chapter, I will analyze, in both theory and computer simulation, only one phenomena: electron micro-bunching in a preformed ion-channel due to the beat between electron betatron motion and the electromagnetic wave. Normalized units which are used throughout the later sections will be addressed briefly in following section. It is assumed that an ion channel is preformed and the process is seeded by a small background radiation field. By assuming this, a simplified theory of electron-microbunching will be given in section 6.3. The PIC (particle in cell) code OSIRIS [68] is used to simulate the bunching phenomena in a 2-D slab coordinate system. The big challenge to simulating an ICL is the disparity in time scale between the betatron period and the radiation period. In section 6.4, I will estimate the computer running-time required by a simulation run on one node. Other challenges in the simulation, such as numerical instabilities, self-space-charge effects, etc. will be addressed briefly also in this section. In section 6.5, I will present preliminary simulation results of electron micro-bunching. I will summarize this chapter in the last section.

6.2 Normalized Units

Normalized units are used throughout the following analysis unless otherwise specified. In particular, velocity is normalized to the speed of light c, density is normalized to the plasma density n_p, charge is normalized to the electron charge e , and the mass is normalized to the electron mass m_e. It follows that if the plasma frequency is ω_p, then the unit of time is ω_p^{-1} and the unit of distance is c/ω_p. The units of other physical parameters can be derived based on above. For example, the electro-magnetic field is normalized to $m_e c\omega_p/e$, and the momentum is to $m_e c$.

6.3 Microbunching Mechanism

In the following sections, a slab geometry is adopted in both the theory and the simulations . In this slab geometry, an ion channel is assumed to be preformed, and the corresponding electrostatic field due to the ion-channel is

$$\vec{E_\beta} = A_\beta x\hat{x} \tag{6.9}$$

where $A_\beta = 4\pi n_i e$ (in cgs. units) and n_i is the ion density. It is assumed that the ion density is equal to the plasma density, i.e., $n_i = 1$, for simplicity. We also assume that the radiation field starts as a plane electromagnetic wave with $\vec{E}$ in the $\hat{x}$ direction and with its magnitude $E_x = Ecos(\omega t - kz)$. The associated magnetic field has $\vec{B}$ in the $\hat{y}$ direction and a magnitude $B_y = Bcos(\omega t - kz)$, where ω is the frequency and k is the wavenumber. $B_y = (ck/\omega)E_x = E_x/v_{ph}$ according to Maxwell's equation. We assume $E_\beta >> E$ so that we are in the small signal approximation.

At $t = 0$, an electron bunch with the Lorentz factor γ_0 and velocity v_z is sent into the preformed ion channel along the axial direction, i.e., $\hat{z}$. These electrons are initially rigidly displaced a distance x_0 away from the axis of the channel and have no transverse momentum. As a beam electron interacts with the ion channel and the electromagnetic wave, its momentum and energy are governed by the following equations. The force in x direction satisfies

$$F_x = \frac{d(\gamma v_x)}{dt} = -E_\beta - E_x + v_z B_y. \tag{6.10}$$

The force in z direction satisfies

$$F_z = \frac{d(\gamma v_z)}{dt} = -v_x B_y. \tag{6.11}$$

The variations of its energy satisfies

$$\frac{d\gamma}{dt} = -E_x v_x - E_\beta v_x. \tag{6.12}$$

In writing the above equations, the variations of the momentum and the energy of the beam electron due to space-charge effects are ignored. In other words, we limit the following discussion in the so called "Compton" regime [69].

In the small signal approximation ($E_\beta >> E_0$), the zeroth order orbit of a beam electron is:

$$\gamma = \gamma_0;\ v_x = 0;\ v_z = v_{z0};\ z = v_{z0}t + z_0. \tag{6.13}$$

The first order part of Eq. 6.10, based on the zero order results, is

$$\frac{d\gamma v_x}{dt} = \gamma\frac{dv_x}{dt} + v_x\frac{d\gamma}{dt} \approx \gamma_0\frac{dv_x}{dt} = \gamma_0\frac{d^2x}{dt^2} = E_\beta. \tag{6.14}$$

where $\gamma_0 dv_x/dt >> v_x d\gamma_0/dt$ is assumed. In view of Eq. 6.9, the first order results for x and v_x are

$$x = x_0 cos(\omega_\beta t + \phi_0);\ v_x = -x_0\omega_\beta sin(\omega_\beta t + \phi_0), \tag{6.15}$$

with ω_β satisfying

$$\omega_\beta = 1/\sqrt{\gamma}. \tag{6.16}$$

The first order equation for γ, based on Eq. 6.12, is

$$\frac{d\gamma}{dt} = -E_\beta v_x = \frac{x_0^2}{4}(1 - cos(2(\omega_\beta t + \phi_0))), \tag{6.17}$$

where equations 6.15 and 6.9 have been applied. The first order equation for v_z, based on Equations 6.11 and 6.12,

$$\gamma_0 \frac{dv_z}{dt} = -v_x B_y - v_{z0}\frac{d\gamma}{dt} = -v_x B_y + v_{z0}(E_x v_x + E_\beta v_x). \tag{6.18}$$

Now it is assumed that the electron with betatron motion characterized by ω_β is resonant with the electro-magnetic wave and remains in phase for many betatron periods; that is $\omega - kv_z - \omega_\beta \sim 0$ and $\omega_\beta t >> 1$. An average on Eq. 6.18 is performed over the period $2\pi/\omega_\beta$, and

$$\langle\frac{dv_z}{dt}\rangle = -\frac{1}{\gamma_0}(\frac{1}{v_{ph}} - v_{z0})\langle v_x E_x\rangle \approx -\frac{sin(kz_0)}{2\gamma_0^3}x_0\omega_\beta E \tag{6.19}$$

In doing so, $\langle v_x E_\beta\rangle \propto \langle v_x x\rangle \propto \langle cos(\omega_\beta t + \phi_0) sin(\omega_\beta t + \phi_0)\rangle = 0$ has been applied. From conservation of charge, the beam density is given by

$$\frac{\partial n}{\partial t} = -\frac{\partial(nv_z)}{\partial z}. \tag{6.20}$$

The perturbed beam density, in first order, is therefore

$$\frac{\partial n_1}{\partial t} = -\frac{\partial n_1 v_{z0} + n_0 \partial v_{z1}}{\partial z}, \tag{6.21}$$

or

$$\frac{dn_1}{dt} = -n_0\frac{\partial v_{z1}}{\partial z}. \tag{6.22}$$

Taking the convective time derivative and averaging both sides of Eq. 6.22 over a betatron period, and employing Eq. 6.19 yields

$$\frac{d^2\langle n_1\rangle}{dt^2} = -\frac{sin(kz_0)}{2\gamma_0^3}n_0 k x_0 \omega_\beta E. \tag{6.23}$$

Therefore, the evolution of the perturbed beam density with time satisfies

$$\frac{\langle n_1 \rangle}{n_0} = -\frac{sin(kz_0)}{4\gamma_0^3} kx_0\omega_\beta Et^2, \tag{6.24}$$

and the maximized perturbed beam density along the beam satisfies

$$\frac{\langle n_1 \rangle}{n_0} = -\frac{kx_0\omega_\beta Et^2}{4\gamma_0^3}. \tag{6.25}$$

In summary of this section, the evolution in time of the perturbed beam density in small signal approximation has been derived. The growth of this perturbation is due to the beat between the electron betatron motion and the ponderomotive force on the electron. In deriving the above equations, I have assumed that all the beam electrons have the same displacement off the axis of the ion channel in the transverse direction, therefore transverse bunching[64] has not been included in the above discussion. I have assumed that the space-charge effects are minimal. In reality, the space-charge effects, particularly for the low beam-energy case, may produce an energy spread on the beam electrons and therefore mix the phases among these electrons. I have also assumed that during the bunching process, the radiation field E is constant.

6.4 Simulation Requirements

The OSIRIS code is used to simulate the electron micro-bunching in an ICL. OSIRIS is a self-consistent, particle-in-cell (PIC) simulation code [68]. The meaning of self-consistency is that the motion for each particle is governed by the Lorentz force (including relativistic effects), while the fields in turn evolve according to Maxwell's Equations with sources provided by the particles. In the PIC method, the fields are calculated on the grids and then interpolated to the particle positions. The dimensions of the grid cells are chosen to resolve the minimum wavelength of interest for the simulated problem. The code then uses the fields and particle information to calculate the new positions and new momenta of the particles after a suitably chosen timestep, dt. The updated position and momentum data are then used to find the sources of the electromagnetic field, i.e., the current and the charge density that are deposited onto the grids. Finally, the sources are used to advance the electromagnetic fields in time via Maxwell's Equations. OSIRIS has been benchmarked with other simulation codes, and in principle it perfectly describes a dynamic system of an ensemble of charged particles interacting with electromagnetic fields within the limits of classical physics.

A moving simulation window in a 2-D cartesian coordinate system has been applied in the code. The window is moving the light speed c. Therefore, for a relativistic beam, the simulation only models the region surroundings the beam, and not the uninteresting regime far behind the beam.

The required number of the time steps on one single CPU node is estimated as follows. Since the minimum wavelength of interest for this problem is the radiation wavelength λ_r, the grid size dx, in the direction of the radiation wave $\hat{x}$, is chosen to be $dx \approx \lambda_r/20$. The grid size in the other dimension dy, is not required to be so small, and is chosen as $dy \approx 10 \cdot dx$ in most cases. The timestep, dt, is required to satisfy

$$dt < \frac{1}{\sqrt{\frac{1}{dx^2} + \frac{1}{dy^2}}} \approx dx \tag{6.26}$$

in the code, according to the Courant condition [70]. Because beam electrons need to traverse several periods of betatron motion in order to be bunched, the total time, Δt, is about $N\lambda_\beta$, with N the period number. Therefore, the total computer running steps, n_s, are $n_s = N\lambda_\beta/dt \geq N\lambda_\beta/dx \approx 40N \cdot \gamma^2$, where $\lambda_\beta \approx 2\gamma^2\lambda_r$ has been used. From the above equation, we can see that the required time steps is proportional to the square of the beam energy.

How much computer time is required to run one time step? It depends on the numbers of grids N_g, the number of particles N_p, the time to advance the fields on each grid t_f, and the time to advance each particle, t_p. The total computer time per step is $N_g \cdot t_f + N_p \cdot t_p$. In a 2-D simulation, $N_g = \Delta x/dx \cdot \Delta y/dy$, where Δx and Δy are the size of the simulation window in the $\hat{x}$ and $\hat{y}$ directions, respectively. In general, the size of the simulation window should be wide enough to eliminate the boundary effects. Another concern in simulating a relativistic beam in a window moving at c is that the beam will eventually slide out of the window due to a slight speed difference between the beam velocity and c. Therefore, the window size in the beam propagating direction, which is Δx in our case, should satisfy $\Delta x >> (c - v_z) \cdot \Delta t$. In a typical simulation run, $\Delta x \approx \Delta y \approx M\lambda_r$ where M is typically chosen to be ~ 100. For this choice of M, the electrons can execute ten's of betatron periods before slipping out the simulation window[2]. Therefore, the number of required grids is $N_g = \Delta x/dx \cdot \Delta y/dy \approx 40M^2$.

Beam electrons typically exist within a small region of the simulation box at $t = 0$, e.g., 5% of the whole simulation box in a typical simulation, with four electrons per grid. The number of electrons N_p is therefore roughly estimated to be $4 \times 40M^2 \times 0.05 = 8M^2$. The beam is the only species of particles in these simulations. The focusing force from the preformed ion-channel is modeled as an external electrostatic field. Therefore, the total running time to simulate an electron bunch moving through a preformed ion channel for N betatron oscillations can be estimated to be

$$t = n_s \cdot (N_g \cdot t_f + N_p \cdot t_p) = 40N\gamma^2(40M^2 t_f + 8M^2 t_p) \qquad (6.27)$$

---

[2] By going through one betatron motion, an electron has a relative displacement with the moving simulation window $x_d \approx (c - v_z) \cdot T_\beta = (c - v_z) \cdot \lambda_\beta \approx \lambda_r$. Therefore, in a simulation window with $\Delta x = 100\lambda_r$, an electron going through 100 times betatron motion may slide from the left side of the simulation window to the right side. However, drag forces such as from the space-charge effect may slow down the electron motion a little bit. An electron may oscillate fewer betatron periods before it slides out of the window. The drag force due to space charge effect is more severe as the Lorentz factor γ is smaller.

The speed of OSIRIS on a single CPU node (Mac G4,for example) is $t_p \approx 6\mu S$(particle push), and $t_f \approx 0.2\mu S$(field solve). Therefore, the ratio of the time for calculating particles to the time for calculating fields is approximately equal to $0.05 \times (\#ofparticles/cell \times t_p/t_f)$, which for our case is 6.5. Therefore the particle push still dominates the field solve. With a typical choice of $N = 20$, $M = 100$ and $\gamma = 50$, the simulation time is $t \approx 10^6$ $Seconds \approx 300$ $hours$. The run time can drop dramatically by decreasing γ. However, as in a real experiment, a beam with low γ spreads due to self-charge effects and this will mix the beam electrons causing a smearing out of the bunching phenomena.

Parallelism could drastically reduce the computational time. However, in this case the particles are located in a small region. While OSIRIS is fully parallelled it does not currently have load balancing. Therefore, for this case parallelism does not help that much.

6.5 Preliminary Simulation Results

We start by attempting to demonstrate longitudinal bunching in an ICL due to the beat between the betatron motion and the electromagnetic wave. The initial conditions for the simulation are as follows. As shown in Fig. 6.3, The simulation window is set to move in x_1 direction with the speed of light, and it is periodic in x_2 direction. The size of the window is 0.4 in x_1 and 1.0 in x_2 respectively, while the corresponding grid was 920×240 cells. The timestep was $dt = 0.000429$. As shown in Fig. 6.3, an REB with $\gamma = 50$ and with a density, $n_b = 1$, is uniformly distributed in the area of $0.2 \leq x_1 \leq 0.3$ and $0.06 \leq x_2 \leq 0.08$ at $t = 0$. The emittance of the beam was set to be zero in both directions. Each grid cell has 4×4 particles. A focusing electric field $\vec{E_\beta} = x_2 \hat{x_2}$ was added into the code to model the focusing force of the ion channel. In addition, as shown in Fig. 6.4, a

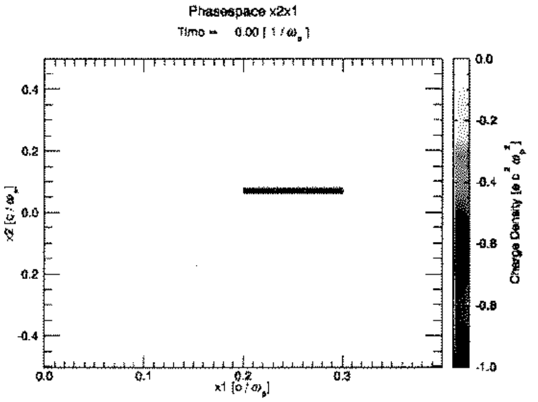

Figure 6.3: A simulation window at t=0. A bunch of electrons with energy $\gamma = 50$ propagates in x_1 direction in a preformed ion channel. A plane electromagnetic wave is at the background, which is shown in Fig. 6.4

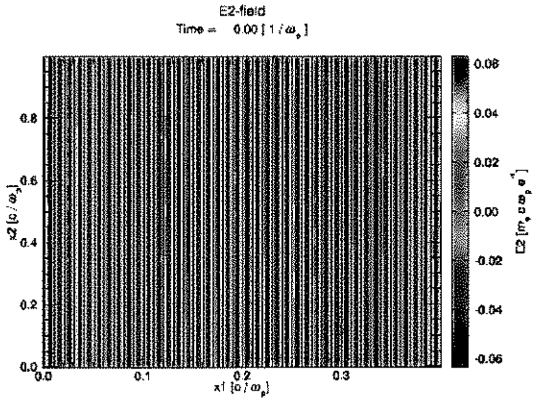

Figure 6.4: A plane electromagnetic wave propagating in x_1 direction has its polarization in x_2 direction, its frequency $\omega = 631.3$ and its magnitude $E = 0.0631$.

plane electromagnetic wave was launched to the right. It was polarized in the x_2 direction with a frequency $\omega = 630.3$ and a magnitude $E = 0.0631$.

The above numbers we are specificially chosen to satisfy the following conditions. The timestep $dt = 0.000429$ is as close to the maximum allowed by the Courant condition, as defined in Eq. 6.26. We chose dt to be as close as possible to the Courant condition limit in order to minimize unphysical Cerenkov emission due to numerical dispersion [70]. We also start with $\langle E \rangle << \langle E_{beta} \rangle$ to satisfy the small signal approximation as mentioned earlier. The betatron frequency ω_β, obtained from Eq. 6.16, is 0.1414. The wiggler strength K, obtained from Eq. 2.27, is 0.49. The resonance frequency ω, obtained from Eq. 6.1, is therefore 630.3.

Figure 6.5 shows the beam electrons' distribution inside the simulation window at $t \approx 215.0$. The modulation of electron density distribution due to the longitudinal bunching is demonstrated in Fig. 6.6, where the electrons' distribution as shown in Fig. 6.5 is summed up in the x_2 direction. From Fig. 6.6, it can be seen that the electrons are bunched with a wavelength near 0.01, which is indeed the wavelength of the plane electromagnetic wave. The ratio $\langle \Delta n \rangle / n_0$ is about 0.04.

Spectral analysis of electrons' distribution for $\omega \approx 631$ plotted as a function of time yields Fig. 6.7, where the theoretical curve based on Eq. 6.25 is also plotted for comparison. It appears that the bunching is growing faster in simulation than in the theory at the early time periods. We have no simple explanation for this discrepancy at this time. The bunching saturates later times at a relatively low level. This may be due to longitudinal energy spread and the fact that numerical dispersion modifies the phase velocity of the EM wave.

We next studied micro-bunching of a beam symmetrically distributed about

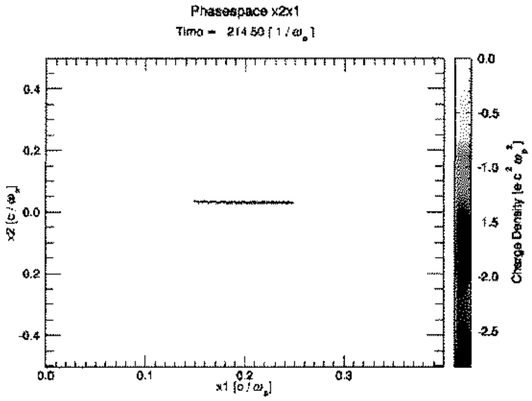

Figure 6.5: A simulation window with electrons' distribution at $t \approx 215$. The initial condition is shown in Fig. 6.3

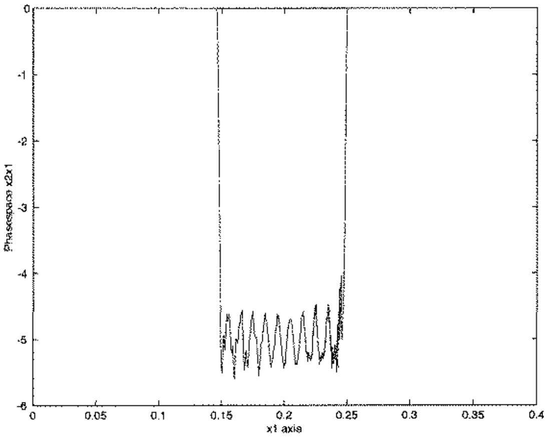

Figure 6.6: The sum of electrons' distribution in x_2 direction at $t \approx 215$.

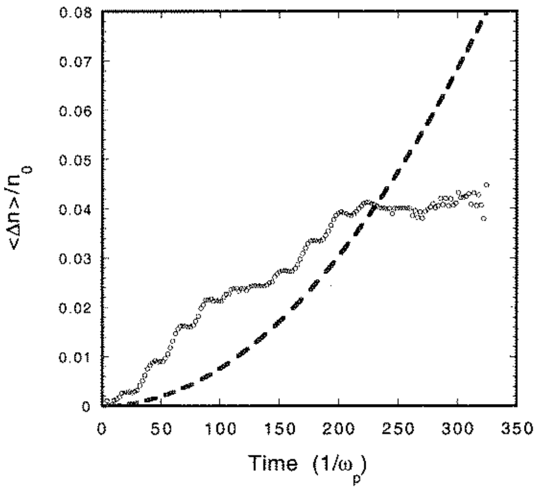

Figure 6.7: Spectral analysis of distribution summed up in x_2 direction on $f \approx 631$ as a function of time. The theoretical curve, based on Eq. 6.25, is plotted as a dashed line.

the channel axis. Electrons are distributed uniformly in the area of $-0.08 \leq x_2 \leq 0.08$. (In the first run, electrons were distributed in the area of $0.06 \leq x_2 \leq 0.08$, therefore all the electrons have almost the same displacements from the axis of the ion channel.) The simulation window at $t = 0$ is shown in Fig. 6.8. All the other simulation conditions are the same as in the first run. Figure 6.9 shows the simulation window at $t = 232$. At this time the envelope of the beam is pinched to its smallest transverse size. In Figure 6.9 we plot the electrons' $x_1 - x_2$ phase space with the resolution of the grids and in Figure 6.10 plot the electrons' exact positions. Figure 6.10 shows that the main body of the beam is bunched at the radiation wavelength of 0.01. The figure also shows that there is a π phase difference between the electron bunching on the two sides of the ion channel, as mentioned earlier in this chapter. It is more complicated to analyze the bunching phenomena in the second run than in the first run. There are at least two effects which have been ignored earlier but need to be included in the second run. One effect is the relativistic mass effect. In view of Eq. 6.17, the average energy

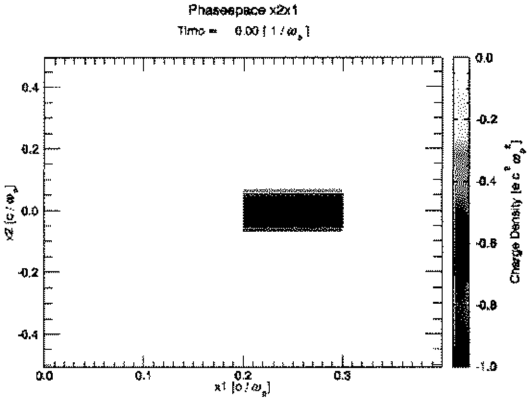

Figure 6.8: The simulation window at $t = 0$, with its initial condition the same with that shown in Fig. 6.3 except here the electrons are distributed in $-0.08 \leq x \leq 0.08$ in x_2 direction.

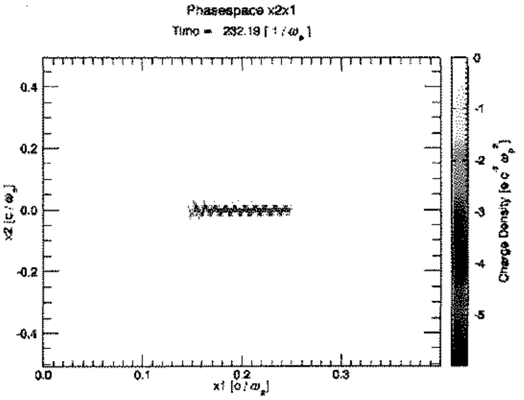

Figure 6.9: The simulation window at $t \approx 232$ with its simulation condition as shown in Fig. 6.3.

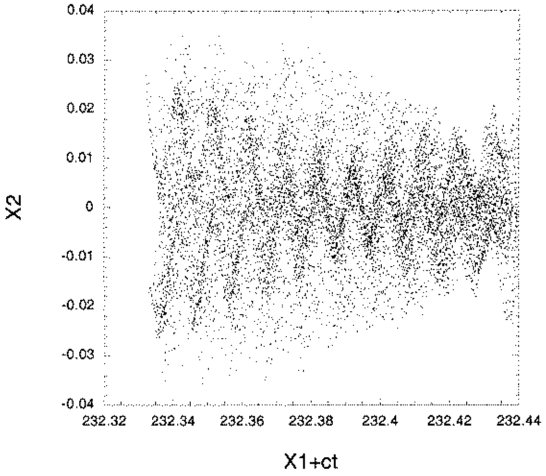

Figure 6.10: Electrons' distribution at $t \approx 232$ with its simulation condition as shown in Fig. 6.3.

of a beam electron is a function of the transverse displacement x_0. Therefore electrons with different transverse displacements have slightly different betatron frequencies due to their slightly different relativistic masses. As a result according to Eq. 6.16, they have slightly different phase relations even if they have the same longitudinal positions. Another effect is space-charge forces. The electrostatic field felt by an electron due to the surrounding electrons varies during its betatron motion because beam electrons are pinched. The variation of this field may also mix the phase relations of electrons.

The third run demonstrates that a micro-bunched beam, i.e., one with radiates more energy than a non micro-bunched beam with the same charge. As shown in Fig. 6.11, a small bunch of electrons with energy $\gamma = 50$ propagates in the x_1 direction in a preformed ion channel. At $t = 0$, they are distributed in the area of $0.2 \leq x_1 \leq 0.22$ and $0.06 \leq x_2 \leq 0.08$(i.e., they are displaced off axis). There is no external radiation field in this run. By doing so, radiation from the beam is much easier to be identified. All the other simulation conditions are the same otherwise as the first run. Figure 6.12 shows the distribution of

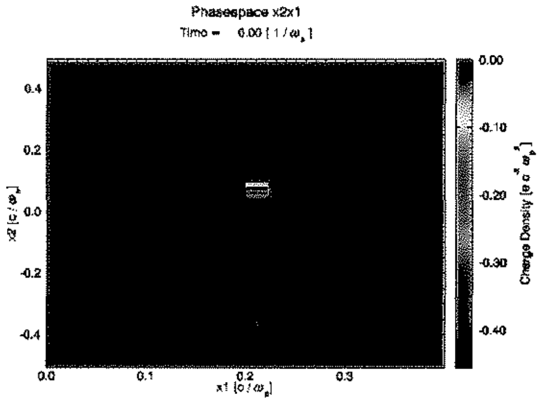

Figure 6.11: A simulation window at t=0. An electron beam with each electron energy $\gamma = 50$ propagates in x_1 direction in a preformed ion channel.

the electric field E_2, in the simulation window at $t \approx 607$. Whereas electrons have slipped backwards behind in the beam propagation direction because their speed is slightly smaller than the velocity of the moving window, the radiation which is produced propagates in the forward direction with the speed of light, and therefore is seen to stay with the window. The position of the electron beam can be identified by the extremely large E2 field associated with it due to its own space-charge effect. The radiation is in front of the beam with a resonance frequency characterized by the the resonance frequency as defined in Eq. 6.1. Figure 6.13 is the plot of the electric field E2 as a function of x_1 at $x_2 \approx 0.47$ at $t \approx 607$. The magnitude of the E_2 field ahead of the beam, i.e., the radiated part is around 0.001. In comparison, we set up another run with the same number of pre-bunched electrons at $t = 0$, as shown in Fig. 6.14. They have the same displacement in the transverse direction with $x_2 \approx 0.07$, but are separated into three bunches in longitudinal direction with the distance equal to 0.01. This distance is equal to the radiation wavelength defined by the resonance

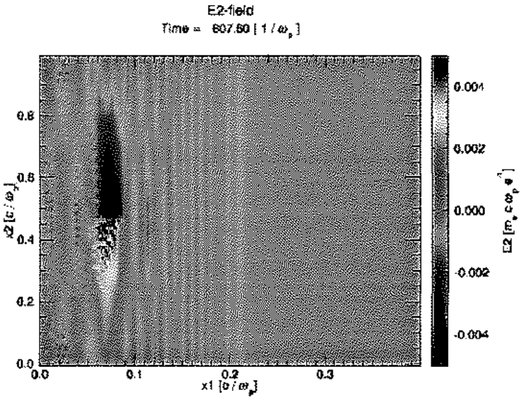

Figure 6.12: the distribution of the electric field in $\hat{x_2}$ direction, E2, in the simulation window at $t \approx 607$. with the simulation window at t=0 demonstrated in Fig. 6.11

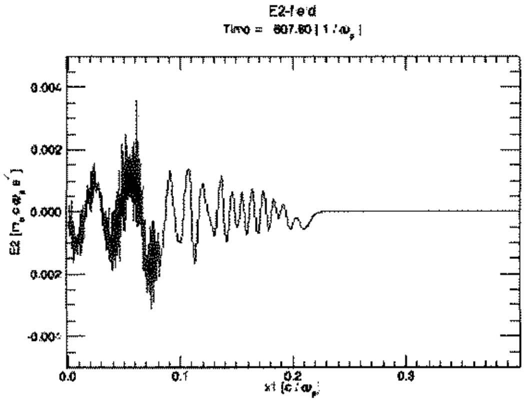

Figure 6.13: The E2 field as a function of x_1 at $x_2 \approx 0.46$ at $t \approx 607$. with its distribution shown in Fig. 6.12.

condition, as is given in Eq. 6.1. All the other simulation parameters are the same. Figure 6.15 demonstrates the distribution of the electric field E_2 in the simulation

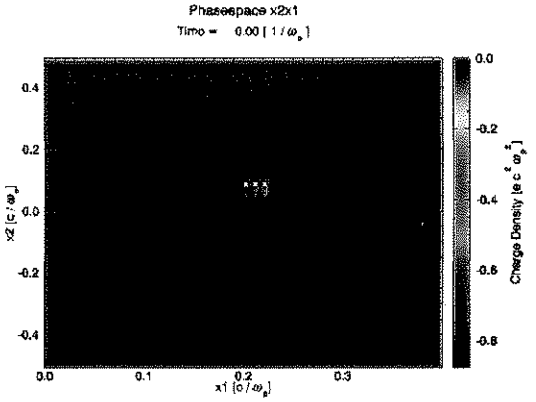

Figure 6.14: A simulation window at t=0. A micro-bunched electron beam with each electron energy $\gamma = 50$ propagates in the $\hat{x_1}$ direction in a preformed ion channel.

window at $t \approx 607$ for this run. In Fig. 6.15 we plot the electric field E_2 as a function of x_1 at $x_2 \approx 0.46$ at $t \approx 607$. The magnitude of the E2 field radiated from the pre-micro-bunched beam is now roughly 0.003, which as expected is 3 times larger than the radiation from a non pre-micro-bunched beam. It should be noted that the decrease of E2 field behind the bunches, as shown in the back of Fig. 6.15, is due to the destructive interference of the radiation reflected from the conducting boundaries. This effect can be removed by simulating a wider region at the expense of a longer simulation time.

6.6 Summary

In this chapter, the ICL concept and the difference between it and a conventional magnetic FEL are reviewed. An ICL has advantages over its magnetic counterpart in that it doesn't require external magnetic structures and waveg-

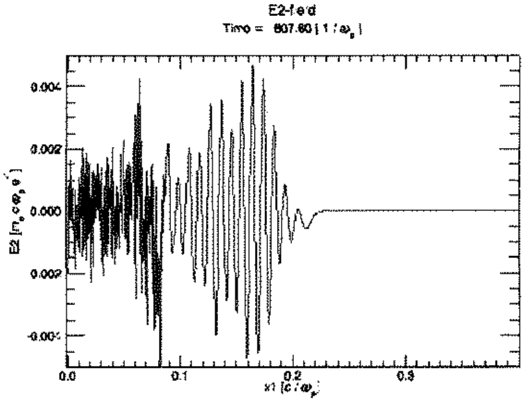

Figure 6.15: The E2 field as a function of x_1 at $x_2 \approx 0.46$ at $t \approx 607$. The initial condition for this run is demonstrated in Fig. 6.14.

uides, and that it offers potentially greater flexibility because the wiggler wavelength can be tuned by changing the plasma density rather than by changing the magnetic poles. Its disadvantages are that the requirement of the beam emittance are more stringent in an ICL than in an FEL, and that other plasma instabilities such as the electron hose instability may deteriorate the desired beam-photon feedback. It is suggested that a PIC simulation which includes all the important physics inside the plasma is very crucial in fully testing the possibility of realization of an ICL.

The electron micro-bunching due to the beat between the electron betatron motion and the radiation wave has been analyzed. The modulation of electron density as a function of time is derived. In this derivation, it is assumed that all the beam electrons have the same displacement off the axis of the ion channel in the transverse direction, therefore transverse bunching was not included in the above discussion. It was also assumed that the space-charge effects are minimal.

The challenges for simulating an ICL with a PIC code were discussed. Estimates for the required number of time steps and the time for a simulation run on a single node were given. It was also pointed out that load balancing is required if parallel computers are to be of use.

Three preliminary simulation results were demonstrated with the code OSIRIS. First it was shown that a REB displaced off axis is bunched as it traverses a preformed ion channel by the ponderomotive force of a low amplitude, plane electromagnetic wave and the ion-channel focusing. The modulation of electron density in the simulation is larger than the prediction of the theory at the early time. Secondly, bunching of beam symmetrically distributed about the axis of a preformed ion channel was shown. The beam electrons at the two sides of the ion channel are bunched π out of phase, as expected from the theory. Last, it was shown that a micro-bunched beam radiates more energy than a non bunched beam with the same amount of charge.

CHAPTER 7

Conclusion

In this thesis, a novel radiation device – a plasma wiggler with an ion channel (PWIC) has been addressed both experimentally and theoretically. In the theory sections, the emission and characteristics of spontaneous emission theory, and the possibility of obtaining stimulated emission in a PWIC have been studied. The experiment which demonstrated X-ray radiation due to electron betatron motion has been carried out. The thesis has also detailed the construction of one of the pivotal components in the experiment – a 1.4 meter long lithium plasma source.

The novelty of a PWIC, compared to its magnetic counterpart, lies in the fact that an electrostatic field has been employed to wiggle a relativistic electron beam. Based on the trajectory of a relativistic electron traversing an ion channel the spontaneous emission due to the electron's betatron motion has been discussed. The radiation spectrum from an electron has been numerically calculated. The radiation from an REB traversing an ion channel is the sum of the radiations from each electron in the beam by assuming there is no phase relation among the radiation fields from each electron. Based on that, the essentials of a PWIC such as the radiation power, the radiation angular distribution, the flux and the spectral brightness have been derived as functions of beam and plasma parameters. In principle, this electrostatic field can also be supported by a plasma wave. Since it is relatively easier to acquire an ion channel than a plasma wave, a PWIC becomes the first plasma wiggler to be realized in an experiment.

A 1.4 *meter* long plasma source for PWFA experiment has been developed and fully characterized. This source contains a 1.4 m homogeneous lithium vapor column with the vapor density that can be tuned in the range of $(2.9 \sim 5.0) \times 10^{15}\ cm^{-3}$. The plasma is created by photo-ionizing the lithium vapor with a 193 nm ArF laser. The plasma density is of the order of $10^{14}\ cm^{-3}$, which is proportional to the the UV energy. The homogeneity of the plasma column depends on the uniformity of the laser profiles along the oven.

Spontaneous emission in a PWIC was demonstrated as a a parasitic project of the plasma-wakefield-acceleration experiment called E157. In E-157, the SLAC high peak-current, 28.5 GeV, REB (relativistic electron beam) traverses a 1.4 m long lithium plasma source in the underdense plasma regime. The head of the beam expels plasma electrons and generates an ion channel. The focusing force of the ion column is subsequently experienced by the main body of the beam. Besides the betatron motion inside an ion channel, which contributes to the spontaneous emission, E-157 has also demonstrated other important transverse effects including bending an REB at the plasma neutral gas boundary, electron betatron motion and sloshing and hosing of an REB in a plasma. All the above effects and the related diagnostic techniques have been reviewed in the thesis.

We have demonstrated broad band X-ray radiation due to betatron motion in E-157. Several diagnostic techniques such as Thomson scattering, Bragg scattering and X-ray fluorescence techniques have been applied. The quadratic density dependence of the spontaneously emitted betatron X-ray radiation and the divergence angle of $(1 \sim 3) \times 10^{-4}$ radian of the forward emitted X-rays as a consequence of betatron motion in the ion channel are in good agreement with theory. The absolute photon yield and the peak spectral brightness at 14.2 KeV photon energy are roughly estimated to be on the order of

$10^{19}\, photons/(sec \cdot mrad^2 \cdot mm^2 \cdot 0.1\% bandwidth)$. Although microwave radiation has been observed in this underdense or ion-focussed regime, no measurements of X-rays have been reported to our knowledge.

Finally the challenges to realizing stimulated emission inside a PWIC – ion channel lasing (ICL) has been addressed. The requirement on the beam emittance is more stringent in an ICL than in an FEL. Plasma instabilities such as the electron hose instability may hinder the phase bunching of beam electrons. A self-consistant PIC simulation which includes all the important physics inside the plasma is critical for fully testing the possibility of realization of an ICL. Some preliminary simulations have been introduced. A low energy REB is seen to micro-bunch on the scale of the radiation wavelength due to the beat between the betatron motion and the electromagnetic wave. Unbearablly long CPU time is at present the hurdle to simulating an ultrarelativisitic electron beam (the Lorentz factor $\gamma > 2000$) traversing an ion channel.

Nevertheless, a plasma wiggler comprising of only a plasma cell offers simplicity of construction, flexibility in undulator wavelength, and potential savings of cost over its magnetic wiggler counterpart in future generation of light sources. This will stimulate more R&D in developing this kind of devices.

APPENDIX A

A Magnetic Wiggler/Undulator

A schematic of a conventional wiggler/undulator source is illustrated in Fig. A.1. As an electron beam is injected orthogonal to the wiggler magnetic field but along its axis, it undergoes a periodic oscillation, perpendicular to both its direction of motion and the magnetic field, through the wiggler due to the Lorentz force. The motion of each particle is composed of a relativistic longitudinal motion and a nonrelativistic transverse oscillation. The transverse oscillations allow the particle to radiate. As it is well known that the center radiation wavelength of a wiggler/undulator is characterized as

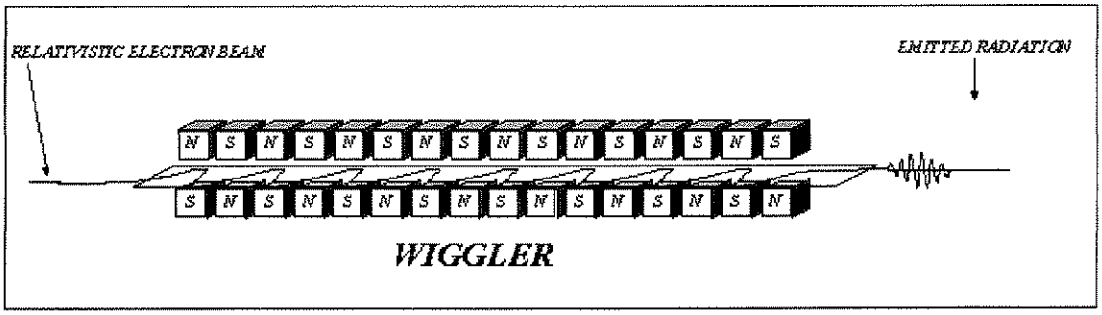

Figure A.1: A schematic of a relativistic electron beam traversing a magnetic wiggler.

$$\lambda_0 \sim \frac{\lambda_w}{(2\gamma^2)}, \tag{A.1}$$

where λ_w is the wiggler wavelength. The $1/(2\gamma^2)$ term can be understood intuitively from the double Doppler shift when transforming to the beam frame to calculate the oscillation frequency and back to beam frames to calculate the radiation frequency. The radiation is concentrated within an angle $\Delta\theta \sim O(1/\gamma)$ to the observation direction because the time-contraction effect is maximum at this angle [25]. Therefore, the radiation from a wiggler is similar to the sum of radiations from a series of bending magnets. An undulator is similar to a wiggler except for one characteristic: it forces the electrons into a much weaker oscillation, so that during the entire motion synchrotron light continues to illuminate the undulator beamline. This implies that the radiation detected by an observer is an almost coherent superposition of the contributions from all the oscillations of the trajectory. For perfect coherence and an infinite number of magnet periods, the radiation would be monochromatic, producing high levels of flux and brightness.

The difference between a wiggler and an undulator can be more quantified by the magnitude of the wiggler strength K[25], which is a scale angle satisfying

$$K = \frac{\gamma k_w}{\rho}, \tag{A.2}$$

where $k_w = 2\pi/\lambda_w$ with λ_w the wiggler period, and ρ the effective radius of curvature of the path. ρ is proportional to the effective mass of the electron but inversely proportional to the Lorentz force, and can be deduced in a magnet wiggler/undulator as

$$\rho = \frac{k_w^2 \gamma m c^2}{e B_W}, \tag{A.3}$$

with B_W the wiggler magnet strength. Therefore an alternative expression of the wiggler strength K in terms of the magnetic strength, is

$$K = \frac{e B_W}{k_w m c^2}. \tag{A.4}$$

Normally a device with $K << 1$ is called an undulator, and one with $K >> 1$ is a wiggler.

A free electron laser is an undulator where the radiation inside the undulator acts strongly with the electron beam and bunches it on the scale of the radiated wavelength. These bunched electrons now radiate in phase leading to coherent emission of radiation as opposed to spontaneous emission emitted by an unbunched beam.

APPENDIX B

The Vapor Pressure Curve of Lithium

Vapor pressure is the pressure of a vapor over a liquid (and some solids) at equilibrium. Because alkali metals are widely used in modern science and technology, their thermodynamics properties such as vapor pressure, have been the subject of both experimental and theoretical investigations. The vapor pressure only depends on the vapor temperature. Experimental data on the saturated vapor pressure of lithium in the temperature range from the triple point (the temperature at which the material can coexist in all three phases in equilibrium, $T_{tr} = 180.54\ {}^0C$ at $1\ atm.$), to the critical point (the highest temperature at which a gas can be converted to a liquid by an increase in pressure, $T_{cr} \approx 3071\ {}^0C$) have been critically assessed in the past. We list three most recent theoretical results on the lithium vapor pressure curve $P(T)$ here. The vapor densities are calculated based on the thermo-equilibrium equation, $n_0 = P(T)/(k_B \cdot T)$, with k_B the Boltzman constant. These theoretical vapor pressure curves are deduced by least-square-fitting a number of reliable experimental data and then by extrapolating to the critical temperatures. Fortunately the vapor pressures and the vapor temperatures on which we are working are not so high, and all three theoritical results data are very close in these ranges. The following equations B.1, B.2, and B.3 for the vapor pressure of lithium are from references [73], [71] and [72], respectively.

$$log(P_{vp}/atm) = A + B/(T/K) + C \cdot log(T/K) \tag{B.1}$$

with $A = 8.409,\ B = -8423,\ C = -0.7074.$

$$ln(P_{vp}/MPa) = A + B/(T/K) + Cln(T/K) \tag{B.2}$$

with $A = 13.0719,\ B = -18880.659,\ C = -0.4942.$

$$ln(P_{vp}/MPa) = cln(T/K) + a_{-1}(10^{-3} \cdot T/K)^{-1} + a_0 + a_1(10^{-3} \cdot T/K) \tag{B.3}$$

with $c = -2.0532,\ a_{-1} = -19.4268,\ a_0 = 9.4993,\ a_1 = 0.753.$

Figure B.1 shows the vapor density as a function of vapor temperature up to 2000 ^0C. A rectangle inside this figure is the range at which our meter long oven

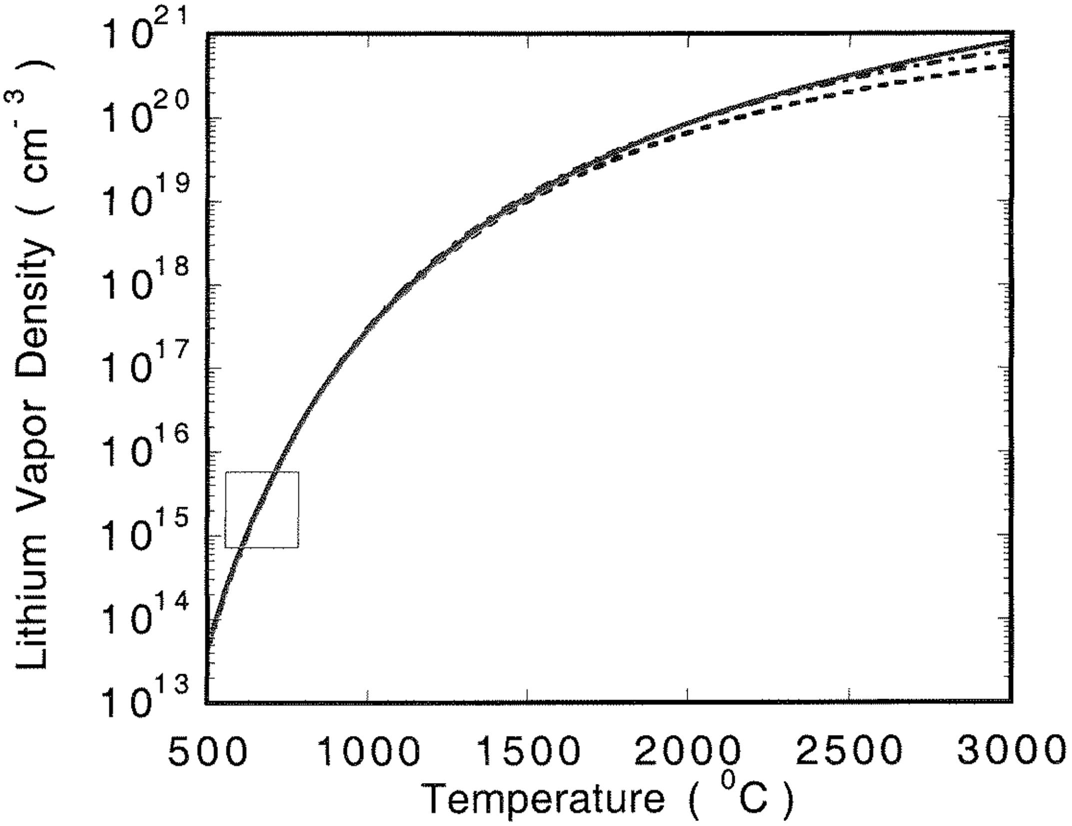

Figure B.1: Vapor densities of lithium as a function of vapor temperature in the range of 500 $\sim$ 3000 ^0C, whereas the *dash* line, the *dash* – *dot* – *dash* line and the *solid* line are drawn based on equations B.1, B.2, and B.3, respectively.

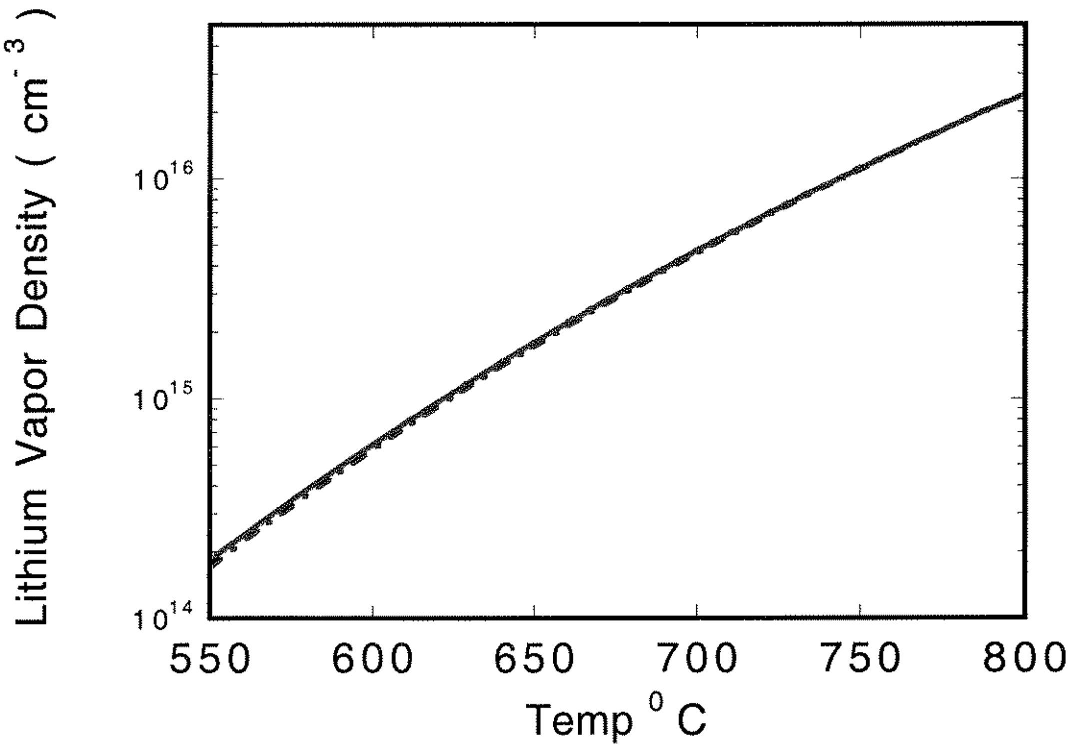

Figure B.2: Vapor densities of lithium as the function of vapor temperatures in the range of 500 ~ 800 ^0C, whereas the *dash* line, the *dash* – *dot* – *dash* line and the *solid* line are drawn based on equations B.1, B.2, and B.3, respectively.

works on, and is blown up as shown in Fig B.2. Table B.1 lists the vapor pressures, and the corresponding vapor densities as a function of vapor temperatures in the blow-up region based on references [71] and [72].

Temp ^{0}C	Pressure $mTorr$ [71]	Density cm^{-3} [71]	Pressure $mTorr$ [72]	Density cm^{-3} [72]	Temp ^{0}C	Pressure $mTorr$ [71]	Density cm^{-3} [71]	Pressure $mTorr$ [72]	Density cm^{-3} [72]
500.0	3.38	4.22e+13	3.70	4.62e+13	650.0	164.22	1.72e+15	171.04	1.79e+15
503.0	3.71	4.62e+13	4.06	5.05e+13	653.0	175.19	1.83e+15	182.30	1.90e+15
506.0	4.07	5.04e+13	4.44	5.50e+13	656.0	186.82	1.94e+15	194.23	2.02e+15
509.0	4.46	5.50e+13	4.86	6.00e+13	659.0	199.14	2.06e+15	206.85	2.14e+15
512.0	4.88	6.00e+13	5.31	6.54e+13	662.0	212.17	2.19e+15	220.20	2.27e+15
515.0	5.33	6.54e+13	5.81	7.11e+13	665.0	225.97	2.33e+15	234.31	2.41e+15
518.0	5.83	7.12e+13	6.34	7.74e+13	668.0	240.57	2.47e+15	249.23	2.56e+15
521.0	6.37	7.74e+13	6.92	8.41e+13	671.0	256.01	2.62e+15	265.00	2.71e+15
524.0	6.95	8.42e+13	7.55	9.14e+13	674.0	272.34	2.78e+15	281.65	2.87e+15
527.0	7.59	9.15e+13	8.22	9.92e+13	677.0	289.59	2.94e+15	299.23	3.04e+15
530.0	8.27	9.94e+13	8.95	1.08e+14	680.0	307.81	3.12e+15	317.78	3.22e+15
533.0	9.01	1.08e+14	9.75	1.17e+14	683.0	327.05	3.30e+15	337.35	3.41e+15
536.0	9.81	1.17e+14	10.60	1.26e+14	686.0	347.35	3.50e+15	358.00	3.60e+15
539.0	10.67	1.27e+14	11.52	1.37e+14	689.0	368.78	3.70e+15	379.76	3.81e+15
542.0	11.61	1.37e+14	12.52	1.48e+14	692.0	391.39	3.92e+15	402.70	4.03e+15
545.0	12.61	1.49e+14	13.59	1.60e+14	695.0	415.22	4.14e+15	426.87	4.26e+15
548.0	13.70	1.61e+14	14.74	1.73e+14	698.0	440.35	4.38e+15	452.32	4.50e+15
551.0	14.87	1.74e+14	15.98	1.87e+14	701.0	466.82	4.63e+15	479.11	4.75e+15
554.0	16.13	1.88e+14	17.32	2.02e+14	704.0	494.70	4.89e+15	507.31	5.01e+15
557.0	17.48	2.03e+14	18.76	2.18e+14	707.0	524.06	5.16e+15	536.97	5.29e+15
560.0	18.94	2.20e+14	20.30	2.35e+14	710.0	554.97	5.45e+15	568.18	5.58e+15
563.0	20.51	2.37e+14	21.96	2.54e+14	713.0	587.49	5.75e+15	600.98	5.88e+15
566.0	22.20	2.55e+14	23.74	2.73e+14	716.0	621.70	6.07e+15	635.46	6.20e+15
569.0	24.01	2.75e+14	25.65	2.94e+14	719.0	657.67	6.40e+15	671.69	6.54e+15
572.0	25.95	2.96e+14	27.70	3.17e+14	722.0	695.49	6.75e+15	709.74	6.89e+15
575.0	28.04	3.19e+14	29.90	3.40e+14	725.0	735.23	7.11e+15	749.70	7.25e+15
578.0	30.27	3.43e+14	32.25	3.66e+14	728.0	776.97	7.49e+15	791.64	7.63e+15
581.0	32.67	3.69e+14	34.77	3.93e+14	731.0	820.82	7.89e+15	835.65	8.04e+15
584.0	35.24	3.97e+14	37.47	4.22e+14	734.0	866.85	8.31e+15	881.82	8.45e+15
587.0	37.99	4.26e+14	40.36	4.53e+14	737.0	915.16	8.75e+15	930.24	8.89e+15
590.0	40.93	4.58e+14	43.44	4.86e+14	740.0	965.85	9.20e+15	981.00	9.35e+15
593.0	44.08	4.91e+14	46.74	5.21e+14	743.0	1019.01	9.68e+15	1034.20	9.83e+15
596.0	47.45	5.27e+14	50.25	5.58e+14	746.0	1074.76	1.02e+16	1089.95	1.03e+16
599.0	51.04	5.65e+14	54.01	5.98e+14	749.0	1133.21	1.07e+16	1148.34	1.08e+16
602.0	54.88	6.06e+14	58.02	6.40e+14	752.0	1194.45	1.13e+16	1209.48	1.14e+16
605.0	58.98	6.49e+14	62.29	6.85e+14	755.0	1258.61	1.18e+16	1273.49	1.20e+16
608.0	63.36	6.94e+14	66.85	7.33e+14	758.0	1325.81	1.24e+16	1340.47	1.26e+16
611.0	68.03	7.43e+14	71.71	7.83e+14	761.0	1396.17	1.30e+16	1410.56	1.32e+16
614.0	73.00	7.95e+14	76.88	8.37e+14	764.0	1469.82	1.37e+16	1483.86	1.38e+16
617.0	78.30	8.49e+14	82.38	8.94e+14	767.0	1546.88	1.44e+16	1560.52	1.45e+16
620.0	83.95	9.08e+14	88.24	9.54e+14	770.0	1627.51	1.51e+16	1640.65	1.52e+16
623.0	89.96	9.69e+14	94.47	1.02e+15	773.0	1711.82	1.58e+16	1724.39	1.59e+16
626.0	96.35	1.03e+15	101.09	1.09e+15	776.0	1799.98	1.66e+16	1811.88	1.67e+16
629.0	103.16	1.10e+15	108.13	1.16e+15	779.0	1892.13	1.74e+16	1903.27	1.75e+16
632.0	110.39	1.18e+15	115.60	1.23e+15	782.0	1988.43	1.82e+16	1998.70	1.83e+16
635.0	118.07	1.26e+15	123.53	1.31e+15	785.0	2089.03	1.91e+16	2098.33	1.91e+16
638.0	126.24	1.34e+15	131.96	1.40e+15	788.0	2194.10	2.00e+16	2202.30	2.00e+16
641.0	134.91	1.42e+15	140.89	1.49e+15	791.0	2303.80	2.09e+16	2310.79	2.10e+16
644.0	144.11	1.52e+15	150.36	1.58e+15	794.0	2418.32	2.19e+16	2423.96	2.19e+16
647.0	153.87	1.61e+15	160.40	1.68e+15	797.0	2537.83	2.29e+16	2541.99	2.29e+16

Table B.1: Lithium vapor pressure and vapor density

APPENDIX C

SLAC and FFTB

SLAC is operated under contract from the United States Department of Energy (DOE) as a national basic research laboratory by Stanford University. Its function is to probe the structure of matter at the atomic scale with x-rays and at much smaller scales with electron and positron beams. The major facilities at SLAC are the linac, End Station A, SPEAR and SSRL, PEP II, SLC, and the FFTB. The linac is a three kilometer long accelerator capable of producing electron and positron beams with energies up to 50 GeV. End Station A is for fixed target experiments. Early work in End Station A showed that the constituents of the atomic nucleus, the proton and neutron, are themselves composed of smaller, more fundamental objects called quarks. The Stanford Synchrotron Radiation Laboratory (SSRL) uses the SPEAR storage ring to produce intense x-ray and ultraviolet beams for probing matter on the atomic scale. PEP II is a storage ring for a B meson factory in which an experiment, BaBar, is seeking to answer why the universe is made of matter and not anti-matter. The Stanford Linear Collider (SLC) in conjunction with the Stanford Large Detector (SLD), analyzed collisions of 50 GeV electrons on 50 GeV positrons in order to determine the mass and other properties of the carrier of the weak force of subatomic physics. The Final Focus Test Beam (FFTB) is a facility for research on future accelerator design. The E157 experiment was located inside the FFTB.

The FFTB was designed to be a facility used for the development and study

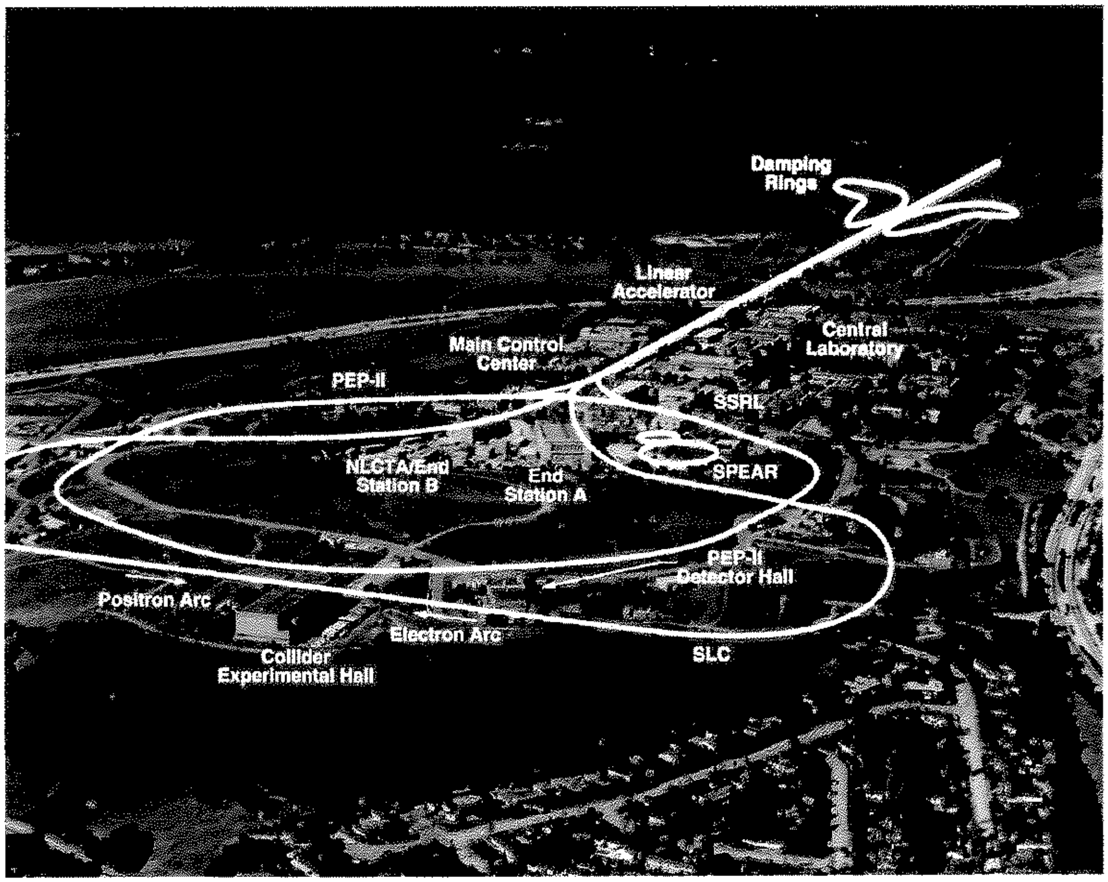

Figure C.1: Annotated aerial view of SLAC (Copied from www.slac.stanford.edu).

of optical systems, instrumentation, and techniques needed to produce the small beam spot sizes required for future electron-positron colliders. It occupies 200 m in the straight-ahead channel at the end of the SLAC linac. The design consists of five key sections. The first part is a matching section to match the beam that appears at the end of the linac to the lattice of the FFTB beamline. This matching section also has lens to match the betatron space of the beam to the second section, the chromatic correction section. The second, third, and fourth sections are used to correct chromatic and geometric aberrations on the beam. The final section is a telescope that focuses the beam down to a small spot size. The optics of the FFTB consist of dipoles, quadrupoles, and sextuples. Various diagnostic machines were built to determine the spot size and position of the beam along the beamline. These include toroids (to measure the beams charge), wire scanners (to measure spot size), and BPMs (to measure the beams position). A BPM is inserted into the aperture of each quadrupole magnet to measure beam positions pulse to pulse. Measurement of transverse profiles of the distribution of beam particles is done at several points along the FFTB beam line. Wirescanners, able to resolve beam profiles as small as 1 μm, are used to make measurements of the beam phase space and to verify the properties of the magnetic lattice in the β-matching and β-exchange sections. A inside view of FFTB at the IP1 site is shown in Fig. C.2.

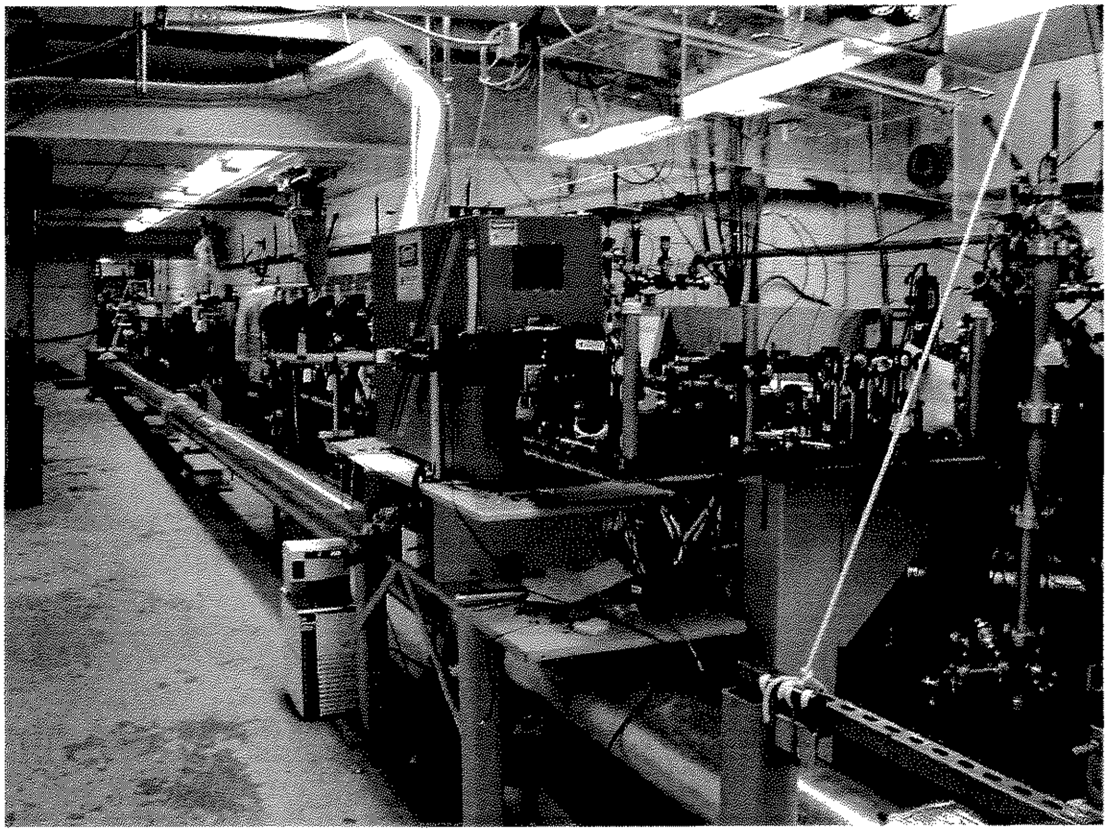

Figure C.2: An inside view of FFTB from IP1 to the beam dump showing the location of the E-157 experiment. The ionizing ArF laser (orange box) can been seen in the foreground.

REFERENCES

[1] T. Tajima and J. M. Dawson, "Laser Electron Accelerator", Phys. Rev. Lett., **43**, 705, (1979).

[2] D. Gordon, *et al.,* "Observation of Electron Energies Beyond the Linear Dephasing Limit from a Laser Excited Relativistic Plasma Wave", Phys. Rev. Lett, **80**, 2133, (1998).

[3] P. Chen, *et al.*, "Plasma Based Adiabatic Focuser", Phys. Rev. Lett., **64**, 1231, (1990); J. J. Su, *et al.*, " Plasma Lenses for Focusing Particle Beams", Phys. Rev. A, **41**, 3321, (1990).

[4] P. Chen and D. Walz, "CERN Courier, 40 (9), 24-26, (2000). J. S. T. Ng, P. Chen, *et al.*, "Observation of Plasma Focusing of a 28.5 GeV Positron Beam", Phys. Rev. Lett., **87**, 244801, (2001);

[5] P. Muggli*et al.*, "Refraction of a Particle Beam", Nature, **411**, 43, (2001).

[6] C.Joshi, *et al.*, "Plasma Wave Wigglers for Free Electron Lasers", IEEE Journal of Quantum Electronics **23**, 1573 (1987).

[7] D. H. Whittum, A. M. Sessler, and J. M. Dawson, "Ion channel Laser", *Phy. Rev. Lett* , Vol. 64, 2511, (1990).

[8] H. Winick, "Synchrotron Radiation", Scientific American, **11**, 88, (1987).

[9] R. Fedele, *et al.*, "The Plasma Undulator",Physica Scripta **30**, 192 (1990).

[10] E. Esarey, *et al.,* "Nonlinear Thomson Scattering of Intense Laser Pulses from Beams and Plasmas ", Phys. Rev. E, **48**, 3003, (1993).

[11] R. Bonifacio, C. Pellegrini, and L. Narducci, "Collective Instabilities and High-Gain Regime in a Free Electron Laser", Opt. Commun., **50**, 373, (1984).

[12] R. L. Williams, *et al.*, "Studies of Classical Radiation Emission from Plasma Wave Undulators", IEEE Trans. Plasma Sci.,**21**, 166, (1993).

[13] T. C. Katsouleas, "On the Effect of Beam Ionization in E-157", ARDB notes, Vol.2, Stanford Linear Acceleration Center.

[14] W. E. Martin, *et al.,* "Electron-Beam Guiding and Phase-Mix Damping by a Laser-Ionized Channel", Phys. Rev. Lett, **54**, 685, (1985).

[15] H. L. Buchanan, "Electron Beam Propagation in the Ion-Focused Regime", Phys. Fluids, **30**, 221, (1987).

[16] E. P. Lee, "Radiation Damping of Betatron Osciallations", Lawrence Livermore National Laboratory, Livermore, CA, UCID-19381, (1982).

[17] E. Esarey, *et al.*, "Overview of Plasma Based Accelerator Concepts", IEEE Trans. Plasma Sci., **24**, 252, (1996).

[18] J. M. Dawson, "Nonlinear Electron Oscillations in a Cold Plasma", Phys. Rev., **133**, 383-387, (1959).

[19] C. K. Huang, *et al.*, Proceedings of the 2001 Particle Accelerator Conference (2001).

[20] M. Hogan, *et al.*, "E-157: A 1.4-m-long plasma wake field acceleration experiment using a 30 GeV electron beam from the Stanford Linear Accelerator Center Linac", Phys. Plasmas **7**, 2241, (2000).

[21] D. H. Whittum, " Nonlinear, relativistic return current sheath for an ion-focused beam", Phys. Fluids **4**, 476, (1992).

[22] K. L. F. Bane, "Physics of Particle Accelerators", AIP Conf. Proc., **153**, AIP, New York, (1987).

[23] J. D. Jackson, "Classical Electrodynamics", J. Wiley and Sons, N. Y. (1975).

[24] E. Esarey *et al.*, AIP Proceedings, **569**, 473, (2001).

[25] K. J. Kim, AIP Con. Proceedings**184**, 565, (1989).

[26] J. D. Lawson, "The physics of charged particle beams", (second edition), Oxford U. P., London, 161, (1988).

[27] H. Wiedemann, "Particle Accelerator Physics II", Sprnger, 266, (1995).

[28] D. H. Whittum, *et al.,* "Electron-hose Instability in the Ion-focused Regime", Phys. Rev. Lett., *67*, 991, (1991).

[29] J. B. Rosenzweig, *et al.,* "Experimental Observation of Plasma Wake-Field Acceleration", Phys. Rev. lett., **61**, 98, (1988), and references in.

[30] S. Lee, *et al.,* "Simulations of a Meter-Long Plasma Wakefield Accelerator", Phys. Rev. E, **61**, 7014, (2000).

[31] C. R. Vidal and J. Cooper, "Heat-Pipe Oven: A New, Well-Defined Metel Vapor Device for Spectroscopic Measurements", J. App. Phys. **40**, 3370, (1969).

[32] A. E. Siegman, " Lasers", University Science Books, (1986).

[33] R. Landerburg, "Dispersion in electrically excited gas", Rev. Modern Phys. **5**,No.4, 243, (1933).

[34] CRC Handbook of Chemistry and Physics, **72**nd ed., Boca Raton, FL:CRC Press, (1991).

[35] M. C. E. Huber, "Modern Optical Methods in Gas Dynamics Research", PP85, Plenum Press, New York, (1971).

[36] G. M. Grover, *et al.,* J. App. Phys. **35**, 1990, (1964).

[37] P. Muggli *et al.*, " Photo-Ionized Lithium Source for Plasma Accelerator Application ", IEEE Trans. Plasma Sci.,**27**, 791, (1999).

[38] C. R. Vidal, "Spectroscopic observations of subsonic and sonic vapor flow inside an open-ended heat pipe", J. Appl. Phys.,**44**, 2225, (1973).

[39] D. S. Rozhdestvenskii, Ann. Physik **39** , 307, (1912).

[40] , W. C. Marlow, "Hakenmethode", Appl. Opt.,**6**,1715, (1967).

[41] R. B. Miles *et al.*, "Optical third-harmonic generation in alkali metal vapors", IEEE J.QE,**9**,470,(1973).

[42] ,V. F. Weisskopf, Z. Physik,**75**, 287, (1932).

[43] W. W. Houston, "Resonance broadening of spectral lines ", Phys. Rev.,**54**,884, (1938).

[44] H. Margenau *et al.*, Rev. Mod. Phys.,**8**,22, (1936).

[45] W. Furssow, *et al.*, Physik. Z. Sowjetunion,**10** ,378, (1936).

[46] G. V. Marr, "Photoionization process in gases", New York: Academic, (1967).

[47] T. C. Katsouleas, "Physical Mechanisms in the Plasma Wake-Field Accelerator", Phys. Rev. A**33**, 2056, (1986).

[48] I. M. Frank, "Transition Radiation and Optical Properties of Matter", Sov. Phys. Uspekhi, **8**, 729, (1966).

[49] A thorough review on Cherenkov radiation: V. L. Ginzburg, "Radiation by Uniformly Moving Sources (Vavilov-Cherenkov effect, transition radiation, and other phenomena)", Physics-Uspekhi, textbf 39, 973-982, (1996).

[50] D.W.Rule, *et al.*, Nucl. Instrum. Methods Phys. Res., Sect. B **24**/25, 901, (1987).

[51] R. Assmann, *et al.*, "Progress Toward E-157: A 1 GeV Plasma Wakefield Accelerator", Proceedings of the 1999 Particle Accelerator Conference, New York (IEEE, Piscataway, NJ, 1999).

[52] R. Siemann, "Beam Envelope Dependence on Plasma Density", ARDB notes, Vol.3, Stanford Linear Acceleration Center.

[53] C. Clayton, *et al.*, "Transverse envelope dynamics of a 28.5-GeV electron beam in a long plasma", Phys. Rev. Lett. **88**, 154801 (2002).

[54] B. Blue, *et al.*, Proceedings of the 2001 Particle Accelerator Conference (2001).

[55] E. S. Dodd, *et al.*, "Hosing and Sloshing of Short-Pulse GeV Class Wakefield Drivers", Phys. Rev. Lett. **88**, 125001 (2002).

[56] D. H. Whittum, *et al.*, "Experimental studies of microwave amplification in the ion-focused regime ",IEEE Trans. Plasma Sci., **21**, 136, (1993).

[57] A. Guinier, "X-Ray Diffraction", W. H. Freeman and Company (1963).

[58] International Tables of Crystallography, Vol. III, The kynoch Press, Birminham (1962).

[59] Sir Lawrence Bragg, *et al.*, "The Development of X-ray Analysis", G. Bell and Sons LTD, (1975).

[60] Z. G. Pinsker, "Dynamical Scattering of X-Rays in Crystals", Springer-Verlag Berlin Heidelberg New York, (1978).

[61] X-ray database from website www-cxro.lbl.gov.

[62] S.Wang, *et al.*, Proceedings of the 2001 Particle Accelerator Conference (2001).

[63] T. J. Orzechowski *et al.*, IEEE J. Quantum Electron. **21** , 831, (1985).

[64] K. R. Chen *et al.*, "On the Amplificatioin Mechanism of the Ion Channel Laser", IEEE Trans. Plasma Sci.,**18**, 837, (1990).

[65] P. Sprangle and A. T. Drobot, "The linear and self-consistent nonlinear theory of the electron cyclotron maser instability", IEEE Trans. Plasma Scei.,**MTT-25**, 528, (1977).

[66] K. R. Chu and J. L. Hirshfield, "Comparative study of the axial and azimuthal bunching mechanism in electromagnetic cyclotron instabilities", Physics Fluids **21** , 461,(1978).

[67] V. L. Bratman, "Relativistic gyrotrons and cyclotron autoresonance masers", Int. J. Electron., **51** , 541, (1981).

[68] R. G. Hemker, *et al.,* "Development of A Parallel Code for Modeling Plasma Based Accelerators", in Proceedings of the 1999 Particle Accelerator Conference, New York (IEEE, Piscataway, NJ, 1999).

[69] C. W. Roberson and P. Sprangle, "A Review of Free Electron Lasers", Physics of Fluids, **1**, 3, (1989).

[70] C. K. Birdsall and A. B. Langdon, "Plasma Physics via Computer Simulation", IOP Publishing Ltd, (1991).

[71] J. Magill, *et al.,* in : R. W. Ohse (ed.), Handbook of Thermodynamic and Transport Properties of Alkali Metals, **73** , Blackwell Scientific Publications, Oxford, (1985).

[72] A. G. Mozgovoi, *et al.,* "The saturated vapor pressure of lithium, sodium, potassium, rubidium, and cesium", High Temperatures-High Pressures, textbf 19, 425, (1987).

[73] C. B. Alcock, *et al.,* "Vapor pressure equations for the metallic elements 298-2500 K", Canadian Metallurgical Quarterly, **23**, No. 3, 309, (1984).